1-27-2014

The Interaction of LSM-YSZ Composite and Improvement of the Solid Oxide Cell Durability by Mn-modified YSZ

Na Li
University of Connecticut - Storrs, nali@engr.uconn.edu

The Interaction of LSM-YSZ Composite and Improvement of the Solid Oxide Cell Durability by Mn-modified YSZ

Na Li, PhD

University of Connecticut 2014

Solid state electrochemical systems such as solid oxide fuel cells (SOFCs) and solid oxide electrolysis cells (SOECs) are attractive for power generation, carbon capture, hydrogen and syngas production. YSZ and LSM have been extensively studied as electrolyte and electrode materials respectively for solid oxide cells operating in 800-1000°C temperature range. During the fabrication and operation of these systems, significant degradation in performance has been reported due to the formation of electrically insulating phases $La_2Zr_2O_7$ and $SrZrO_3$ at the LSM-YSZ interface.

The contradictory dada in literature, the limited information about effect of sintering atmosphere and the porosity urged a necessary systematic research of the LSM-YSZ composite system. This thesis includes a systematic study of reaction between LSM and YSZ, the role of oxygen pressure, porosity, raw power, sintering temperature and time on the air electrode densification, microstructural evolution and interaction of LSM-YSZ composite. In addition, the effect of zirconate phase on the thermal expansion coefficient (TEC) of the composite cathode was studied. Also, the reversibility of the reaction was studied, namely the $La_2Zr_2O_7$ formed in lower PO_2 can be reversed back into LSM and YSZ when resintered in higher PO_2. The

prevention of the detrimental LSM-YSZ reaction was discussed thermodynamically and successfully demonstrated by Mn-doped YSZ powder.

Long term degradation remains an issue for SOEC development. Anode delamination has been frequently observed and considered as one of the largest contributor to the cell performance degradation. Previous study found the resistive compound $La_2Zr_2O_7$ formed at the air electrode side, and $La_2Zr_2O_7$ formation degrades the cell performance. So the understanding from the study of the LSM-YSZ composite was applied in a symmetric solid electrolysis cell to alleviate the LSM-YSZ reaction. The SOEC electrochemical performance was improved by introducing a Mn-doped YSZ interlayer between LSM and YSZ. The delamination of air electrode was mitigated by a porous sol-gel Mn-doped YSZ interlayer. The sol-gel structure with high surface area and porosity is believed to be the possible reason for the prevention of delamination by release the oxygen pressure at the air electrode side.

The Interaction of LSM-YSZ Composite and Improvement of the Solid Oxide Cell Durability by Mn-modified YSZ

Na Li

B.E., Zhengzhou University, 2001

M.S., University of Connecticut, 2008

A Dissertation

Submitted in Partial Fulfillment of the

Requirements for the Degree of Doctor of Philosophy

At the

University of Connecticut

2014

APPROVAL PAGE

Doctor of Philosophy Dissertation

The Interaction of LSM-YSZ Composite and Improvement of the Solid Oxide Cell Durability by Mn-modified YSZ

Presented by

Na Li, B.E, M.S.

Major Advisor _____

Prof. Prabhakar Singh

Associate Advisor _____

Prof. Harris Marcus

Associate Advisor _____

Prof. Alexander Agrios

University of Connecticut

2014

Acknowledgements

I would like to thank Prof. Prabhakar Singh, my major advisor, for all the support and guidance throughout this work. Thank him for all the contributions of facilities, invaluable advice and dedication towards research enterprise. I'd also like to thank my associate advisors, Dr. Harris Marcus, Dr. Radenka Maric and my committee advisors Dr. Alexander Agrios and Dr. George A. Rossetti, Jr. for their useful discussions and contributions to this work. Thank Dr. Leon Shaw, Dr. Rampi Ramprasad and Dr. Steven Suib to serve on my committee for PhD general exam and proposal defense.

I am grateful to Pete Menard and Gary Barnes in the center for clean energy engineering for being a great laboratory support to my work. I would like to thank BJ McLaughlin, Sheila Ciccone and Amy Smith, Terry Barber-Tournaud for all the documentation support and paper work. I would like to thank Dr. Roger Ristau at Institute of Materials Science for FIB and TEM help, thank Dr. Lei Jin, Dr. Hector Fabian Garces Trujillo and Mark Biron for technical help from the characterization equipment.

I would like to thank all of my friends at the Center for Clean Energy Engineering, Dr. Manoj Mahapatra, Dr. Kailash Patil, Dr. Boxun Hu, Dr Mirela Dragon, Alex Lassman, Le Ge, Michael Keane, Keling Zhang, Sapna Gupta, Xiaofeng Wang, Guangliang Liu, Venkata Manthina, Rish Jain, Hui Fan and Juan Pablo Correa for the discussions and encouragements.

The last but not the least, thanks my family for the unconditional support for so many years.

Table of Contents

List of Figures

List of Tables

Chapter 1 Introduction

1.1 Fuel Cells

A fuel cell is an electrochemical device that can directly convert chemical energy from gaseous fuels (Hydrogen, natural gas, gasified coal) into electrical energy. The efficiency is not limited by the Carnot cycle and pollutant output is magnitudes lower than from conventional technologies. A fuel cell can continuously produce power when supplied with fuel and oxidant. [1] They offer higher electrical efficiency (≥ 40%) compared to conventional power generation systems such as reciprocating engine (~35%), turbine generator (30-40%), photovoltaics (6-20%), and wind turbines (~25%). Other advantages include fuel flexibility, base load and off-grid applications. Noise-free operation and modular construction are added features that allow its further application in small residential, automotive, portable electronic devices, as well as off-grid electricity generation in remote areas, marine and space applications[2] .

Based on the materials of construction, fuel cells are categorized mainly into five groups: low temperature fuel cell such as polymer electrolyte membrane fuel cell (PEMFC) and alkaline fuel cell (AFC) are mainly considered for transport applications, medium and high temperature fuel cell such as phosphoric acid fuel cell (PAFC), molten carbonate fuel cell (MCFC), and solid oxide fuel cell (SOFC) are mainly considered for stationary power plants [3] The operating temperature, materials, and advantages and disadvantages of the different types of fuel cells are presented in Table 1.1[4]. Although, the operating principles for all the fuel cells are governed by the Nernst equation, the electrode reactions vary widely depending on protonic or anionic conduction through electrolyte.

Table 1.1 Different types of fuel cells

	Polymer Electrolyte Fuel Cell (PEFC)	Alkaline Fuel Cell (AFC)	Phosphoric Acid Fuel Cell (PAFC)	Molten Carbonate Fuel Cell (MCFC)	Solid Oxide Fuel Cell (SOFC)
Operating temperature (°C)	40-80	65-220	150-210	600-700	600-1000
Charge carrier	H^+	OH^-	H^+	CO_3^{2-}	O^{2-}
Cathode reaction	$\frac{1}{2}O_2 + 2H^+ + 2e^- \rightarrow H_2O$	$O_2 + 2H_2O + 4e^- \rightarrow 4OH^-$	$O_2 + 4H^+ + 4e^- \rightarrow H_2O$	$\frac{1}{2}O_2 + CO_2 + 2e^- \rightarrow CO_3^{2-}$	$\frac{1}{2}O_2 + 2e^- \rightarrow O^{2-}$
Anode reaction	$H_2 \rightarrow 2H^+ + 2e^-$	$2H_2 + 4OH^- \rightarrow 4H_2O + 4e^-$	$2H_2 \rightarrow 4H^+ + 4e^-$	$H_2O + CO_3^{2-} \rightarrow H_2O + CO_2 + 2e^-$	$O^{2-} + H_2 \rightarrow H_2O + 2e^-$
Electrolyte	Hydrated polymeric ion exchange membrane	Potassium hydroxide in asbestos matrix	Liquid phosphoric acid in silicon carbide	Liquid molten carbonate in $LiAlO_2$	Ion conducting ceramics (yttria stabilized zirconia, gadolinia doped ceria, lantham gallate)
Electrodes	Carbon	Transition metals	Carbon	Nickel and nickel oxide	Perovskite, cermet (perovskite/fluorite and metal cermet)
Fuel	Hydrogen or methanol	Hydrogen or hydrazine	Hydrogen and alcohol	Hydrogen, hydrocarbons	Hydrogen, hydrocarbons
Oxidant	O_2/air	O_2/air	O_2/air	CO_2/O_2/air	O_2/air
Heat quality	-	Very low	Low	High	High
Advantages	• Solid electrolyte reduces corrosion and electrolyte management problems • Low operating temperature • Quick start up	• Faster cathodic reaction • Wide range of electro-catalysts	• Tolerance to impurities in hydrogen	• Fuel flexibility • Low cost catalyst	• All solid state components • Fuel flexibility • Low cost catalysts • No electrolyte flooding • Highest efficiency
Disadvantages	• Poisoning by trace contaminants in fuel • High cost platinum catalyst • Difficulties in thermal and water management	• High purity hydrogen	• Slow cathodic reaction • Corrosive nature of phosphoric acid • High cost platinum catalyst	• Corrosive electrolyte • High operating temperature • Long-term reliability of materials due to high temperature	• High operating temperature • High manufacturing cost • Long-term reliability of materials due to high temperature
Manufacturers	Ballard	AFC	Clear	Fuel Cell	Bloom Energy

	Power Systems, Canada; Baxi Innotech, Germany; SerEnergy, Denmark; M-Field Energy Ltd., China;	Energy, UK	Edge Power, USA; Toshiba Fuel Cell Power Systems, Japan	Energy, USA; Ishikawajima-Harima Heavy Industries (IHI), Japan	Corporation, USA; Acumentrics Corporation, USA; Ceres Power, UK; Topose Fuel Cell, Denmark; Hexis AG, Germany; LG Fuel Cell, South Korea; Osaka Gas Ltd. Japan; Toto Ltd., Japan

In comparison to other fuel cells, SOFC operates at significantly higher temperature (500-1000)°C enabling the use of low cost non-noble metal catalysts for electrode reactions and processing of a wide range of hydrocarbon fuels (from pipe line natural gas to diesel and logistic fuels). All solid state construction of SOFC eliminates the need for electrolyte management required for the liquid electrolyte fuel cells. Generation of high quality heat and its application in combined heat and power (CHP) co-generation system allows the overall system efficiency in excess of ≥80%[4,5]. Features such as water independence and carbon capture can be easily incorporated in SOFC's in comparison to other fuel cell systems. Challenges related to long term stability and cost reduction, however, remain. An overview of the basic operation, component materials, cell and stack design, and degradation processes is presented. The state of the art materials, development trend and mechanistic understanding of degradation processes are outlined.

1.2 SOFC Power System

A typical SOFC power system, schematically shown in Figure 1.1, consists of a hydrocarbon fuel processor, fuel cell stack, power conditioning equipment, and process gas heat exchanger for thermal management.[6,7] Power conditioning equipment, fuel processor and process

gas heat exchanger are termed as Balance of Plant (BOP). The operating temperature of SOFC ranges from (650-1000)°C. Emitted carbon dioxide from SOFC can be captured and stored using standard technologies for use in chemical and agriculture sectors. Capture of emitted carbon dioxide from SOFC is less energy intensive compared to that of conventional power plants and gasification plants. NO_x remains absent in the tail gas (flameless process). H_2 can be further separated for reuse as a chemical or fuel in fuel cells. The integration of SOFC and carbon capture and storage technologies in coal base power plants improve the overall efficiency and reduce carbon dioxide emission.[8,9,10,11]

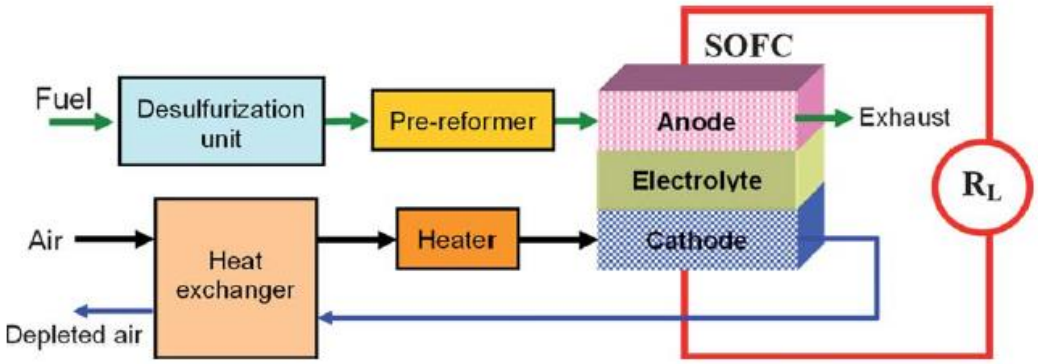

Figure 1.1 A simplified Schematic of a solid oxide fuel cell system.[12]

A single cell of a SOFC delivers a maximum of 1 V when hydrogen and air are used as the fuel and the oxidant, respectively[13]. To produce larger quantities of power, multiple cells are stacked in series or parallel connected by electrical conducting interconnects. Single cells are classified according to the porous support materials: anode supported, cathode supported, electrolyte supported, and metal supported. [14,15,16] The porous support materials thickness varies from 300 μm to a few millimeters with provisions for a gas diffusion path leading to electrochemical reactions at the cathode and anode electrodes. Anode supported cells are preferred due to low concentration polarization loss and the ability for hydrocarbon fuel gas

reforming at the support while higher polarization and ohmic losses have been observed for the cathode supported and electrolyte supported cells[17,18]. Although the fabrication process is simpler including lower cost and better thermal cycling resistance for the metal supported cells, the oxidation and corrosion of the metallic support remains a concern. Single cells are also divided into tubular and planar cell geometries as shown in Figure 1.2. [19] The power density of planar cell is higher than the tubular cell but hermetic seal is required to prevent gas mixing and leakage.[2]

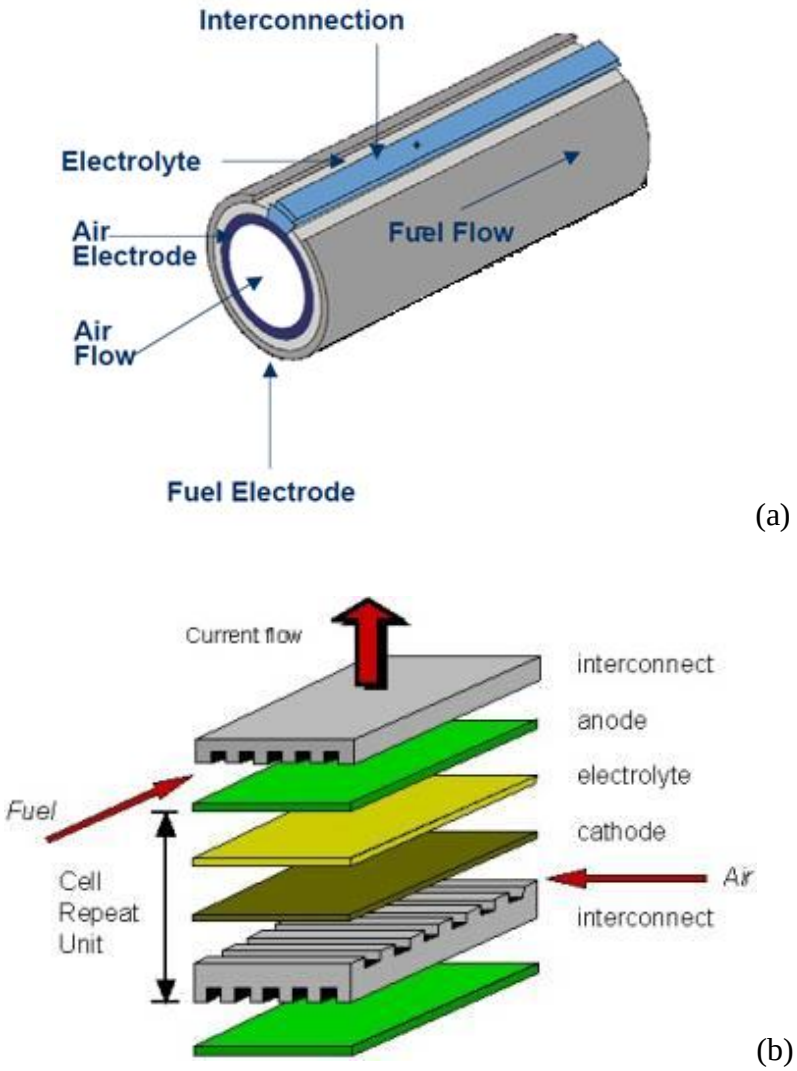

Figure 1.2 A single solid oxide fuel cell (a) tubular type (b) planar type

1.3 SOFC

The concept of the fuel cell was first proposed by William Grove in 1839 [20]. Following the discovery of solid oxide electrolytes by Nernst in 1899 [21], Baur and Preis (cited by Ormerod [22]) demonstrated the first SOFC running at 1273k in 1937. Due to significant achievements in both material developing and cell manufacturing in the last two decades, the SOFC is now approaching commercial reality.

1.3.1 Principle

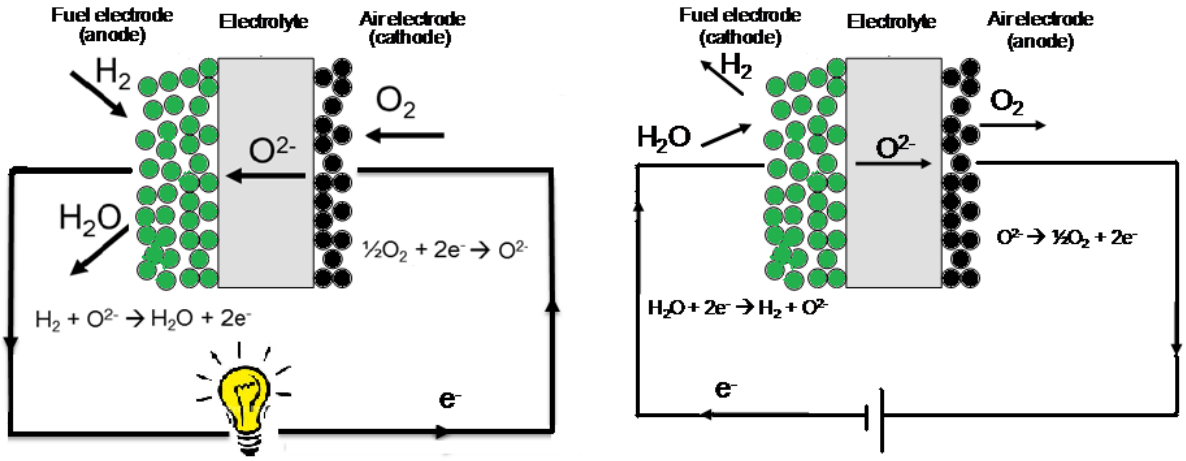

(a) (b)

Figure 1.3 Schematic diagrams of a solid oxide fuel cell and a solid oxide electrolysis cell.

Figure 1.3 (a) is a schematic diagram of the solid oxide fuel cell. When the fuel cell is in operation, fuel and oxidant are fed to the fuel electrode and the air electrode, respectively. At the cathode, oxygen receives electrons from the external circuit and is reduced to oxygen ion. Oxygen ion transports through electrolyte from cathode to anode side. At the anode, the fuel is oxidized and electrons are then released to the external circuit. The direct-current (DC) electricity is produced by the electron flow through the external circuit[23].

1.3.2 Electrical Losses

Nernst's equation serves as the underpinning principle for the operation of the fuel cell:

$$V_{Nernst} = \frac{RT}{4F} \ln \frac{P_{O_2\ oxidant}}{P_{O_2\ fuel}} \quad (1.1)$$

In practice, the actual voltage of a fuel cell is less than the Nernst potential due to electrical loss. The chemical to electrical energy conversion losses in a fuel cell, termed as polarization or over potential, is divided into activation polarization, ohmic polarization, and concentration polarization. Slow electrochemical reactions at the electrode surface leads to activation polarization and depends on the current density or electric bias. The origin of the ohmic polarization is the resistance to the flow of ions in the electrolytes and flow of the electrons in the electrodes. The concentration polarization relates to the diffusion and mass flow of the reactant species through the electrodes, inherent to the electrode materials and microstructure. The ohmic polarization increases with electrolyte thickness and formation of interfacial compounds at the electrolyte and electrode interfaces. The concentration polarization decreases with increasing current density or electric bias up to a certain value and increases above the limit. The concentration polarization is nominally higher in the cathode than in the anode. A representative plot of polarization losses with current density is shown in Figure 1.4.[2] The actual voltage (V_{Cell}) of a cell during operation with a given current density is:

$$V_{Cell} = V_{Nernst} - \text{ohmic loss} - \text{polarization losses} \quad (1.2)$$

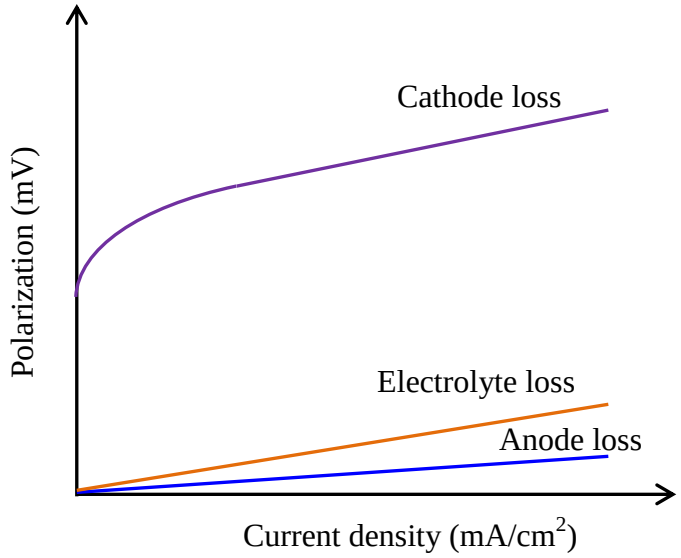

Figure 1.4. Schematic representation of the contribution of cathode, anode, and electrolyte contribution to electrical loss.

There has been significant progress in reducing the operation temperature of SOFC from traditional 1000 ºC to intermediate temperature range of 600–800 ºC. Decreasing the operation temperature brings both dramatic technical and economic benefits. The cost of SOFC system can be substantially reduced by using metal alloys instead of expensive lanthanum chromite as interconnect.[24] Furthermore, as the operation temperature is reduced, system reliability and operational life increases.[25] On the other hand, reduction in operation temperature results in a significant increase in the electrolyte and electrode resistivity and the polarization losses. To compensate for the increase in ohmic losses at lower temperatures, electrolytes with higher ionic conductivity or thinner films are used.[26] In SOFCs based on thin electrolyte, the overall losses of the cell are generally dominated by the polarization losses for the O_2 reduction on the cathode[27]. This is partly due to the high activation energy and slow reaction kinetics for the O_2 reduction reaction when compared with the hydrogen oxidation reaction. Consequently the development of

cathodes with high performance and high stability becomes increasingly critical for the intermediate-temperature SOFCs or ITSOFCs.

1.3.3 Advantage

Compared with conventional power generation, the fuel cell technology offers several advantages. For example, the high operating temperature results in high reaction rates. No expensive catalysts are thus needed. Another advantage of SOFCs is that it can use natural gas directly. It also has substantially higher energy conversion efficiency, much lower production of pollutants, modular construction, siting flexibility etc.[28]

1.3.4 Application

There are three main applications of SOFC such as combined cycle power plant, cogeneration/regeneration for hotel, residential building, hospital etc. and transportation application.

1.4 Overall Materials

The main components of a SOFC stack are the electrolyte, the cathode, the anode and the interconnect (Figure 1.2). Each component serves several functions and therefore has to meet certain requirements. All the components must possess proper electrical conductivity and must be chemically and physically stable in an oxidizing and/or reducing atmosphere. Each component must be chemically compatible with the other components and its thermal expansion coefficient should be similar to those of the others. The anode and the cathode are porous to allow fuel or oxidant gas to be transported to the reaction sites, while the interconnect and the electrolyte are dense to prevent gas mixing.

1.4.1Electrolyte

Fluorites material such as zirconia and ceria and perovskite material such as lanthanum gallate have been recognized as oxide ion conducting SOFC electrolytes. [29,30] Lower valence

cation doping in zirconia and ceria create oxygen vacancies in the crystal lattice. Similarly, lower valent cations doping on A and B-sites of lanthanum gallate create oxygen vacancies in the lattice. The conductivity of all the electrolytes depends also on the processing and microstructure.

Yttria stabilized zirconia (YSZ) and scandia stabilized zirconia (ScSZ) are used as SOFC electrolytes. Addition of dopant increases the conductivity and reaches a maximum. Further addition of dopants decreases the conductivity, as shown in Figure 1.5, due to defect clustering and lattice strains. Increase in temperature decreases the activation energy for oxygen migration and hence the conductivity follows Arrhenius behavior with temperature. The maximum conductivity is obtained for approximately 8 mol% yttria and 10 mol% scandia additions. The conductivity of YSZ and ScSZ are suitable for high temperature ($\geq$800°C) SOFC operation. The conductivity of YSZ and ScSZ decreases due to the materials aging during SOFC operation, and the conductivity decreased to almost same value for both materials after aging. The small difference in ionic radii of zirconium and scandium ions is the reason for the higher conductivity of ScSZ. Although the conductivity of ScSZ is higher, it may not be advantageous for long term operation. The reason is that yttria doping stabilizes the cubic symmetry of zirconia but scandia doping changes the symmetry from cubic to rhombohedral structure below 600°C. [31,32] The lattice strain due to the polymorphic transformation may lead to elastic strain during thermal cycling.

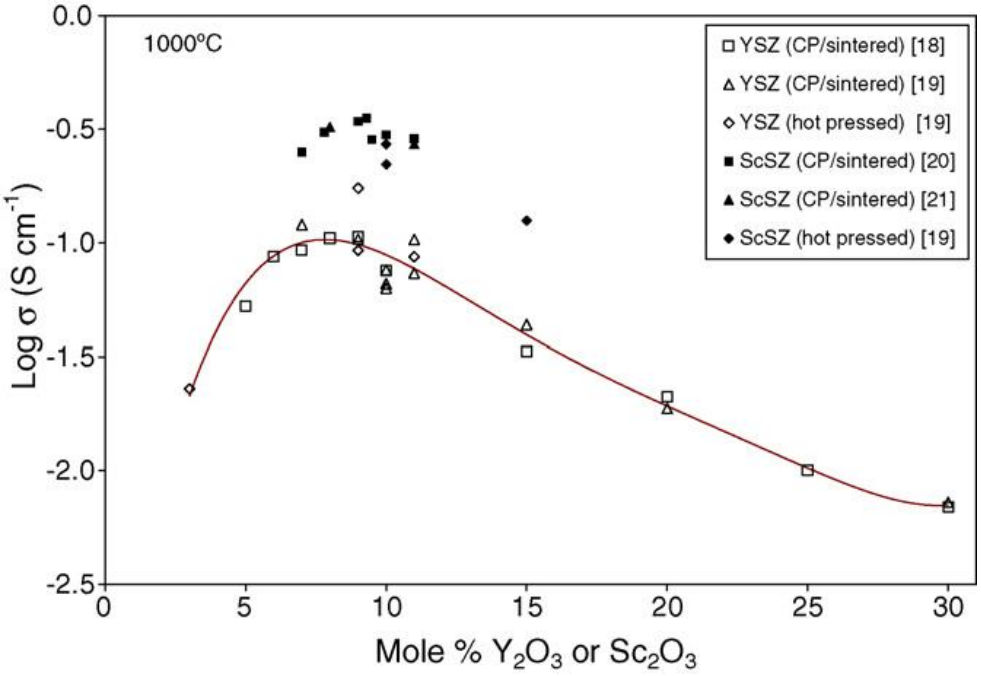

Figure 1.5 Conductivity of yttria and scandia stabilized zirconia in air at 1000°C. [29]

The maximum conductivity of ceria can be obtained by doping using 10-12 mol% gadolinia (GDC) or samaria (SDC).[33] The higher conductivity of ceria below 600°C enables a decrease in the SOFC operating temperature to ~650°C. The Ce^{4+} reduces to Ce^{3+} in reducing atmosphere and induces undesirable electronic conductivity. For example, the electronic conductivity dominates over ionic conductivity at ~10^{-19} atm PO_2 at 700°C [34,35]. Therefore, ceria based electrolyte is not suitable for high temperature SOFC even though the conductivity is higher compared to YSZ.[36] Also, reduction of cerium ion increases lattice strain during thermal cycling due to higher oxygen vacancies.

The highest conductivity in lanthanum gallate has been achieved by strontium doping at A-site and magnesium doping at B-site with $La_{0.8}Sr_{0.2}Ga_{0.9}Mg_{0.1}O_3$ (LSGM) formula.[29,30] The conductivity of LSGM is higher than YSZ and comparable to GDC. LSGM is suitable as electrolyte in a wide range of operating temperature. Similar to GDC, electronic conductivity has

also been observed for LSGM in a reducing atmosphere. For example, electronic conductivity is predominant at ~10^{-18} Pa (~10^{-23} atm) PO_2 at 1000°C and restricts its application at higher temperature.[37] However, the bulk conductivity may be compromised due to elemental inter-diffusion across the interfaces.[29] The lower conductivity (than that of GDC at a lower temperature) may be the reason for the limited exploration of LSGM as the electrolyte of solid oxide cells.

1.4.2 Fuel Electrode

Ni/YSZ cermet is considered as the state-of-the art SOFC anode material because of: a) catalytic and reforming activity of nickel for the oxidation of various fuel constituents, b) high electronic conductivity of nickel and ionic conductivity of YSZ for increasing TPB length and c) ease of fabrication by co-firing. Nickel is an electrical conductor and YSZ is an ionic conductor.[38,39] Fuel oxidation takes place at the triple phase boundary as shown in Figure 1.6 (a).[38] The disadvantages of Ni/YSZ anode formulation are: a) poor redox cycling stability and b) poisoning with subsequent deactivation of catalytic property due to the presence of gas phase impurities.

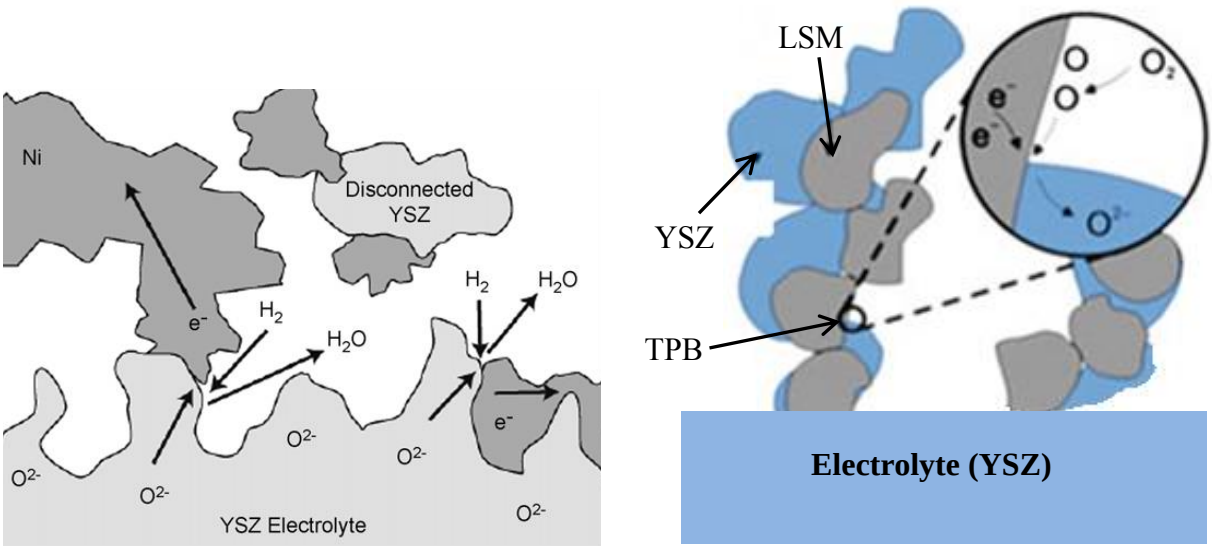

Figure 1.6 Triple phase boundary at (a) anode-electrolyte interface and (b) cathode-electrolyte interface.

Nickel is oxidized to nickel oxide (p-type) above equilibrium oxygen partial pressure if air is leaked and mixed with fuel. Nickel oxidation has also been observed in the presence of steam in fuel.[40,41] Volume change due to oxidation may not generate sufficient strain to form cracks at the nickel/YSZ interface, due to its porous microstructure, but may do so at the anode-electrolyte interface[41,42] Gas leakage through the pores/cracks at the interface decreases the electrochemical driving force (establishment of smaller oxygen partial pressure gradient across the electrolyte) leading to lower SOFC performance. The volume change during the reduction-oxidation (redox) cycle is not reversible on prolonged subsequent reduction. This process induces strain in the bulk anode creating nickel particle to particle separation, loss of continuous contact and increase in the resistance, result in the decrease of the effective TPB length. The redox cycling stability of Ni-YSZ cermet is better for coarser microstructure and lower operating temperature but worse in steam containing fuel since steam favors densification of Ni-YSZ cermet with finer microstructure.[43] In practice, a finer microstructure to increase TPB length and a higher operating temperature for faster fuel reduction kinetics are preferred.

The impurities in the anode can be intrinsic and extrinsic. The common intrinsic impurities in nickel metal are Al, Ca, Cu, Fe, Mg, and Si. The common impurity in YSZ is SiO_2.[44,45,46] The impurities alter the anode morphology and deposit at Ni-YSZ interfaces during SOFC operation. Commonly found extrinsic impurities are H_2S and CO in fuel gas, silica in seals and insulating materials.[12,44,47] Very small amount of sulfur in fuel is detrimental. For example, 1 ppb of sulfur can cover 60% surface of nickel and deactivate the catalytic activity[48]. At normal SOFC operating conditions, sulfur degrades anode performance by chemical

adsorption at nickel surface and TPB, formation of Ni_3S_2 compound at high concentration of sulfur (≥100ppm), and inducing microstructure change.[49] Although chemical adsorption and compound formation is reversible, the microstructure change is irreversible.

Carbon deposits at the nickel-YSZ grain and grain boundaries mainly in filamentary forms and also as amorphous particles.[50, 51] If carbon deposition increases the electrical conductivity, the electrochemical reaction kinetics may be enhanced. However, carbon dissolves and diffuses through nickel particles above a critical amount.[52,53] Dissolution of carbon decreases the electrical conductivity of nickel. Carbon dissolution and diffusion also swells microstructure of nickel and forms cracks at the anode.[52] All these phenomena lead to decrease anode performance.

Silica in seals and YSZ can form vaporized species, $Si(OH)_4$ at the normal operating condition and deposits at the grain boundaries as observed by striations in the TPB and nickel surface.[54,55] Silica forms low melting point silicate compounds with the other impurities. Being electrically insulating, the presence of silica and silicate phases contributes to anode performance degradation.[45]

To overcome above mentioned problems in Ni-YSZ cermet; mixed ionic electronic conducting oxides such as $LaCrO_3$, $SrTiO_3$, $La_{1-x}Sr_xVO_3$, $Sr_2Fe_{1.5}Mo_{0.5}O_{6-\delta}$, Sr_2MgMoO_6 based perovskites have been investigated for potential anode application [12,38,56,57,58,59]. The performance of a Sr and Mn doped $LaCrO_3$ anode is comparable with that of Ni-YSZ cermet.[60] These materials suppress sulfur deposition.[61] Also, no evidence of carbon deposition has been reported.[58] The alternative anodes also have several drawbacks: a) the electronic conductivity of these materials may not be sufficient for faster fuel oxidation kinetics. b) the long term stability of these materials is questionable. c) dopants increase the electrical conductivity as well as

catalytic activity but above a critical concentration the structure can be destabilized and the secondary phases form compounds with sulfur. For example, excessive manganese doping destabilizes $LaCrO_3$ perovskite structure and forms MnS and La_2O_2S compounds in H_2S contacting fuel. [62,63]

1.4.3 Air Electrode

The air electrode is the material where pure oxygen or oxygen from air, combining electrons externally from the cell, is reduced to oxygen ions through the following electrochemical reaction. Among the various air electrode materials, lanthanum strontium manganite (LSM) perovskites, till today, are the most investigated and probably the most important electrode materials in SOFCs [64].

A 20 mol% strontium doped lanthanum manganite ($La_{0.8}Sr_{0.2}MnO_{3+\delta}$) is considered as the state-of-the-art air electrode material for high temperature SOFC (800-1000℃ operating temperature).[64] The LSM is an electronic conductor. Ionic conduction of LSM is due to the oxygen vacancy in oxygen lattice. Oxygen adsorbs and desorbs at the surface only. In bulk LSM, oxygen migrates only through surface since absence of oxygen vacancy prohibits oxygen migration through the bulk. Therefore, the electrochemical reaction sites (TPB) mainly exist at the cathode-electrolyte interfaces [65]. However, cathodic bias enables oxygen migration through oxygen vacancies in the bulk [66]. The oxygen vacancies can also be created by (a) substitution of La^{3+} by Sr^{2+} and (b) partial reduction of Mn^{4+} to Mn^{3+} or Mn^{3+} to Mn^{2+}. [67,68] The very low oxygen ionic conductivity of LSM is considered to be the main factor for the high polarization losses of LSM cathode for the O_2 reduction reaction in ITSOFC[69].

Despite low ionic conductivity and slow oxygen reduction kinetics, LSM remains attractive due to thermal expansion match with YSZ electrolyte and the thermo-chemical

stability.[64] Oxygen reduction kinetics can be enhanced by increase in TPB length by addition of ionic phase such as YSZ above the percolation limit.[70,71] Infiltration of nanoparticles of YSZ further increases the TPB and cathode performance.

Mixed ionic electronic conductors (MIECs) as cathode materials have also been investigated.[72,73] Strontium doped lanthanum ferrite, cobaltite, and cobaltite ferrite are some of the examples of MIECs. These materials show high electrical and ionic conductivity as well as electrocatalytic activity for the oxygen reduction. Higher CTE (12.2-20.5× 10^{-6}/°C) of these materials, however, make them prone to cracking and delamination from the adjoining interfaces (electrolyte and contact layers) during SOFC operation resulting in the performance degradation.[74] Strontium doped lanthanum cobaltite ferrite (LSCF) has been recognized as air electrode with better performance than LSM due to higher surface exchange coefficient and diffusivity of oxygen, and lower polarization resistance than LSM [75]. LSCF is a MIEC material with faster oxygen reduction kinetics. Being an oxygen deficient perovskite, oxygen ions migrate through the oxygen vacancies in the bulk material. [76] Oxygen also adsorbs and ionized at the surface and migrates through surface similar to electronic conductor.[73] The optimized $La_{0.6}Sr_{0.4}Co_{0.2}Fe_{0.8}O_{3-\delta}$ formula shows thermal expansion match with electrolyte and better bulk stability among other compositions in the LSCF family.[30] Formation of SrZrO3 due to severe solid state reaction with YSZ at ~800°C limits LSCF application for SOFCs.[77] Gadolinium doped ceria (GDC) is the preferred electrolyte for LSCF cathode. Elemental inter-diffusion across LSCF and GDC during device fabrication (≥1100°C), however, is sufficiently high for oxide segregation at the grain boundaries as well as at the interface, corroborating to degradation in cell performance. [78,79]

The properties of these cathode materials are listed in Table 1.2 [80]. The type and levels of dopants tune the properties of these ABO_3 type perovskites but only the optimized composition will be emphasized in this section.

Table 1.2 Thermo-physical properties of SOFC cathodes and electrolytes

Properties	YSZ	GDC	LSM	LSM/YSZ	LSCF
TEC (× 10-6/°C)	10.5	11.9	12	11.5	14-17
Electronic conductivity (S/cm)	0.01 at 800°C	0.1 at 800°C	190 at 900°C	10^{-3} at 900°C	275 at 700°C
Ionic conductivity (S/cm)			10^{-6}-10^{-7} (900-1000°C)		0.01 at 700°C
Surface exchange coefficient (cm/s)	10^{-18}-10^{-19} (700-900°C)	10^{-18}-10^{-19} (600-700°C)	10^{-8} -10^{-9} (700-900°C)	10^{-6} -10^{-7} (800-900°C)	10^{-6} -10^{-7} (650-750°C)
Oxygen diffusion coefficient (cm^2/s)	10^{-15}-10^{-16} (700-900°C)	10^{-18}-10^{-19} (600-700°C	10^{-13} – 10^{-16} (700-900°C)	10^{-9} (800-900°C)	10^{-7} – 10^{-12} (750-850°C)

Apart from solid-state interactions with the electrolyte, cathode performance also degrades due to interaction with the impurities in air, chromium vapor species from metallic interconnects, and other impurities such as silicon from sealants and insulating materials.[81,82,83,84,85,86] The main impurities in atmospheric air are ~3% H_2O, ~400 ppm CO_2, and sulfur at ppb level in the form of $SO_2/SO_3/H_2S$. The impurity content can vary with geographical regions. For example, moisture content will be much higher in the coastal area. Moisture in air

precipitates strontium oxide at the surface of LSM and LSCF cathodes but there is no consensus on the mechanism of strontium segregation at the cathode.

The effect of trace amount of sulfur in air on cathode degradation has not been demonstrated. The effect of high concentration sulfur (0.1-100 ppm) in air has been reported for accelerated test conditions.[87] The performance of LSM cathode slightly degrades in presence of ~ 100 ppm sulfur but no secondary compound has been found. Sulfur reacts with LSM in the presence of chromium and forms $Sr(Cr,S)O_4$ compound.[88] Sulfur reacts with LSCF and forms $SrSO_4$ compound when the concentration is ≥1ppm. LSCF decomposes and forms $CoFe_2O_4$ and $La_2O_2SO_4$ compounds with increase in sulfur content.[89] In a recent study, the presence of $SrSO_4$ has been shown in a LSCF cathode thermally treated at 600°C for 1000 h without any external source of sulfur. Silicon evaporates in the form of $Si(OH)_4$ in humidified atmosphere during SOFC operation and deposits at the cathode surface.[90]

Chromium transportation from metallic interconnect (chromia forming alloy) degrades the cathode performance, known as chromium poisoning.[91] Chromium transports in the form of CrO_3 and/or $CrO_2(OH)_2$ vapor species, respectively, in air and humidified air. These vapor species reduces to Cr_2O_3 and deposits randomly and also reacts with the cathode. The reaction product is $(Cr,Mn)_3O_4$ spinel for LSM and $SrCrO_4$ for LSCF cathodes.[86] Cr_2O_3 and the reaction products prefer to deposit at the junction of electronic conducting, ionic conducting, and gas phases. Therefore, chromium species deposition blocks the electrochemical reaction sites (triple phase boundary) for LSM and/or LSM/YSZ cathode while the chromium species deposition is randomly distributed through the MIEC cathodes such as LSCF.[91] Subsequently, the performance degradation is higher for the LSM compared to LSCF.

1.5 Solid Oxide Electrolysis Cell

The cleanest method of producing hydrogen has been water electrolysis. In this field, hydrogen generation from water electrolysis using solid oxide electrolysis cell (SOEC) has been attracted a lot of interests in the last few years, as they offer significant higher efficiencies compared to conventional low temperature electrolysers.[92] Of all the methods to produce hydrogen, water electrolysis is probably the cleanest when combined with a renewable energy source to produce the electricity.

The principle of a water electrolyser is to convert water and DC electricity into gaseous hydrogen and oxygen. This process was firstly demonstrated by Nicholson and Carlisle in 1800. In the 1820s Faraday clarified the principles and in 1934 he introduced the word "electrolysis". SOEC technology attracted great interest in the 1980s because of the studies carried out by Dönitz[9394,95,96,97] and the contribution from Westinghouse Electric Corporation R&D Centre[98]. Research in high temperature electrolysis has increased significantly in recent years.

The electrochemical reactions that take part in an SOEC are the inverse reactions to those that take part in an SOFC. Cell polarization is the opposite and anode and cathode interchange their roles. In an SOEC, water acts as a reactant and is supplied to the cathode side of the cell (anode electrode in SOFC mode). Oxygen ions are transported to the anode through the electrolyte, and hydrogen is produced in the cathode side, as shown in Figure 1.3 (b). The overall reaction of the water electrolysis is:

$$H_2O \rightarrow H_2 + \tfrac{1}{2}O_2 \tag{1.3}$$

The reactions in the cathode and anode sides are:

Cathode side: $$H_2O + 2e^- \rightarrow H_2 + O^{2-} \tag{1.4}$$

Anode side: $$O^{2-} \rightarrow \tfrac{1}{2}O_2 + 2e^- \tag{1.5}$$

1.5.1 Degradation Issues in Solid Oxide Electrolysis Cells

One of the most important developmental barriers in SOEC technology is long-term degradation. For example, cell degradation, responsible for as high as 40% reduction in hydrogen production rate in 2000 hour tests with SOEC stacks has been reported. [99] All the long-term degradation studies have concluded that further improvements are required prior to commercialization. Short-term degradation is also frequent in SOEC cells, especially operating under extreme conditions such as high current densities or high steam concentration at the fuel electrode.

A number of causes for the observed degradation have been identified. The degradation has been classified into two broad groups: (a) electrode poisoning due to gas phase contamination, and (b) gradual delamination of the electrode at the anode-electrolyte interface. Aging studies up to 1300 h were made at Risø at 850ºC, and 50% RH of steam, showing a degradation rate of 2%.[100] The degradation was mainly attributed to the Ni/YSZ electrode. The growth of Ni particles as well as the presence of Si impurities possibly, related to the variation in the electrolysis operation conditions.[45] SOEC operation in a 720-cell stack for 1080 h at 830°C from INL was also reported and 20% performance degradation was observed.[101] In this case, the hydrogen electrode (Ni–YSZ) was mainly in good condition apart from relatively few silicon impurities coming from the seal. The presence of Cr doped Al_2O_3 was also observed near the seals coming from the bipolar plates and cation diffusion at the air electrode. Overall, the largest contributor to cell performance degradation is the delamination of the air electrode due to the high oxygen partial pressures at the electrode/electrolyte interface occurring upon O_2 evolution in closed pores in the electrode/electrolyte interface, as observed by other authors [102 ,103, 104]. A typical example of the oxygen electrode delamination can be observed in Figure 1.7. Anode

delamination from the electrolyte results in a current constriction and increased ohmic loss[103,105,106]. Understanding the cause of oxygen electrode delamination and its mitigation should be considered a high priority. [107]

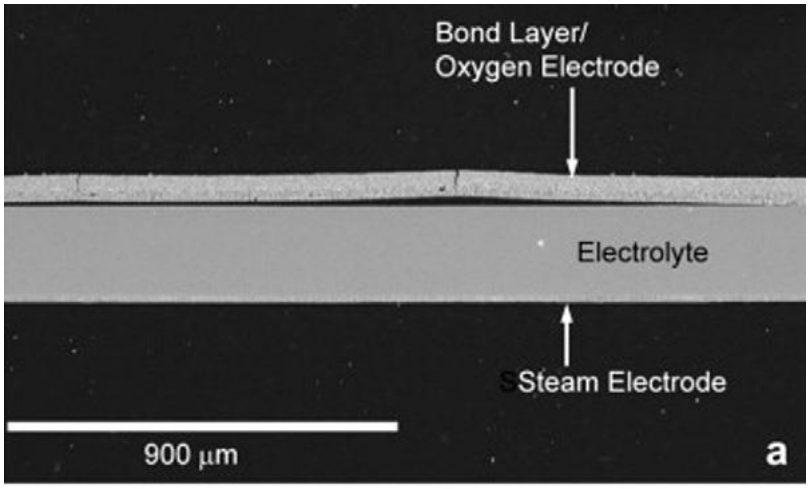

Fig 1.7 SEM micrographs of a polished cross-section of a cell from the 2000h stack [108]

Different mechanisms have been proposed on the anode delamination, such as high oxygen pressure development, electrolyte grain boundary separation, morphological changes in the LSM anode, high oxygen chemical potential produced under an anodic overpotential, thermal expansion mismatch[109], and the penetration of evolved oxygen into the closed pores/defects at the electrode/electrolyte interface. Virkar et al employed a concept of local thermodynamic equilibrium and equivalent circuit modeling scheme to analyze the delamination problem, and proposed that the mechanical failure and delamination of the anode electrode is primarily due to the buildup of high oxygen pressure at the anode-electrolyte interface as well as within the electrolyte due to differences in ionic and electronic conductivity between the electrode and the electrolyte[110]. Kaiser et al concluded that the electrode delamination could be caused by the presence of doped aluminum in YSZ and formation of an electronically conducting $MnAl_2O_4$ layer near the anode–electrolyte interface[105]. Chen et al. concluded that the delamination of LSM

anode results from the formation of nanoparticle clusters under high oxygen partial pressure at the interface.[111] The formation of nanoparticles is due to migration of oxygen ions from YSZ into LSM, resulting in LSM lattice shrinkage and local tensile strains within LSM particles.

A combination of first principles, DFT based calculations and thermodynamic modeling has been used to understand the delamination mechanisms.[112] Authors proposed that high temperature interdiffusion across the LSM/YSZ interface significantly affected structural stability of the materials and their surface. Particularly La and Sr substitutional defects positioned in ZrO_2 and near interface significantly change oxygen transport which may cause pressure to build up in the interfacial region and eventually anode delamination. A ceria barrier between YSZ and LSM was suggested to reduce the formation of high resistance oxide phases and avoid delamination.

Chen et al.[113] studied LSM-YSZ composite air electrodes under SOEC operation conditions, the incorporation of YSZ significantly enhances the electrocatalytic activity on LSM, but electrode delamination and failure also occurred. Authors attributed the delamination to the formation of LSM nanoparticle at the interface and suggest minimizing the direct contact of LSM particles and YSZ electrolyte. Yang et al. reported that the porous LSM-YSZ oxygen electrode made by conventional mixing method was well adhered to the YSZ electrolyte after 7 days testing in Steam/H_2 at 800-900ºC in electrolysis mode.[114] Knibbe et al. however didn't observe delamination for LSM-YSZ composite oxygen electrode but the formation of micro-pores in the grain boundary of YSZ electrolyte near the anode-electrolyte interface.[115] The porosity formation is postulated to be due to high oxygen partial pressure build up.

Yang et al. fabricated porous LSM-YSZ composite as anode by an impregnation method. The electrolysis cell showed relatively lower area specific resistance than the conventional

mixing LSM-YSZ anode, and demonstrated stable performance at 800ºC for 50h.[116] Chen et al. improved the stability of SOEC by infiltrating pre-sintered porous YSZ scaffold with nano-structured LSM particles as LSM-YSZ composite cathode. The stable performance can be reached under electrolysis operation at 500mA cm^{-2} at 800C for 100h. The authors attributed the good performance to the infiltrated LSM nanoparticles.[117]

Mawdsley et al performed the post-test analysis for the 1080h testing cell from INL and proposed two possible mechanisms that might cause the oxygen electrode delamination, excessive pressure build up with high O_2 flow in over-sintered region, or defects acting as nucleation sites for localized cracking of the perovskite-zirconia interfaces within the electrolyte layer.[118]

Though several approaches for the mitigation of electrode delamination has been suggested including modification of the electronic and ionic resistances of the device components[110] and operation under AC voltage rather than DC voltage[119], the delamination phenomena has neither been fully understood nor prevented for the LSM anode. The previous study in our group found the resistive compound lanthanum zirconate formed at the anode side and related the LZ formation with the degradation and delamination.[120] The understanding of LSM-YSZ system may help us to suppress the electrode/electrolyte interfacial reaction, mitigate anode delamination and improve the longevity of the SOEC device.

1.6 LSM-YSZ Reaction

The LSM-YSZ reactions have been extensively studied during the past two decades. Formation of electrically insulating phases ($La_2Zr_2O_7$ and $SrZrO_3$) at the LSM-YSZ interface resulted in significant degradation has been reported during the fabrication and operation of SOFC and SOEC systems.[64,121]

When tested in fuel cell mode degradation of air electrodes based on stoichiometric LSM caused by formation of secondary phases that are poorly conductive such as $La_2Zr_2O_7$ or $SrZrO_3$ was reported.[23,122,123,124,125,126] So far only a few reports on electrolysis tests with degradation of the LSM based air electrode e.g. caused by such secondary phases have been published.[127,128]

The electrical conductivity of the above phases is significantly lower than those of LSM and YSZ.[129] For example, at 1000°C, the electrical conductivities of $La_2Zr_2O_7$, $SrZrO_3$ and $La_{0.8}Sr_{0.2}MnO_3$ are ~2×10^{-5} Scm^{-1}, 1×10^{-4} Scm^{-1}, and ~200 Scm^{-1}, respectively. The ionic conductivity of YSZ is 0.1 Scm^{-1}.[130,131,132] Formation of the zirconate phases changes the morphology of LSM and LSM-YSZ interface, decreases the length of triple phase boundary (electrochemically active area), and increases the interfacial resistance at the LSM-YSZ interface resulting in SOFC performance degradation.[133] For instance, the length of the triple phase boundary decreases from ~0.7 μm^{-1} to ~0.4 μm^{-1} and the interfacial resistance increases from ~100 $\Omega\cdot cm^2$ to ~250 $\Omega\cdot cm^2$ while the $La_2Zr_2O_7$ thickness at the LSM-YSZ interface increases from ~ 50 nm to ~ 70 nm.[134]

The reaction between LSM and YSZ depends on the composition of $La_{1-x}Sr_xMnO_3$ (Sr concentration and A/B ratio), yttria concentration and crystal structure of YSZ, the ratio between LSM and YSZ, characteristics of starting powder, sintering temperature, time, and atmosphere.[135,136,137,138] Several studies have indicated that $La_2Zr_2O_7$ forms for $x \geq 0.0$ and $SrZrO_3$ along with the $La_2Zr_2O_7$ starts to form for $x \geq 0.3$,[126,139] while other studies reported that both zirconates can form at $x \geq 0.17$, which is also consistent with thermodynamic calculations[123,135]. Formation of $SrZrO_3$ at 1: 1 LSM and YSZ ratio and $La_2Zr_2O_7$ at 1:3 ratio was reported during annealing at 1000°C in N_2 (PO_2 ~10^{-5} atm) atmosphere[140]. However, $SrZrO_3$ formation was not observed when LSM and YSZ ratio ≥ 1.0[135]. Lowering of the A/B ratio in LSM may retard the formation

of zirconate phases but cannot hinder the reaction. Although it has been reported widely in literature that the formation of zirconate phases depends on the starting powder characteristics, reaction temperature and exposure atmosphere, the effect remains little understood in terms of densification, grain growth and phase evolution[136].

The zirconate phases formation has been reported in a wide temperature range between 1000ºC to 1400ºC. [126,141] $SrZrO_3$ forms at higher temperature than that of $La_2Zr_2O_7$. For instance, $La_2Zr_2O_7$ forms at 1200°C but $SrZrO_3$ forms at 1350°C for $La_{0.6}Sr_{0.4}MnO_3$-YSZ composites sintered in air for 120h [139]. The amount of the zirconate phases increases with increase in sintering time.[23,126,137,140] Interdiffusion of respective cations across the LSM-YSZ boundary during the sintering of LSM-YSZ has been reported to be responsible for zirconate phases formation.[134,137,142,143,144]Among all the elements in the LSM-YSZ composites, the diffusivity of manganese remains the highest.[129] However, diffusion of manganese into the YSZ has not been observed by several researchers. [23,123] The contradictory nature of the above results related to LSM-YSZ interactions may be attributed to the difference in powder characteristics such as composition, morphology, surface area etc.

Most of the above reported studies have been conducted in air and electrochemical device operation conditions typically in the temperature range of 800-1100°C. But the understanding of the LSM-YSZ composite interaction under the device fabrication conditions remains largely unknown. Typical fabrication conditions include sintering at elevated temperatures in the range of 1200-1500°C in air.[145,146,147,148] Role of sintering atmosphere on the air electrode densification, microstructural evolution and chemical interactions also remains unknown at these elevated temperatures. Above understanding is also considered useful for establishing degradation processes during cell operation where oxygen partial pressure (PO_2) at the LSM-YSZ interface

can be as low as 10^{-5} atm.[149] PO_2 change at the LSM-YSZ interface can occur during SOFC operation due to several reasons including (1) temperature gradient and hot spot, (2) changes in the component microstructure, (3) polarization of the electrodes (4) intermixing of fuel gas and air due to internal cracks and seal leakage and (5) variability in the repeat cell unit contact resistance in the stack.[149,150]

It has been demonstrated that the lower PO_2 favors the formation of the zirconate phases.[135,138,151] For example, zirconate phases are absent when LSM-YSZ composite sintered in air at 1000°C for 5 weeks but present while sintered in N_2 atmosphere.[138] These studies have not shown the detailed and systematic morphological evolution of reaction products and structure at lower PO_2. It was reported that porous electrodes accelerated the LSM-YSZ interaction when compared to dense electrodes.[124] Only $SrZrO_3$ formed for dense electrode, while both $La_2Zr_2O_7$ and $SrZrO_3$ formed for porous composite structure.[141] Even though porous cathodes are required for electrochemical systems applications, most of the studies have been conducted on dense LSM-YSZ composites.[124,126, 152] In addition, the effect of zirconate phase on the thermal expansion coefficient (TEC) of the composite cathode remains unknown.

The contradictory dada in literature, the limited information about effect of sintering atmosphere and the porosity urged a necessary systematic research of the LSM-YSZ composite system.

1.7 Our Strategy and Organization of the Dissertation

This research project includes a systematic study of reaction between LSM and YSZ; understand the LZ formation mechanisms as well as the morphology and structure change of the reactants under different sintering conditions, such as sintering temperature, time and atmosphere. LSM powders from different source and with different particle size was used to compare the

effect of raw material, samples with more or less pore formers were characterized to see the effect of porosity. A sintering temperature of 1400°C was selected to represent the device sintering condition. An oxygen partial pressure range of 0.21 to 10^{-6} atm was selected to study the effect of PO_2 on the phase interaction and microstructural evolution. Besides the zirconate formation, the YSZ and LSM morphology and crystal structure were changed greatly. Also, the reversibility of the reaction will be studied, namely the LZ formed in lower PO_2 can be reversed back into LSM and YSZ when resintered in higher PO_2. In addition, the effect of zirconate phase on the thermal expansion coefficient (TEC) of the composite cathode was studied. Since the reaction degrade the performance of the fuel cells, prevention of the reaction between LSM and YSZ by modification of the composition of the reactants will be pursued.

At last, the fundamental knowledge we get from the systematic study of the LSM-YSZ composite will be applied in solid oxide electrolysis cell to prevent the LZ formation at the anode-electrolyte interface and improve the cell performance; the anode delamination mechanism was also discussed and mitigated.

On the basis of the discussion above, this dissertation is generally divided into six parts: Role of PO_2 on the stability of dense LSM-YSZ composite (Chapter 2), LSM-YSZ reaction in porous sample (Chapter 3), Other factors for the interaction between LSM and YSZ (Chapter 4), The reversibility of the reaction between LSM-YSZ (Chapter 5), Improvement of the durability of SOEC by Mn Modified YSZ (Chapter 6).

Chapter 2 presents the stability of dense LSM-YSZ composite. The role of oxygen pressure on microstructural evolution, reaction kinetics and interaction of LSM-YSZ composite was discussed thoroughly.

Chapter 3 presents the role of PO_2 on the stability of porous LSM-YSZ composite. This chapter focused on understanding the influence of PO_2 on the densification, stability and thermal expansion behavior of porous LSM-YSZ composites.

Chapter 4 describes other factors related to the interaction of LSM-YSZ composite, including sintering temperature, time, porosity and raw powder.

Chapter 5 presents the reversibility of the LSM-YSZ reaction and the prevention of the LSM-YSZ reaction. This reaction can be reversed by reinterring the samples at higher PO_2 than the original PO_2. The reversibility was also proved by the $La_2Zr_2O_7$ and MnO_2 reaction to form ZrO_2 and $LaMnO_3$. The LSM-YSZ reaction can be retarded by doping YSZ with Mn.

Chapter 6 presents the improvement of the durability of SOEC by Mn modified YSZ. The electrochemical performance was improved by Mn-doing YSZ interlayer between electrode and electrolyte, and the delamination was mitigated by a porous interlayer.

Chapter 7 provides a brief summarization for this dissertation followed by recommendations for the future work for the development of solid oxide cells.

Chapter 2 Role of PO_2 on the Stability of Dense LSM-YSZ Composite

2.1 Introduction

This chapter describes the role of oxygen pressure on microstructural evolution, reaction kinetics and interaction of LSM-YSZ composite. Carbon black was chosen as pore former to get dense sample. A sintering temperature of 1400°C was selected to represent the device sintering condition. An oxygen partial pressure range of 0.21 to 10^{-6} atm was selected to study the phase interaction and microstructural evolution.

2.2 Experimental Section

2.2.1 Sample Preparation

LSM ($La_{0.8}Sr_{0.2}MnO_3$, surface area 4.66 m^2/g, Fuel Cell Materials, Ohio), YSZ (surface area 4.7 m^2/g, Fuel Cell Materials, Ohio), and carbon black (density 1.8 g/cm^3, Cabot Corporation, Massachusetts) powders in 1:1:0.12 mass ratio were ball milled for 24 h using zirconia balls and ethanol. Carbon black powder serves as pore former to obtain ~30 vol% pores in the sample after bisque firing. The mixed powder batch was dried for 24 h and pressed into pellets. The LSM-YSZ pellets were bisque fired in air at 1000°C for 2 h in order to burn out carbon.

The bisque fired samples were subsequently sintered at 1400°C for 10 h in flowing dry air (PO_2 ~0.21 atm), 1000 ppm O_2 (PO_2 ~10^{-3} atm), and 1 ppm O_2 (PO_2 ~10^{-6} atm) in a tube furnace (Model No. 0300334, CM Inc. New Jersey) at a nominal flow rate of 20 sccm. The sintering atmosphere was achieved by using certified gasses (Airgas, Connecticut) comprised of O_2 and N_2. For all the sintering experiments, the heating and cooling rates were 3°C/min.

2.2.2 Characterization

The bulk densities of the sintered LSM-YSZ samples were measured by Archimedes method following ASTM C20-97 standard. The densities of at least five samples for each sintering atmospheres were measured. Average density is reported.

X-ray diffraction (XRD) studies, using a Bruker D8 Advance diffractometer (Bruker AXS Inc., Madison, WI) were carried out to identify the structure and phases present in the sintered LSM –YSZ composite. The scan step was 0.04° with CuK_{α} radiation (λ =1.5406 Å).

The LSM-YSZ samples were polished to optical finish. The polished samples were cleaned in an ultrasonic bath with water and dried and wiped with ethanol. The microstructures of the polished samples were examined using scanning electron microscope (SEM, Quanta 600, FEI Company, Hillsboro, OR). The energy dispersive spectroscopy (EDS) module attached to the SEM was used to analyze the elemental composition of various phases in the sintered samples. A minimum of ten EDS spot analysis was carried out for each phase. The average elemental composition is reported.

The transmission electron microscopy (TEM) and scanning transmission electron microscopy (STEM) specimens described in this paper were prepared using a focused ion beam (FIB) instrument (FEI strata 400S, FEI Company, Hillsboro, OR, 30 keV Ga+ ions) with a dual-beam column, combining a scanning electron beam and an ion beam in one unit. The dual beam allows high-resolution imaging of the surface of the sample during the ion-beam milling process. An Omniprobe nanomanipulator (Omniprobe Auto Probe ^{TM} 200) is used for the in situ TEM specimen lift-out technique. For the current study, a sample thickness between 75-100 nm provides suitable results. TEM studies and STEM-XEDS line scans were performed using Tecnai T12 TEM. In STEM-XEDS line scan, a series of spectra were acquired while the beam

was scanning along a defined line. The elemental distribution profiles were obtained by selecting the energy windows of a particular element.

2.3 Results

2.3.1 Density

93-95% theoretical density is obtained for the LSM-YSZ composites. Slight decrease in the density is observed with decreasing oxygen partial pressure. At high theoretical density, the effect of PO_2 on the densification is not significant.

2.3.2 XRD

The role of sintering atmosphere on the compound formation and structural changes in the LSM-YSZ composites, as identified by XRD, is shown in Figure 2.1. Cubic zirconia (JCPDS number: 00-030-1468) is observed for all the samples regardless of sintering atmosphere. Rhombohedral LSM (JCPDS number: 00-053-0058) is observed for the samples sintered in air. Rhombohedral (JCPDS number: 00-074-8264) LSM, cubic $La_2Zr_2O_7$ (JCPDS number: 00-017-0450), and MnO_x (Mn_3O_4 JCPDS number: 00-024-0734) phases are found for the samples sintered in 10^{-3}atm and 10^{-6} atm PO_2. Although rhombohedral LSM is observed for the samples sintered in 10^{-3}atm and 10^{-6} atm PO_2, the shift in XRD pattern indicates that the lattice parameters are different from that of air sintered samples leading to higher unit cell volume. These observations indicate that sintering atmosphere significantly influences the phase evolution and the structure of LSM.

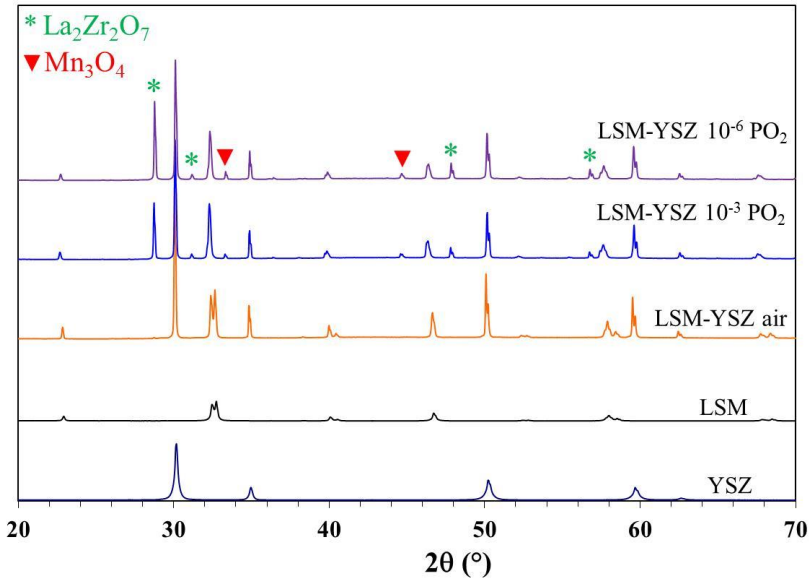

Figure 2.1 XRD patterns of the LSM-YSZ composites in different sintering atmospheres. Dotted lines show the shift in 2θ position for LSM with sintering atmosphere.

2.3.3 SEM-EDS

The microstructures of the polished LSM-YSZ composites sintered in different atmospheres are shown in Figure 2.2. For the sample sintered in air (Figure 2.2 (a)), both LSM and YSZ are homogeneously distributed. The grain size of these phases varies from 1.5 µm to 6 µm. The dark phases are YSZ (marked as 1) and bright phases are LSM (marked as 2) as confirmed by EDS analysis given in Table 2.1. However, Y and O are not considered in the EDS elemental analysis. The X-ray energies of Y and Zr are very close and could not be distinguished. The atomic number of oxygen is low for reliable quantitative analysis. The EDS analyses show the presence of ~ 7 at% La and ~ 10 at% Mn in the YSZ.

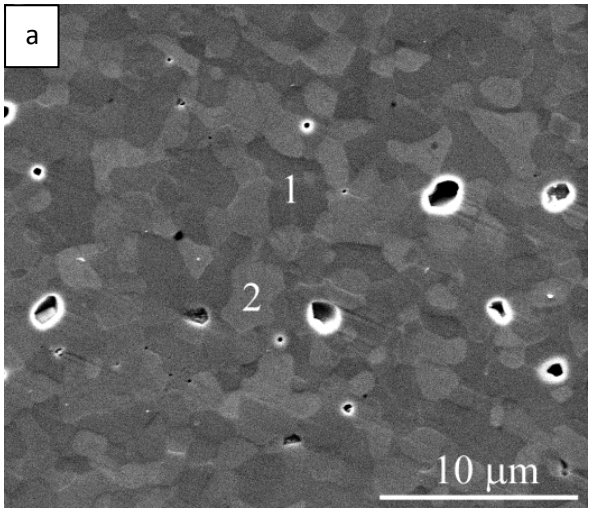
a
1
2
10 μm

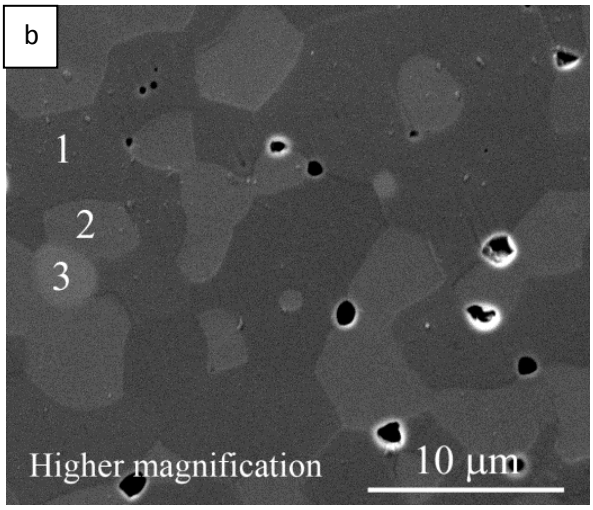
b
1
2
3
Higher magnification
10 μm

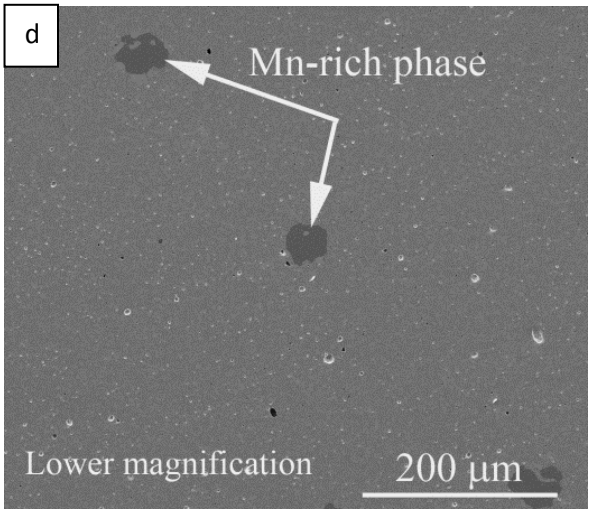
d
Mn-rich phase
Lower magnification
200 μm

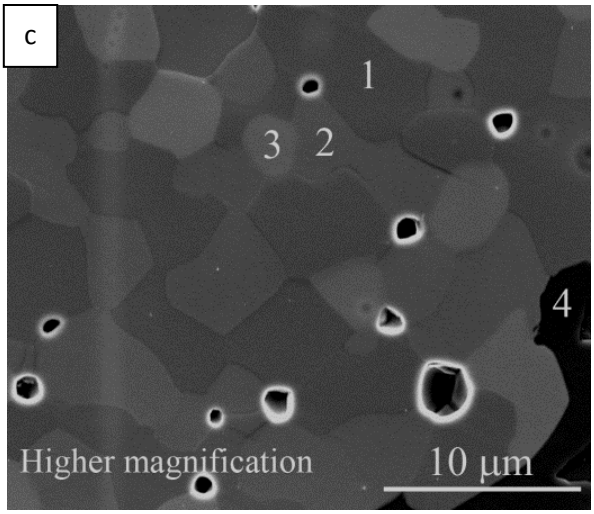
c
1
3
2
4
Higher magnification
10 μm

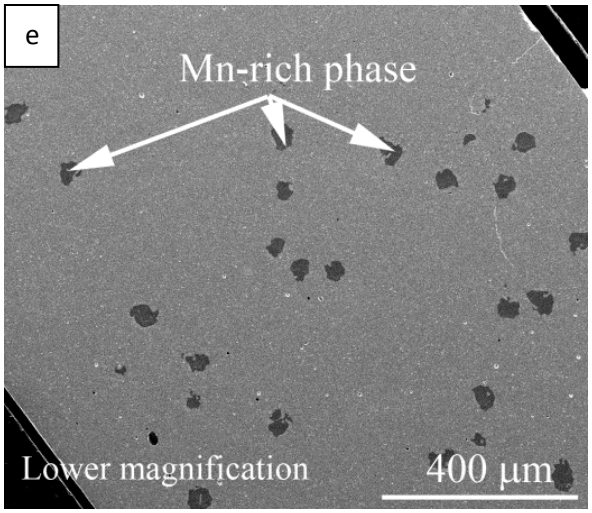
e
Mn-rich phase
Lower magnification
400 μm

Figure 2.2 SEM images of the polished LSM-YSZ samples sintered at 1400°C for 10 h in: (a) air, (b) 1000 ppm O_2, (c) 1ppm O_2, Low magnification images in (d) and (e) show the presence of Mn-rich phases in the bulk sample.

Table 2.1 Elemental composition from SEM-EDS analyzes of the observed phases in the LSM-YSZ composites sintered in different atmospheres in Figure 2.2

Sintering atmosphere		**Elements**				**Compounds**
		La	**Sr**	**Mn**	**Zr**	
Air						
	1	6.5±1.0		9.5±1.1	84.0±1.7	YSZ solid solution
	2	42.3±0.9	12.5±0.4	45.1±0.9		LSM
1000 ppm O_2						
	1	6.7±0.4		13.8±0.3	79.4±0.5	YSZ solid solution
	2	39.4±0.3	14.3±0.4	42.2±0.8	4.1±0.7	LSM
	3	43.8±0.5			55.7±0.5	$La_2Zr_2O_7$
1ppm O_2						
	1	7.5±0.6		15.0±0.8	77.6±1.3	YSZ solid solution
	2	41.5±1.1	13.2±0.5	42.5±1	2.8±1.0	LSM
	3	45.9±0.1			54.1±0.1	$La_2Zr_2O_7$

For the sample sintered in 10^{-3} atm PO_2, four distinct phases are observed (Figure 2.2(b)). The dark phase (marked as 1) is YSZ, grey colored phase (marked as 2) is LSM, the brighter phase (marked as 3) is $La_2Zr_2O_7$ and the darkest phase (marked in low magnification image in Figure 2.2 (d)) is MnO_x as confirmed by EDS analysis (Table 2.1). The LSM and YSZ are

homogeneously distributed. MnO_x phase (~ 30 µm, Mn_3O_4 as confirmed by XRD) is randomly distributed (Figure 2.2 (d)). The grain sizes of LSM, YSZ, and $La_2Zr_2O_7$ vary from 2-4 µm, 5-10 µm, and 1-3 µm respectively. The EDS analyses show the presence of ~ 7 at% La and ~ 14 at% Mn in the YSZ and ~ 4.5 at% Zr in the LSM.

For the sample sintered in 10^{-6} atm PO_2, four distinct phases are observed (Figure 2.2(c)). The dark phase (marked as 1) is YSZ, the grey colored phase (marked as 2) is LSM, the brighter phase (marked as 3) is $La_2Zr_2O_7$ and the darkest phase (marked as 4) is MnO_x as confirmed by EDS spot analyses (Table 2.1). The LSM and YSZ are homogeneously distributed. MnO_x phase of ~ 30 µm in size (Mn_3O_4 as confirmed by XRD) is randomly distributed (Figure 2.2(e)). The grain sizes of LSM, YSZ, and $La_2Zr_2O_7$ vary from 4-6 µm. The EDS analyses show the presence of ~ 7.5 at% La and ~ 15 at% Mn in the YSZ and ~ 3 at% Zr in the LSM.

2.3.3 TEM-EDS

The TEM images of the selected LSM-YSZ composites sintered in different atmospheres are shown in Figure 2.3 and Figure 2.4. While Figure 2.3 represents air sintered sample, Figure 2.4 represents the samples sintered in 10^{-6} PO_2, respectively. Because of better spatial resolution and lower sampling volume, TEM provides detailed morphological and compositional changes in the samples. For the sample sintered in air (Figure 2.3(a)), it has been observed that two phases are homogeneously distributed. The phases are identified as LSM and YSZ from the STEM-XEDS analysis given in Table 2.2. The grain sizes are 1-6 µm, consistent with SEM. Submicron sized grains are observed (marked as 3 and 6 in Figure 2.3(a)). Twins are also observed in the LSM grains. The compositions of the LSM and YSZ phases vary from grain to grain. 2-4 at% La and 4-5 at% Mn are present in the YSZ (marked as 1 and 2 in Figure 2.3(a)). Similarly, the LSM grains contain 30-46 at% La, 11-17 at% Sr, and 43 -51 at% Mn as given in

Table 2.2. STEM-XEDS line scan analysis was carried out along YSZ grain in-between two LSM grains (marked as A_1-A_2 line in Figure 2.3(a)). No secondary phase has been found at the LSM and YSZ grain boundaries. The concentration profiles of Zr and Mn elements are also shown in Figure 2.3 (b) and (c).

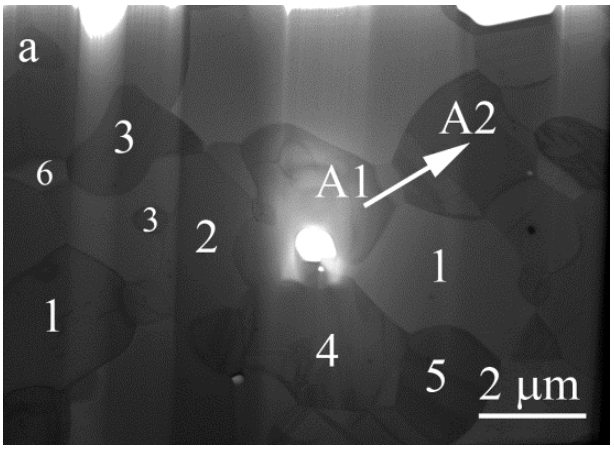

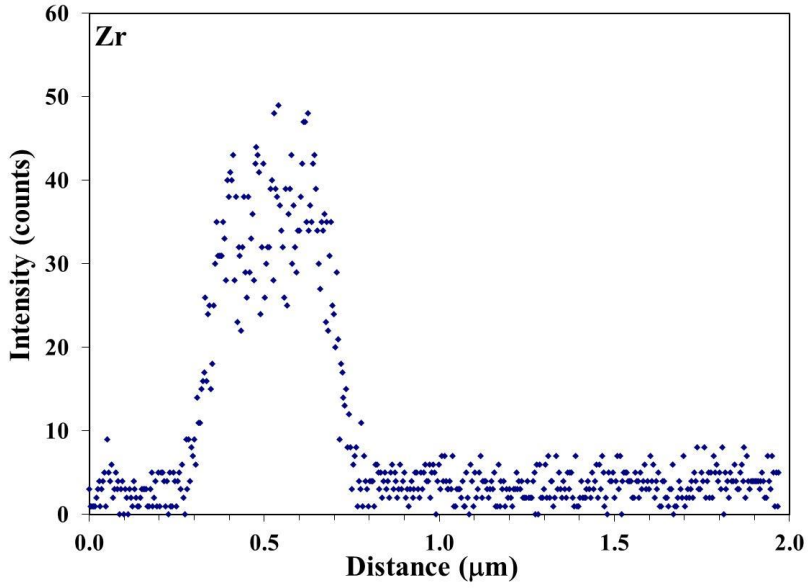

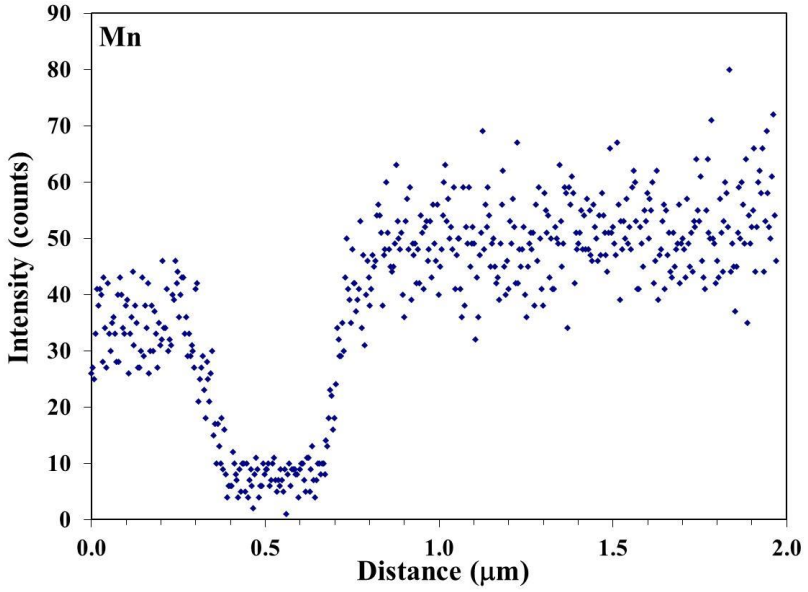

Figure 2.3 (a) TEM image of the LSM-YSZ composite sintered at 1400°C for 10 h in air. The concentration profiles of (b) Zr and (c) Mn are determined along the line A_1-A_2 in the TEM image.

For the sample sintered in 10^{-6} atm PO_2 (Figure 2.4 (a)), four different phases are observed. From the EDS analysis in Table 2.2, the phases are identified as LSM (marked as 1 and 2), YSZ (marked as 3), $La_2Zr_2O_7$ (marked as 4), and MnO_x (marked as 5). The MnO_x grain is elongated and oriented in a layer form. Due to the non-uniform distribution of these phases, the grain sizes could not be determined. The LSM composition varies from grain to grain. 3 at% La and 10 at% Mn are present in the YSZ. 4 at% Zr are found in some of the LSM grains. No secondary phase has been found at the LSM and YSZ grain boundaries, consistent with the concentration profiles of the La, Sr, Mn, Y, and Zr at the grain boundary. The TEM analysis, in all cases, shows the presence of twins in LSM grains and layered morphology of MnO_x phase and reveals that the LSM, YSZ, and $La_2Zr_2O_7$ grain compositions vary from grain to grain.

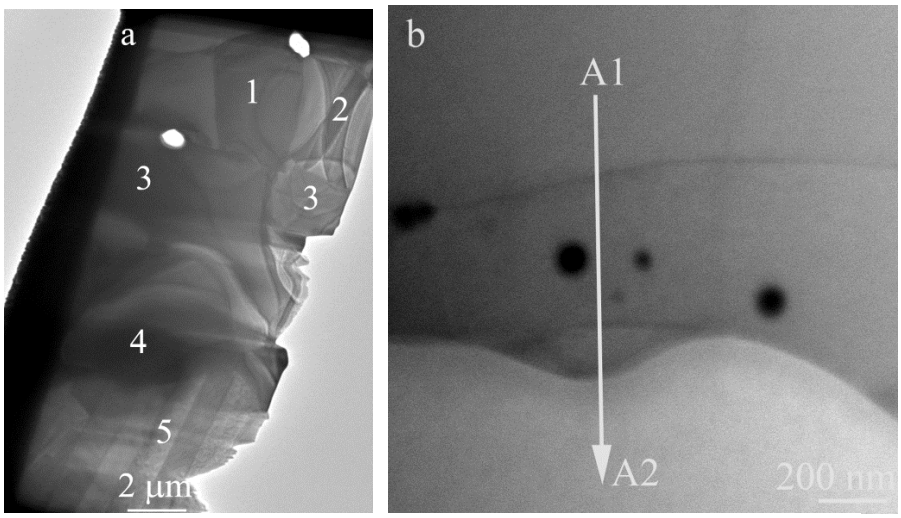
a
1
2
3
3
4
5
2 μm
b
A1
A2
200 nm

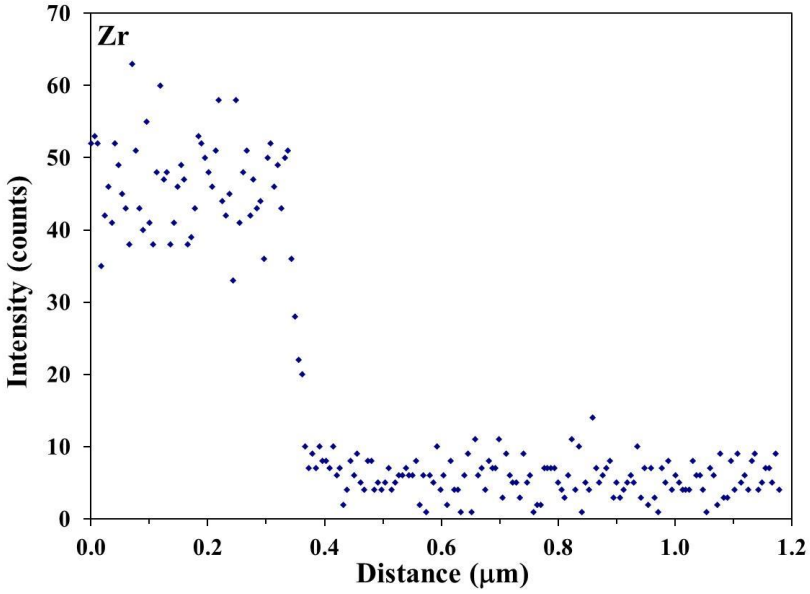
Zr
Intensity (counts)
Distance (μm)
0
10
20
30
40
50
60
70
0.0
0.2
0.4
0.6
0.8
1.0
1.2

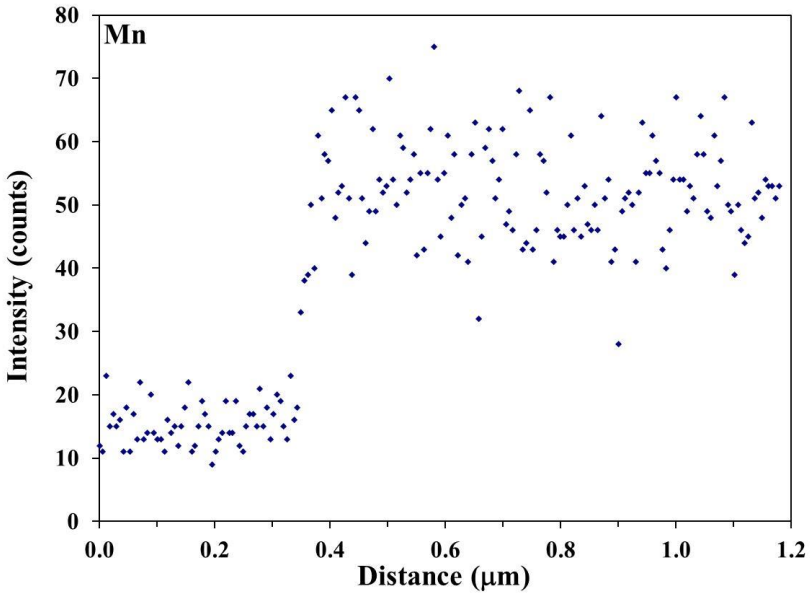
Mn
Intensity (counts)
Distance (μm)
0
10
20
30
40
50
60
70
80
0.0
0.2
0.4
0.6
0.8
1.0
1.2

Figure 2.4 (a) Low and (b) high magnification TEM images of the LSM-YSZ composite sintered at 1400°C for 10 h in 1ppm O_2 environment. The concentration profiles of (c) Zr and (d) Mn are determined along the line A1-A2 in the TEM image (b).

Because of better spatial resolution and lower sampling volume, TEM-EDS provide detailed morphological and compositional changes in the samples. For samples sintered in air, two phases are identified as LSM and YSZ. 2-4 at% La and 4-5 at% Mn are present in the YSZ. Similarly, the LSM grains contain 30-46 at% La, 11-17 at% Sr, and 43-51 at% Mn as given in Table 2.2. For brevity, concentration profiles of the elements are mot shown in the text. For the sample sintered in 10^{-6} atm PO_2, four different phases are observed. From the EDS analysis in Table 2.2, the phases are identified as LSM, YSZ, $La_2Zr_2O_7$, and MnO_x. 3 at% La and 10 at% Mn are present in the YSZ. 4 at% Zr is found in some of the LSM grains. No secondary phase has been found at the LSM and YSZ grain boundaries, consistent with the concentration profiles of the La, Sr, Mn, Y, and Zr at the grain boundary. The TEM analysis, in all cases, shows the presence of twins in LSM grains and layered morphology of MnO_x phase and reveals that the LSM, YSZ, and $La_2Zr_2O_7$ grain compositions vary from grain to grain.

Table 2.2 TEM-EDS analysis of LSM-YSZ composites (as shown in Figures 2.4 and 2.5)

Sintering atmosphere	**Elements**					**Compounds**
	La	**Sr**	**Mn**	**Zr**	**Y**	
Air						
1	1.3±0.2		4.4±0.3	82.7±0.8	12.2±0.5	YSZ Solid solution
2	5.2		4.9	79.0	10.9	YSZ Solid solution
3	35.2±1.4	14.1±1.2	50.5±1.4			LSM
4	31	17.3	50.1	2.7		LSM
5	46.1	10.8	43.0			LSM
6	33.6	14.4	50.7		1.3	LSM
1ppm O_2						
1	34.0	13.1	48.9	4.0		LSM
2	21.1	14.2	61.0	3.5		LSM
3	2.7±1.0	0.6±0.3	9.5±0.7	76.8±1.1	11.5±1.0	YSZ solid solution
4	28.3	0.6	0.5	67.9	2.9	$La_2Zr_2O_7$ and ZrO_2
5	1.8±1.0	0.2±0.1	98.3±1.2	1.1±0.5		MnO_x

2.4 Discussion

Above observations indicate that the sintering atmosphere affects the microstructural changes and the interaction between LSM and YSZ. The overall grain sizes of the LSM and YSZ phases are larger for the samples sintered in 10^{-3} atm and 10^{-6} atm PO_2 when compared to air sintered samples. Regardless of sintering atmospheres, ~ 7 at% La and 10-15 at% Mn are present in the YSZ. The amount of Mn in YSZ is higher (14-15 at%) for the samples sintered in 10^{-3} atm and 10^{-6} atm PO_2 but decreases to 10-12 at% on further sintering in air. For all the samples except the sample sintered in air, 2.5-5 at% Zr is observed in the LSM phases. For the sample sintered in air, no secondary phases are formed. $La_2Zr_2O_7$ and Mn_3O_4 phases evolve for the

samples sintered in 10^{-3} atm and 10^{-6} atm PO_2 atmospheres. The amounts of these phases are found to be higher for the samples sintered in 10^{-6} atm PO_2 as evident from the microstructures in Figs. 2b and 2c and also supported by the higher intensity of the $La_2Zr_2O_7$ and Mn_3O_4 phases in the XRD plots (Fig. 1). This infers that the extent of reaction between LSM and YSZ increases with decreasing oxygen partial pressure in the sintering atmospheres.

The effect of sintering atmosphere on the stability of LSM-YSZ composite will be discussed from several aspects: structural and morphological changes and reaction kinetics. Respective phase formation during the sintering in various gas atmospheres is shown in Tables 2.1 and 2.2. Mn ions diffuse readily in YSZ due to its smaller ionic radii and highest diffusivity among lanthanum and strontium ions.[153,154] The change in the lattice parameters of LSM structure is explained based on the changes in the valence state of manganese ions (Mn^{4+} to Mn^{3+}). In 10^{-3} atm and 10^{-6} atm PO_2, manganese ions reduce to lower valence state according to[155]

$$2Mn_{Mn}^{\bullet} + O_O^X = \frac{1}{2}O_2 + V_O^{\bullet\bullet} + 2Mn_{Mn}^X \quad (2.1)$$

$$2Mn_{Mn}^X + O_O^X = \frac{1}{2}O_2 + V_O^{\bullet\bullet} + 2Mn_{Mn}^{/} \quad (2.2)$$

where $V_o^{\bullet\bullet}$, $Mn_{Mn}^{\bullet}$, Mn_{Mn}^{x}, and $Mn_{Mn}^{/}$ are oxygen vacancy, Mn^{4+}, Mn^{3+}, and Mn^{2+} respectively. Reduction of Mn^{4+} and Mn^{3+} ions to larger Mn^{2+} ions increases the unit cell volume of the LSM.[156] Subsequently, the LSM lattice parameters are changed during sintering in 10^{-3} atm and 10^{-6} atm PO_2 leading to peak shifts in the XRD pattern. As the Mn^{2+} ion is more soluble into the YSZ than Mn^{3+} and Mn^{4+} ions due to the favorable ionic radii, the concentration of manganese ion in the YSZ is the highest for the samples sintered in 10^{-6} atm PO_2.[157]

Thermochemical stability and formation of $La_2Zr_2O_7$ phase due to the reaction between LSM and YSZ is influenced by the temperature and oxygen partial pressure. From La_2O_3-MnO_x-

ZrO_2 chemical potential diagram, lanthanum manganite and zirconia cannot coexist in equilibrium without $La_2Zr_2O_7$ formation at high temperatures (≥1000°C) according to the reaction[157]

$$LaMnO_3 + ZrO_2 = \frac{1}{2}La_2Zr_2O_7 + MnO_x + (\frac{3}{4} - \frac{1}{2}x)O_2 \quad (2.3)$$

The forward reaction rate (k) for the above reaction increases with decreasing PO_2 and formation of $La_2Zr_2O_7$ remains favorable in 10^{-6} atm PO_2. The $La_2Zr_2O_7$ phase field is asymmetric and according to defect cluster model, ZrO_2 excess $La_2Zr_2O_7$ is more stable than the stoichiometric and La_2O_3-excess $La_2Zr_2O_7$.[158] This is consistent with the EDS analyses (Tables 2.1 and 2.2).

2.5 Conclusion

The role of sintering atmosphere on the structural and chemical stability of $La_{0.8}Sr_{0.2}MnO_3$ (LSM)-8 mol% yttrium stabilized zirconia (YSZ) dense composite has been studied as a function of oxygen partial pressure at 1400^{o}C. The LSM and YSZ preferentially react to form $La_2Zr_2O_7$ and Mn_3O_4 phases in sintering atmospheres containing lower oxygen pressures. The unit cell volume of LSM increases with decreasing oxygen partial pressure because of changes in the manganese oxidation state.

Chapter 3 Role of PO_2 on the Stability of LSM-YSZ Porous Composite

3.1 Introduction

The present study is focused on understanding the influence of PO_2 on the densification, stability and thermal expansion behavior of porous LSM-YSZ composites. 40vol% starch powder was chosen as pore former to get porous sample. A sintering temperature of 1400°C was selected to represent the device sintering condition. An oxygen partial pressure range of 0.21 to 10^{-6} atm was selected to study the phase interaction and microstructural evolution.

3.2 Experimental Section

3.2.1 Sample Preparation

$La_{0.8}Sr_{0.2}MnO_3$ (particle size 0.5-1.8 μm, Inframat advanced materials, Connecticut), YSZ (particle size 0.3-1.4 μm, Fuel cell materials, Ohio) and starch powders (particle size 30-45 μm) were mixed in 1:1:0.33 weight ratio. The starch powder was used as pore former. Bulk porosity allows the samples to achieve uniform exposure to the controlled gas atmosphere. The mixed powders were uniaxially pressed into pellets at 100 MPa. The pressed pellets were bisque fired in air at 1000°C for 2 h to burn the pore formers. The bisque fired samples were subsequently sintered at 1400 °C in a range of PO_2 (0.21-10^{-6} atm). The sintering atmosphere was achieved by using certified gas mixtures consisting of oxygen and nitrogen (Airgas, Connecticut). The samples were sintered under a flowing gas atmosphere (flow rate of 40 sccm).

3.2.2 Characterization

The density of the LSM-YSZ samples was measured by Archimedes method according to ASTM C20-97 standard. Phase characterization was performed by XRD analysis using Cu Kα radiation (Bruker D8 advance X-Ray diffractometer). The semi-quantitative analysis to

determine the amount of $La_2Zr_2O_7$ phase was performed by using the ratio of the 100% intensity reflection of $La_2Zr_2O_7$ and YSZ, taking plane multiplicity factors M_{hkl} into account.[152,159]

The polished cross section was prepared using standard metallographic techniques and analyzed using SEM (Quanta 600 FEI Company, Hillsboro, OR). The EDS attached to the SEM was used for elemental analysis. The TEM specimens were prepared using a FIB instrument (FEI strata 400S, FEI company, Hillsboro, OR, 30 keV Ga+ ions) with a dual-beam column. An Omniprobe nanomanipulator (Omniprobe auto probe ^{TM} 200) was used for the in situ TEM specimen lift-out technique. TEM high resolution images, selected area diffraction pattern and TEM-EDS spot analysis were performed using JEOL 2010 FasTEM.

Thermal expansion properties were measured using the Netzsch 402PC dilatometer in air from room temperature to 1000°C with a heating rate 5°C/min. The sintered LSM-YSZ composite samples were cut to rectangular shape (10×2×3 mm) and used to measure TEC. Standard alumina rod was used for calibration. The dense YSZ and LSM samples sintered at 1400 °C for 10 h in air were used as reference for comparison.

3.3 Results

Sintered densities, compound formation, microstructure, elemental distribution, and thermal expansion are presented.

3.3.1 Density

Depending on the sintering atmospheres and time, the average densities of the LSM-YSZ composites are in the range of 65-85% of theoretical density as shown in Figure 3.1. The density of the LSM-YSZ composites increases from ~75% to ~80% while sintering atmosphere decreases from 0.21 to 10^{-6} atm PO_2 for sintering time of 10 h. The density of the LSM-YSZ composites also increases from ~67% to ~75% with increasing sintering time from 2 h to 10 h

for the samples sintered in air and similar trend is followed for the samples sintered in lower PO_2. It can be noted in Figure 3.1 that the density value of the LSM-YSZ sample are scattered within ± 5% and the deviation from the average value increases with lowering PO_2. It is also observed that the density of the composites sintered in 10^{-3} atm PO_2 for 10 h is higher (~85%) than the samples sintered in 10^{-6} atm PO_2 for the same time, however, within the standard deviation range for the 10^{-6} atm PO_2 sintering atmosphere. The large deviation from the average density values may be attributed to the distribution of pores in the samples. The amount of porosity may vary from sample to sample and accordingly the interaction volume of solids with sintering atmospheres varies resulting in large scattering in density values. Nonetheless, it can be concluded that the density of the LSM-YSZ composites increases with lowering PO_2 and prolonged sintering time.

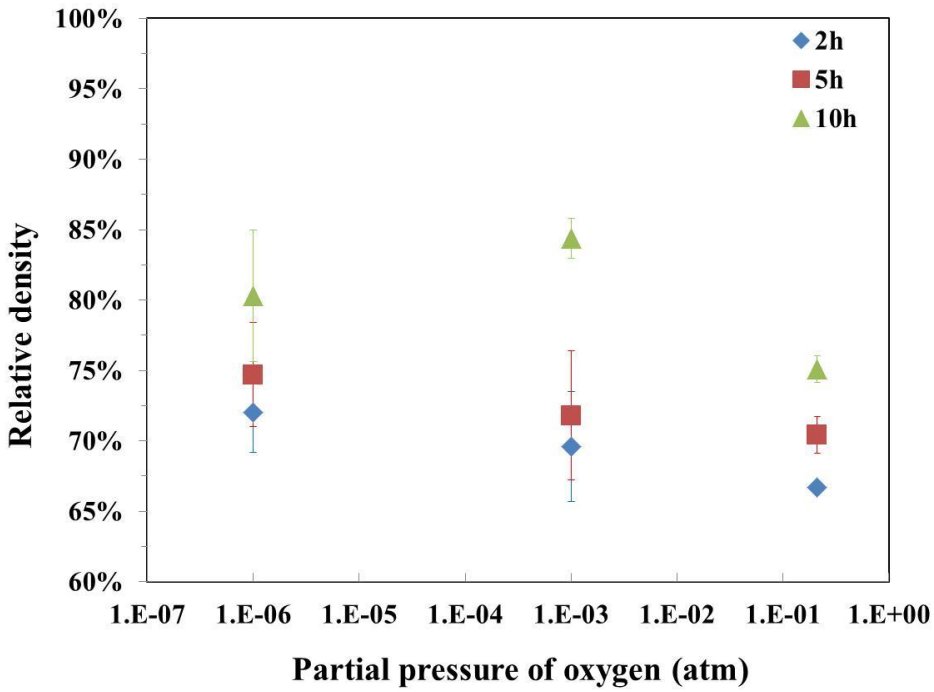

Figure 3.1 Relative density of LSM-YSZ composites sintered at 1400 ºC in different atmospheres

3.3.2 XRD

The effect of sintering atmosphere and exposure time on the compound formation in the LSM-YSZ composites were analyzed by XRD and shown in Figure 3.2. Cubic zirconia (JCPDS number: 00-030-1468) and rhombohedral LSM (JCPDS number 00-053-0058) are observed for all the samples. The crystal structure of the LSM and YSZ does not change with sintering condition as observed from the identical peak positions with that of raw powders. New phase, cubic $La_2Zr_2O_7$ (JCPDS number: 01-070-5602), is found for the samples sintered in air for 10 h only, and in 10^{-3} and 10^{-6} atm PO_2 for all the sintering times.

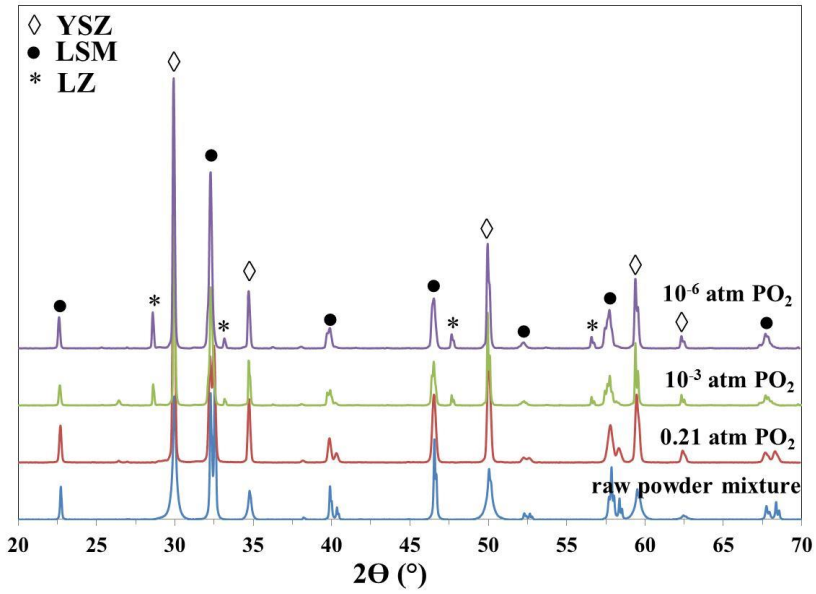

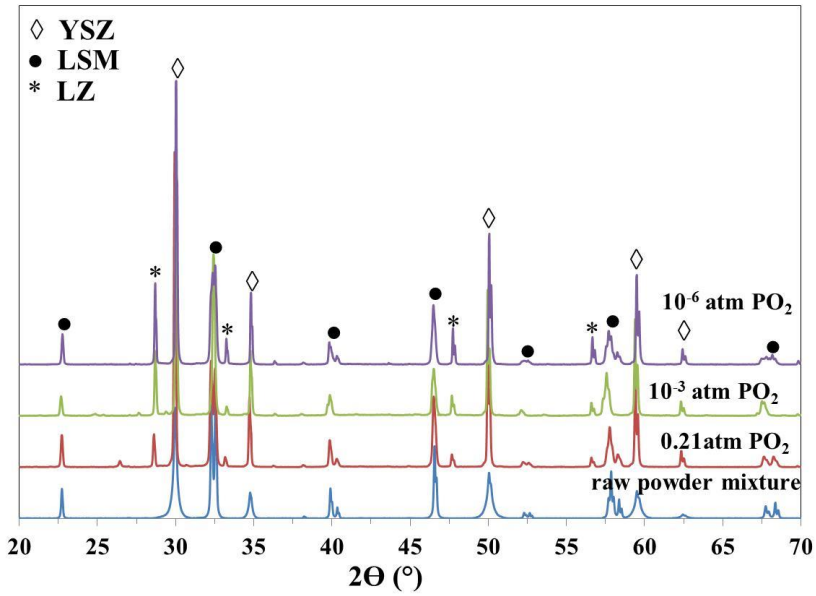

Figure 3.2 XRD patterns of the LSM-YSZ composites in different sintering atmospheres

(a) Samples sintered at 1400 °C for 2 h in 10^{-6} atm, 10^{-3} atm and air

(b) Samples sintered at 1400 °C for 10 h in 10^{-6} atm, 10^{-3} atm and air

The semi-quantitative content of $La_2Zr_2O_7$ was determined by the intensity ratio of X-ray diffraction line of the (222) plane of $La_2Zr_2O_7$ to that of (111) plane of YSZ. As those lines are the 100% intensity peaks of LZ and YSZ, respectively, and both peaks have same multiplicity factors (M_{hkl} = 8).[159] Figure 3.3 showed that the relative amount of LZ increases with decreasing PO_2 of sintering atmosphere and increasing sintering time. These observations indicate that reduced sintering atmosphere and the prolonged sintering time favor the formation of LZ.

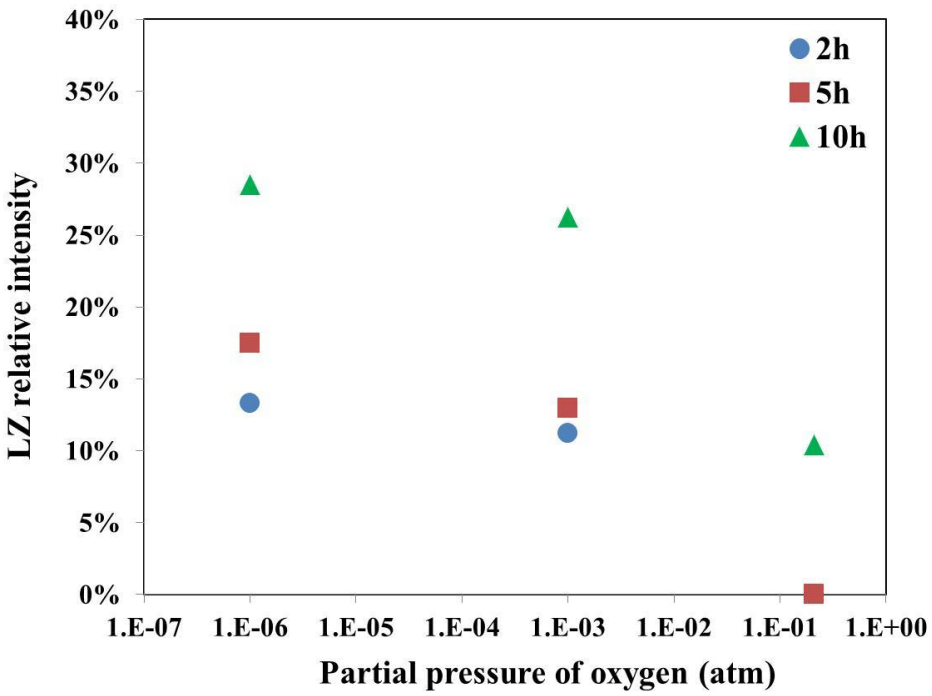

Figure 3.3 LZ/YSZ relative amount with different atmosphere for 2 h, 5 h and 10 h

3.3.2 SEM

Figure 3.4 shows the porosity of samples sintered at different experimental conditions. Porosity decreased with decreasing of PO_2. Porosity decreased with increasing sintering time. The SEM images agreed with the density measurement.

Figure 3.5 shows the microstructures of LSM-YSZ composites sintered under different experimental conditions. Figure 3.5 (a) shows the cross section of sample sintered at 1400°C in air for 2 h. Two main phases are homogeneously distributed into the samples. Color contrast and elemental analysis indicated the dark phases to be YSZ, the bright phases to be LSM. 5 h sintered samples have the similar character. The SEM image is not shown here for brevity. With the sintering time increased to 10 h (Figure 3.5 (b)), $La_2Zr_2O_7$ showed as the brightest contrast, under SEM observation.

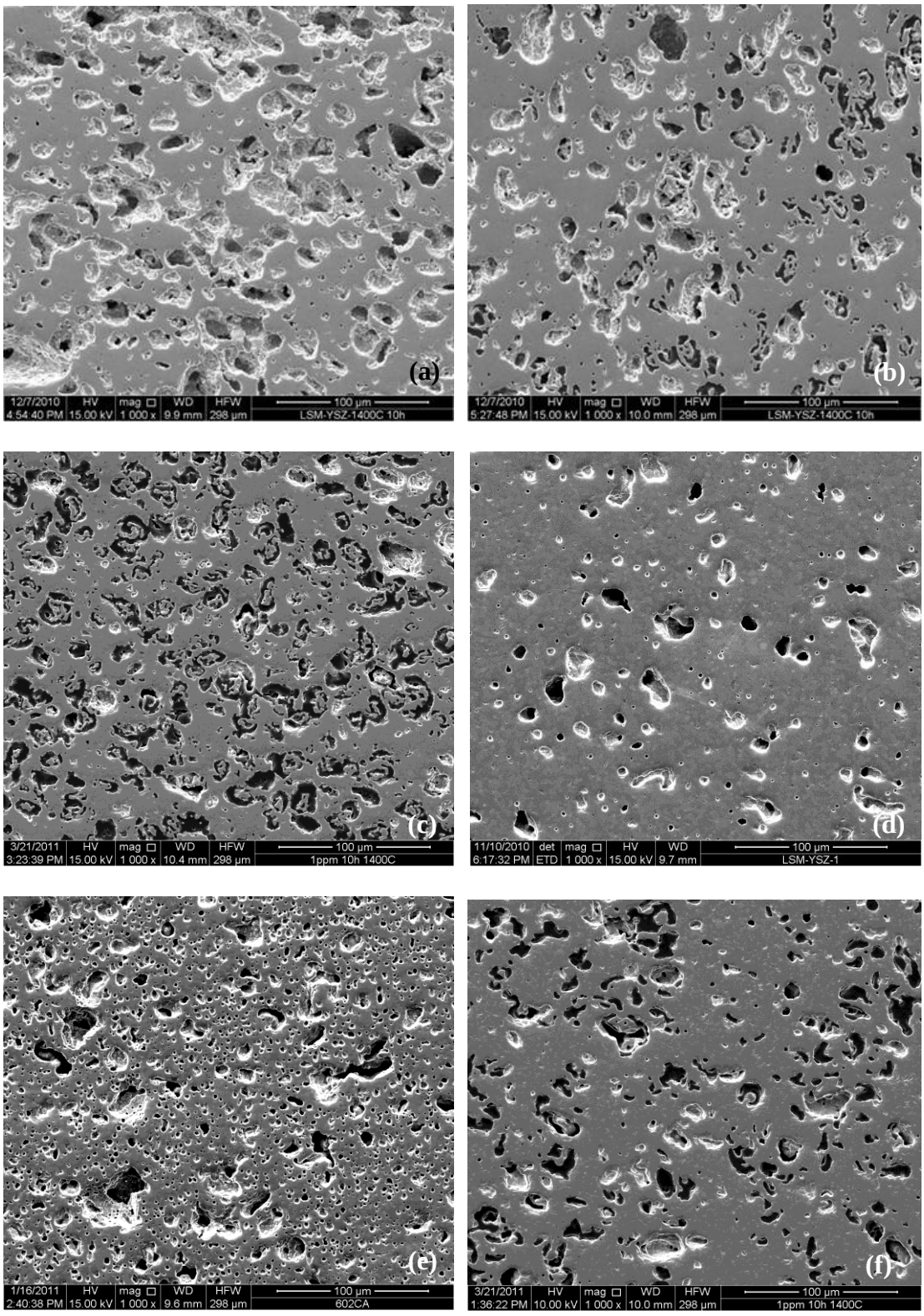

Figure 3.4 SEM of the cross section of samples sintered at 1400 °C in (a) air for 2h (b) air for 10 h (c) 10^{-3} atm PO_2 for 2h (d) 10^{-6} atm PO_2 for 10h (e) 10^{-6} atm PO_2 for 2h (f) 10^{-6} atm PO_2 for 10h

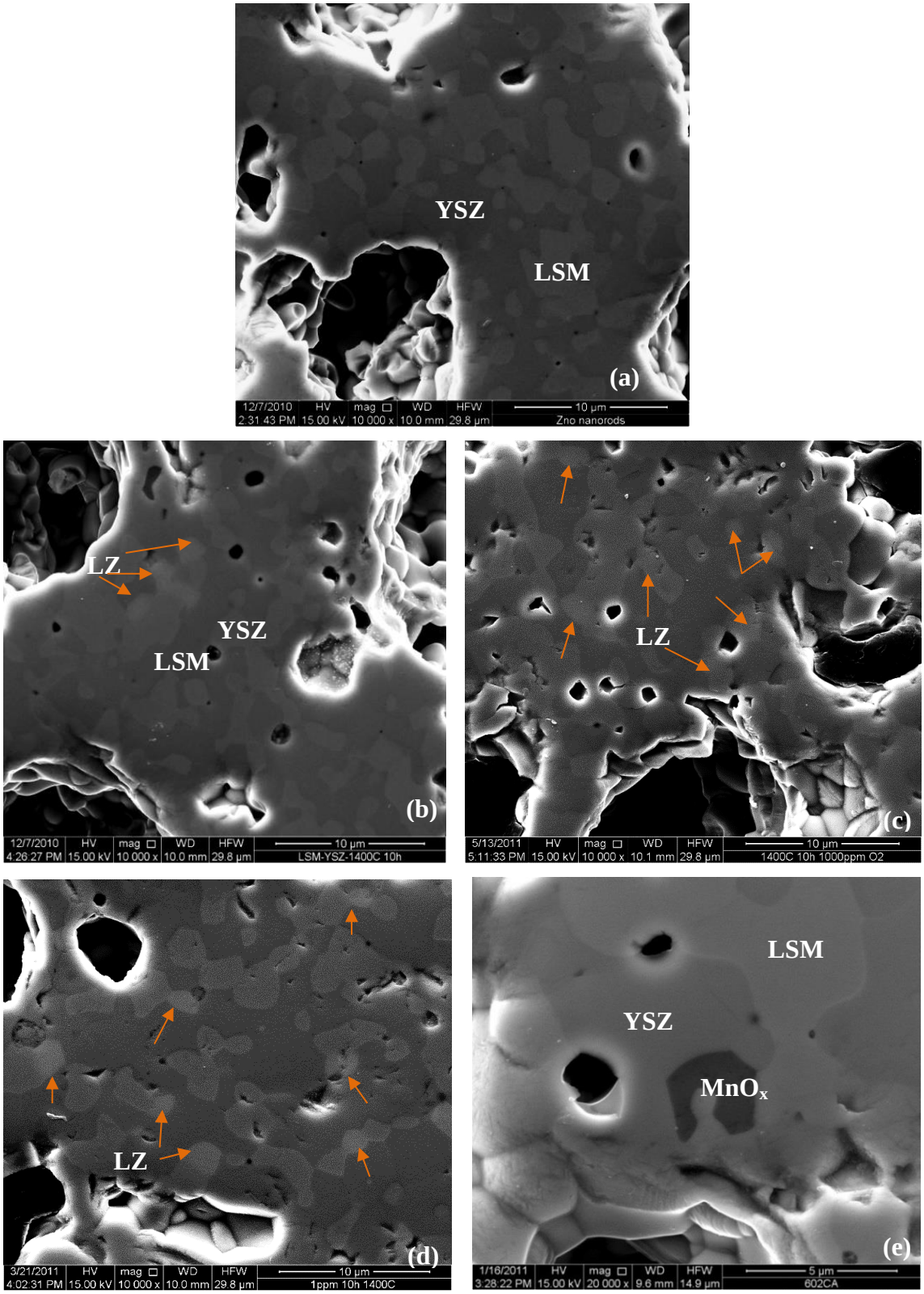

Figure 3.5 SEM of the cross section of samples sintered at 1400 °C in (a) air for 2 h (b) air for 10 h (c) 10^{-3} atm PO_2 for 10 h (d) and (e) 10^{-6} atm PO_2 for 10 h

All the samples sintered in 10^{-3} atm PO_2 shows three phases LSM, YSZ and LZ. In addition to the mentioned three phases, few MnO_x grains about ~2 µm size are also found in the samples sintered in 10^{-6} atm PO_2 as shown in Figure 3.5 (e). The $La_2Zr_2O_7$ phase is found after 2 h sintering in these low PO_2 condition. It is observed that the amount of the $La_2Zr_2O_7$ increase with lowering PO_2 and prolonging sintering time. The grain sizes of all the phases vary in a wide range for all the samples due to the variation in particle sizes of starting LSM (0.5-1.8 µm) and YSZ (0.3-1.4 µm) powders. The grain size increases with decrease in PO_2 (Table 3.1). For example, the average grain size of LSM and YSZ are 1.6 and 1.8 µm for LSM-YSZ composites sinter in air while those value increases to 2.9 and 2.7 µm for 10^{-3} atm PO_2 sintering atmosphere, 3.3 and 2.8 µm for 10^{-6} atm PO_2 sintering atmosphere. For LZ, the average grain size is around 2.0 µm for 10 h sintering in each sintering atmosphere.

Table 3.1 SEM-EDS results of LSM-YSZ composites sintered in different atmospheres

Preparation condition	**La**	**Sr**	**Mn**	**Zr**	**compounds**	**grain size (µm)**
Air	8	0	10	81	YSZ	1.8
1400 °C	36	13	43	7	LSM	1.6
10 h	40	2	2	56	LZ	2.1
10^{-6} atm PO_2	7	3	11	79	YSZ	2.7
1400 °C	41	13	44	2	LSM	2.9
10 h	39	2	3	56	LZ	1.9
10^{-3} atm PO_2	8	2	15	75	YSZ	2.8
1400 °C	39	13	45	3	LSM	3.3
10 h	41	2	4	53	LZ	2.0

The elemental composition of the observed phases was obtained by averaging the SEM-EDS spot analysis results (Table 3.1). For brevity, the elemental compositions of different phases obtained from EDS analysis are shown only for the samples sintered for 10 h because no significant difference in composition was found for the different sintering times. For the air

sintered sample, YSZ contains ~7 at% La and ~10 at% Mn, and LSM contains ~7 at% Zr. On changing the sintering atmosphere to 10^{-3} atm PO_2; YSZ shows ~7 at% La, ~11 at% Mn, and LSM shows ~2 at% Zr. In 10^{-6} atm PO_2 sintering atmosphere, Mn content in the YSZ increased to ~14 at% while the contents of the other elements remained similar to those observed in the 10^{-3} atm PO_2 sintering atmosphere. The increased amount of Mn in YSZ and reduced amount of Zr in LSM in the samples sintered in 10^{-6} atm PO_2 compared to those of the air sintered samples suggest that the elemental diffusion from LSM into YSZ becomes more pronounced with decreasing PO_2 compare to diffusion from YSZ into LSM.

3.3.3 TEM

For better understanding of the elemental distribution, a thin sample (150-200 nm) having all the three phases (LSM, YSZ and $La_2Zr_2O_7$) was prepared using focus ion beam from the LSM-YSZ composite sintered in 10^{-6} atm PO_2. Fig. 7(a) showes a high-resolution bright field image taken with TEM. YSZ, LSM, and LZ grains was observed and confrmed by TEM-EDS analysis (Table 3.2). The LZ grains were characterized by selected area electron diffraction (SAED). Fig. 7(b) shows the fcc pyrochlore structure of LZ with the zone axis of [011].

Table 3.2 TEM-EDS results for LSM-YSZ sample sintered at 1400 °C in 10^{-6} atm PO_2 for 10h

Preparation condition	**La**	**Sr**	**Mn**	**Y**	**Zr**	**compounds**
10^{-6} atm PO_2	8.5	0	10.6	13.4	67.5	YSZ
1400 °C	52.0	8.4	36.1	0.7	2.8	LSM
10 h	56.4	0	0.5	4.1	39.0	LZ

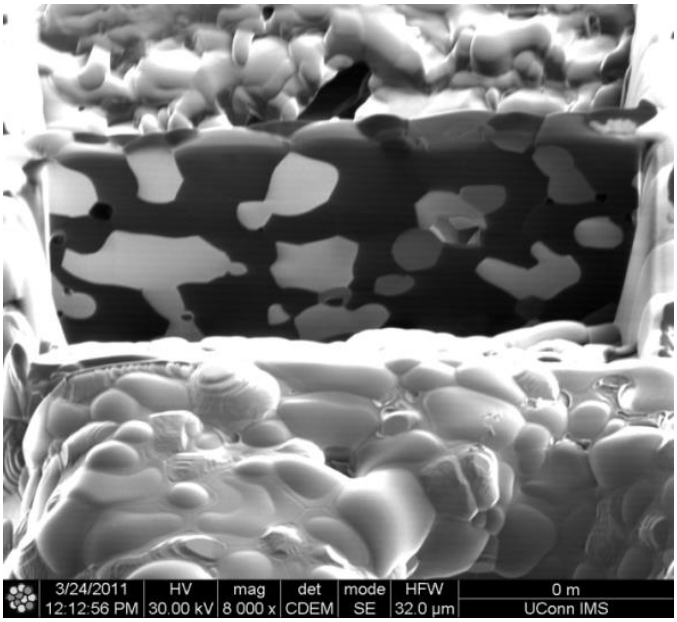

Figure 3.6 A typical sample prepared by FIB

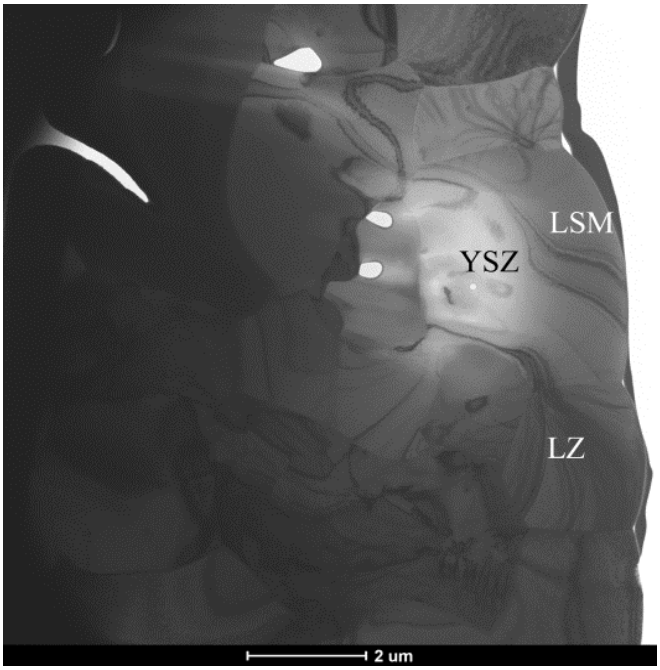

Figure 3.7 TEM image of smaple sintered at 1400 °C in 10^{-6} atm PO_2 for 10 h

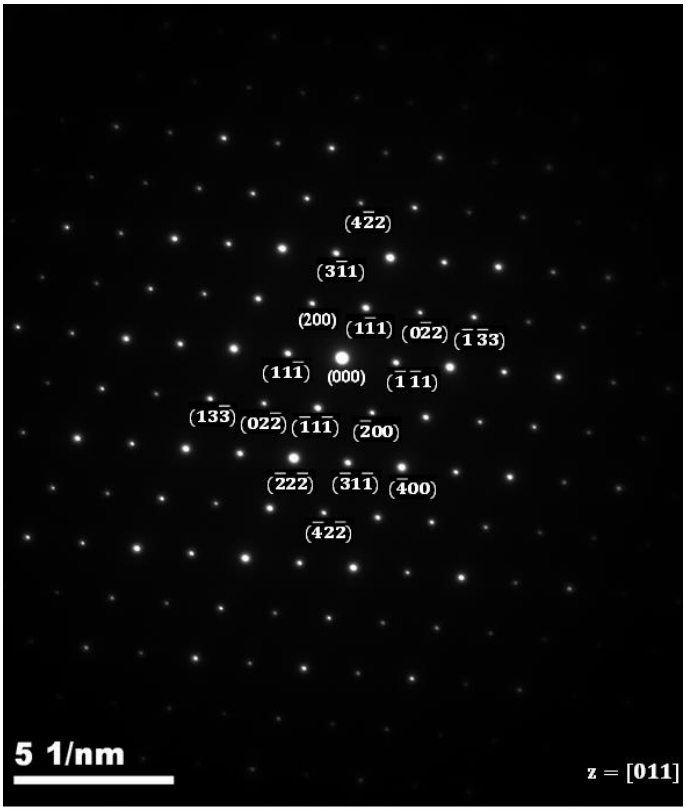

Figure 3.8 Selected area diffraction pattern of LZ with the zone axis [011]

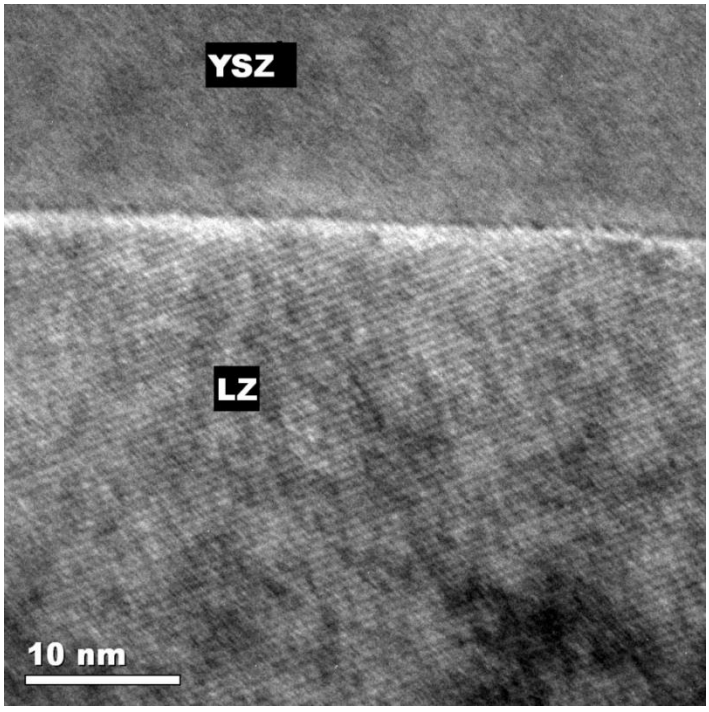

Figure 3.9 Lattice image of YSZ/LZ interface with the zone axis [011]

3.3.4 Thermal Expansion Coefficients

The thermal expansion coefficients of the porous LSM-YSZ composites are shown in Table 3.3. The TECs of dense YSZ and LSM are also shown for reference purposes. The TEC values of the LSM and YSZ are 12.3×10^{-6} /°C and 10.8×10^{-6} /°C respectively from room temperature to 1000 °C, consistent with literature[155,160,161,162]. The TEC of the LSM-YSZ composite sintered in air for 2 h at 1400 °C is 11.5 $\times10^{-6}$ /°C, and is in agreement with the mixing rule of composite. For the samples sintered in lower PO_2, the TEC value decreased from 11.5 to 10.3×10^{-6} /°C. Lowing of the TEC is assigned to the presence of $La_2Zr_2O_7$ phase in the samples sintered in 10^{-3} and 10^{-6} atm PO_2. The TEC values of $La_2Zr_2O_7$ were reported in the range of $9.0\text{-}9.3\times10^{-6}$ /°C [152,163,164].

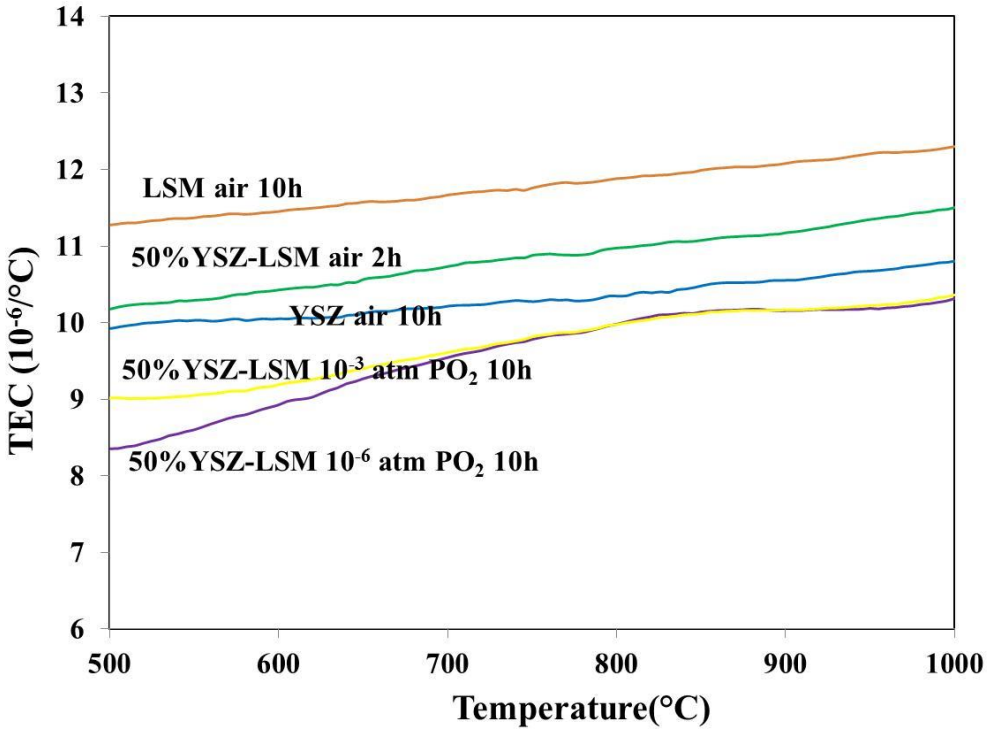

Fig 3.10 Thermal expansion coefficients of LSM, YSZ and LSM-YSZ composite

Table 3.3 Thermal expansion coefficient (from room temperature to 1000 °C) of samples related in this study

Composition	TEC ($\times 10^{-6}$/°C) This study	TEC ($\times 10^{-6}$/°C) Reference
YSZ	10.8	10.3[160],10.9[161]
LSM	12.3	11.7[161], 11.6[162]
LZ		9[152], 9.2[163], 9.3[164]
YSZ-LSM sintered in air for 2h	11.5	
YSZ-LSM sintered in 10^{-3} atm PO_2 for 10h	10.3	
YSZ-LSM sintered in 10^{-6} atm PO_2 for 10h	10.3	

3.4 Discussion

The PO_2 range used in the present work (0.21–10^{-6} atm) is well within the chemical and structural stability region for both LSM and YSZ.[165] The technical discussion is focused on observations related to (a) higher solubility of Mn in YSZ at lower PO_2 (b) enhanced densification with decrease PO_2 (c) increased formation of LZ at lower PO_2 (d) presence of MnO_x at lower PO_2.

Presence of Mn (8-14%) in YSZ has been reported during the sintering of LSM-YSZ. Mn ions diffuse readily in YSZ due to its smaller ionic radii and highest diffusivity among lanthanum and strontium ions.[134,143] The Mn in solid solution is a mixture of Mn^{3+} and Mn^{2+}.[166] The diffusion of Mn from LSM into YSZ changes the oxygen stoichiometry, (La+Sr) to Mn ratio in LSM will also be influenced.[167,168] At lower PO_2, manganese ions reduce to lower valence state according to (1), (2). Oxygen vacancies increase due to change in the oxidation state of

manganese ions as stated above.[153] Substitutional of Mn at Zr sites also has the tendency to increase the oxygen ion vacancy according to reactions:

$$MnO_{ZrO_2} = Mn''_{Zr} + V_O^{\bullet\bullet} + O_O^X \quad (3.1)$$

It has been calculated that the MnO_x solubility in c-ZrO_2, the amounts of Mn^{2+} and Mn^{3+}, vary with PO_2.[165] In lower PO_2 region, mainly Mn^{2+} dissolves in ZrO_2 and its solubility is higher than Mn^{4+} and/or Mn^{3+} solubility in air. As a result, the amount of manganese in ZrO_2 increases from 10 at% Mn to 14% while sintering atmosphere changes from air to 10^{-6} atm PO_2. Our experimental findings confirm and validate the theoretical evaluation.[167]

The overall grain sizes of the LSM-YSZ composites sintered in 10^{-3} atm and 10^{-6} atm PO_2 are larger than those for the samples sintered in air. In reduced atmospheres, oxygen vacancies increase due to change in the oxidation state of manganese ions as stated above (reactions 1 and 2). The oxygen vacancies enhance the atomic mobility to the grain boundaries and free surfaces causing the development of larger grain sizes. For LSM, cation mobility has been reported to be rate-limiting for sintering.[169] The oxygen vacancies enhance the cation mobility for sintering,[170,171] so the densification increased with the decrease of the oxygen partial pressure.

The formation of lanthanum zirconate phase is influenced by PO_2 and can be discussed from two aspects. Firstly, La_2O_3-MnO_x-ZrO_2 chemical potential diagram shows that lanthanum manganite and zirconia cannot coexist in equilibrium without $La_2Zr_2O_7$ formation at high temperatures ($\geq$ 1000°C).[157] The forward reaction rate of the reaction (4) increases with decreasing PO_2 and favoring lanthanum zirconate formation in lower PO_2. Secondly, the diffusivity of manganese is the highest among all the elements in LSM (La, Sr, and Mn), supported by the highest amount of Mn (10-14 at%) in YSZ followed by La (7-8 at%) and Sr (0-

2 at%) from our EDS data. While Mn diffusion to YSZ initiates the reaction between YSZ and LSM, and then the interdiffusion of La and Zr result in the formation of LZ. The Gibbs free energy value for formation of $La_2Zr_2O_7$ (-146.2 ± 5.0 kJ/mol at 1200 K) is more negative than that of $SrZrO_3$ (-92.01 kJ/mol at 1200 K).[151, 172] Also, the activation energy for $La_2Zr_2O_7$ formation (17.5 ± 1.8 kJ/mol) is lower than that of $SrZrO_3$ (18.8 ± 1.9 kJ/mol).[123]As a result, a large amount of $La_2Zr_2O_7$ but no $SrZrO_3$ is observed in this study.

Manganese oxide has been observed in the LSM-YSZ composites sintered in 10^{-6} atm PO_2 but not in air and 10^{-3} atm PO_2. The absence of manganese oxide for these samples can be explained as follows. First, more MnO_x was produced due to the reaction in 10^{-6} atm PO_2, consistent with the results obtained from microstructural study. Second, MnO_x formed due to the reaction (4) evaporated at 1400 °C as supported by its deposition on the crucible and tube in the furnace. As a result, MnO_x is only found for the sample sintered only in 10^{-6} atm PO_2. These arguments are also supported by our previous study where MnO_x is found for all the dense samples with zirconate phases.[173]

3.5 Conclusion

The stability of porous LSM-YSZ composite has been examined as a function of oxygen partial pressure and time during sintering at 1400 °C. Elemental inter-diffusion across the LSM-YSZ grain boundaries as well as the thermodynamic stability of the LSM-YSZ composite in the studied conditions causes the formation of new compounds such as $La_2Zr_2O_7$ and MnO_x. The chemical and microstructural stability of the LSM-YSZ composite preferentially degrade with lowering PO_2 during sintering because of the formation of higher amount of the new compounds and creation of oxygen vacancies due to manganese dissolution in the YSZ. Thermal expansion coefficient decreases with increase in the amount of the zirconate phases.

Chapter 4 Other Factors Affecting the LSM-YSZ Reaction

4.1 Introduction

This chapter examines other factors during the sintering of LSM-YSZ composite, including sintering temperature, time, and porosity and raw powder on the stability LSM-YSZ composite. The samples with and without pore former was prepared to evaluate the role of porosity. The different sources of LSM powder were used to evaluate the role of raw powder.

4.2 Experimental Section

The mixed LSM and YSZ powders were pressed into pellets at 100 MPa. Then the pellets were bisque fired in air at 1000°C for 2 h. The bisque fired samples were subsequently sintered at controlled atmosphere. Certified gas (Airgas, Connecticut) at fixed flow rate of 40 sccm was used in all the sintering experiments. The samples were sintered at different temperature 1200ºC, 1300ºC, 1400ºC and 1500ºC to evaluate the role of sintering temperature. The samples were sintered for different time, 2h, 5h, and 10h to evaluate the role of sintering time.

The dense sample and porous samples were prepared to evaluate the role of porosity. The dense samples were prepared without adding any pore former, the powder weight ratio is LSM: YSZ = 1:1. The porous samples were prepared with starch powder as pore former, the powder weight ratio is LSM: YSZ: starch = 1:1:0.33. All the other samples in this chapter were prepared with pore formers if not mentioned specially.

8YSZ powder was from Fuel cell materials, Ohio. Two different sources of $La_{0.8}Sr_{0.2}MnO_3$ powder were used to evaluate the role of raw powder, the coarse powder (particle size is) from Inframat Advanced Materials, Connecticut; the fine powder (particle size is about) from Fuel Cell Materials, Ohio. All the other samples in this chapter were prepared with LSM from Inframat Advanced Materials if not mentioned specially.

Phase characterization was performed by XRD analysis using Cu Kα radiation (Bruker D8 advance X-Ray diffractometer). The polished cross section was prepared using standard metallographic techniques and analyzed using SEM and the attached EDS (Quanta 600 FEI Company, Hillsboro, OR).

4.3 Results and Discussion

4.3.1 Sintering Temperature

The XRD pattern of LSM-YSZ samples sintered in air for different temperature was shown in Figure 4.1. LZ peak was not found for samples fired at 1000°C, sintered at 1200°C, and 1300°C. However, when the sintering temperature increased to 1400°C, LZ was detected.

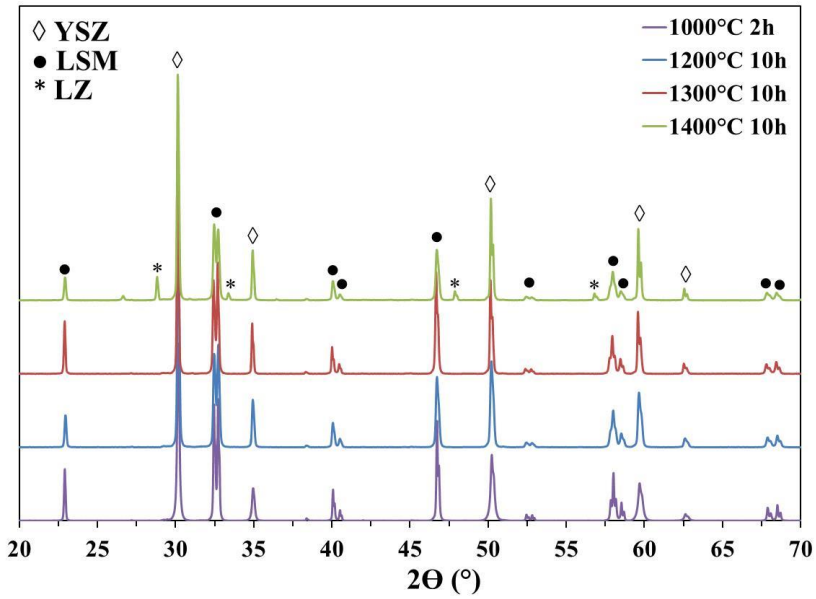

Figure 4.1 XRD patterns of the LSM-YSZ composites sintered in air at 1200°C, 1300ºC and 1400°C.

Figure 4.2 shows the SEM image for samples sintered in 10^{-6} atm PO_2 for 5h at 1400ºC and 1500°C. Sintered at 1400°C, LZ phase (determined by EDS) showed the brightest contrast. With the temperature increased to 1500°C, the samples showed the brightest LZ phase and the

darkest MnOx phase. Figure 4.3 shows the XRD pattern for these two samples sintered at 1400°C and 1500°C, with the raw powder mixture as reference. MnO_x content is probably very low, not shown in both samples. The LZ peak showed in both sample, but the 1500°C sintered sample has higher relative LZ content than 1400°C sintered sample. It suggested that the reaction between LSM and YSZ showed in equation (4) was pushed forward as the temperature increased. The reaction was so intense that not only the LZ phase but the MnOx phase showed in the bulk.

High temperature enhanced the reaction between LSM and YSZ. LZ was not formed at low temperature in air, but formed with the temperature increased to 1400°C. LZ and MnOx content were increased with the temperature increase from 1400ºC to 1500ºC in 10^{-6} atm PO_2. This phenomenon can be explained as the high temperature lowers the activation energy for $La_2Zr_2O_7$ formation.

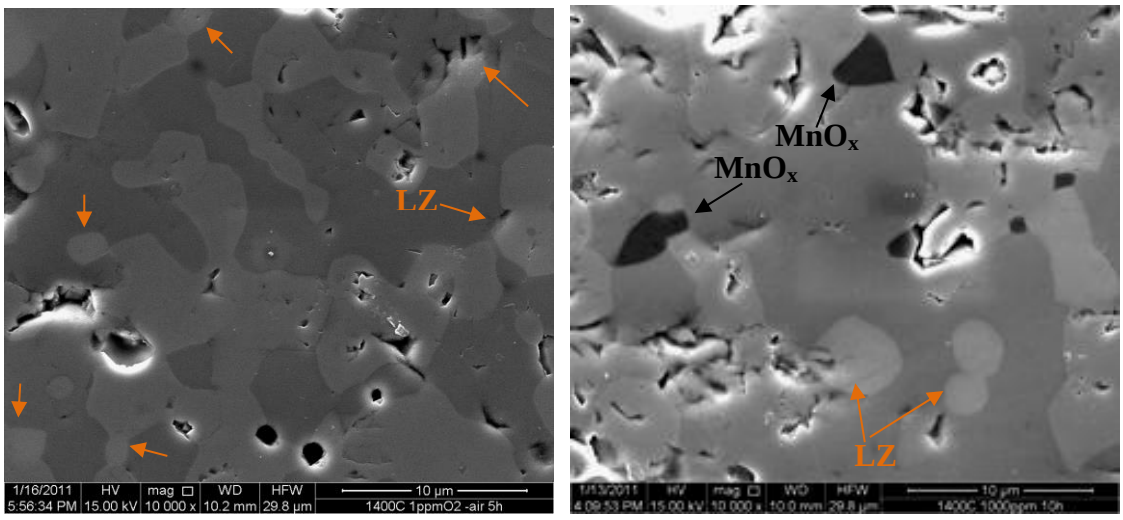

Figure 4.2 SEM image of samples sintered in 10^{-6} atm PO_2 for 5h at (a) 1400ºC (b) 1500°C

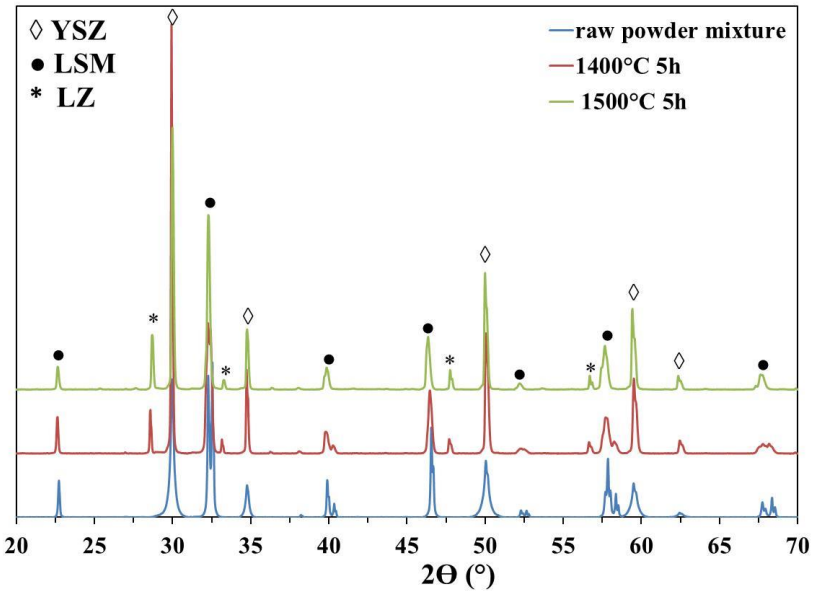

Figure 4.3 XRD patterns of the LSM-YSZ composites sintered in 10^{-6} atm O_2 at 1400ºC and 1500ºC for 5h

4.3.2 Sintering Time

LZ was preferred to be formed in lower PO_2. Sintered in ambient air, LZ is hard to be formed. If the reaction time is long enough, LZ still can be formed. LZ was not formed after sintering for 2h. When the sintering time increased to 10h, LZ was formed. LZ was formed after 2h sintering in 10^{-3} and 10^{-6} atm, with the increase of sintering time, LZ relative content was increased.

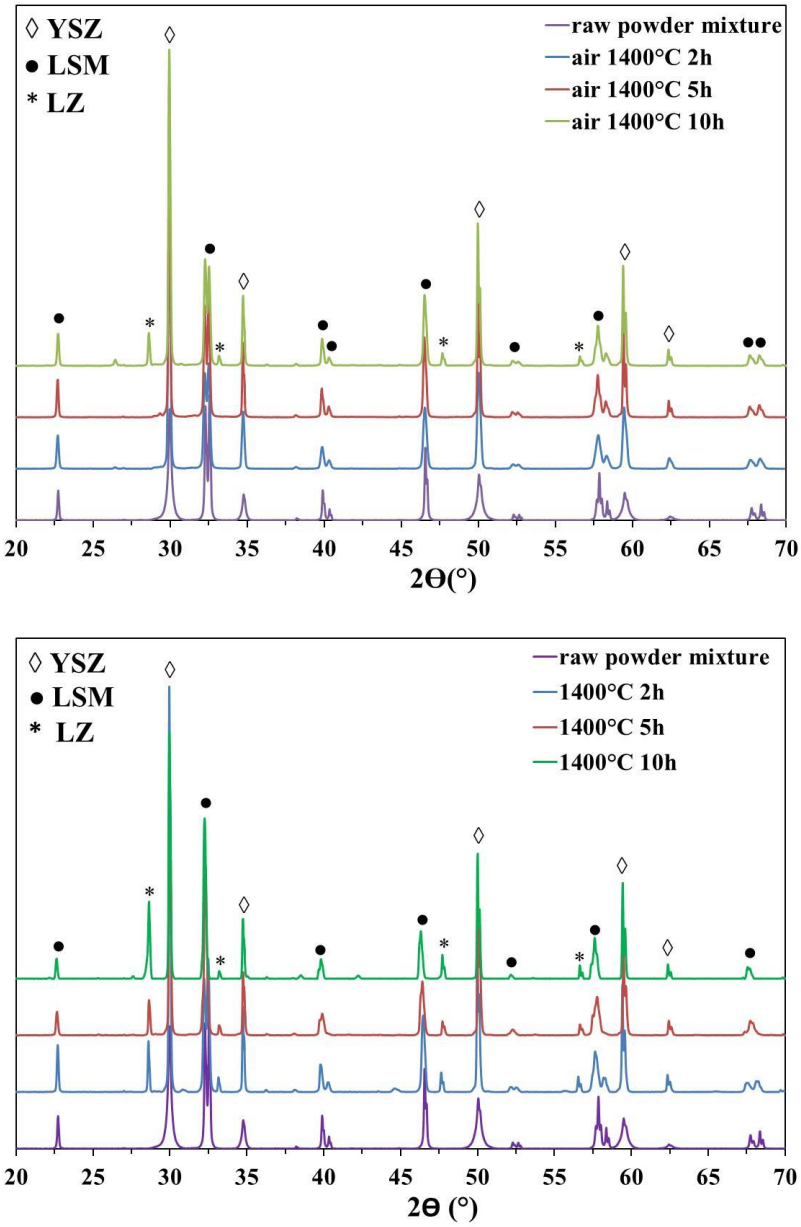

Figure 4.4 XRD patterns of the LSM-YSZ composites sintered at 1400ºC in (a) air (b) 10^{-3} atm PO_2

4.3.3 Porosity

To consider the porosity effect on the reaction between LSM and YSZ, Inframat LSM and Fuel Cell materials YSZ was used as raw materials, and 40vol% starch powder is used as pore former to prepare the porous sample. Dense samples were prepared without any pore

formers. For samples sintered in air for 2h, dense samples formed LZ, but porous sample did not. Sintered for 10h in air LZ phase was formed in both dense and porous samples. Sintered in lower PO_2, 10^{-3} and 10^{-6} atm, LZ was formed in both dense and porous samples. It suggested that in high PO_2, the reaction between LSM and YSZ is preferred in dense LSM-YSZ composite. In dense sample, the PO_2 in the bulk may be much lower than the surface, which promotes the reaction forward. Diffusion path is more available in dense samples.

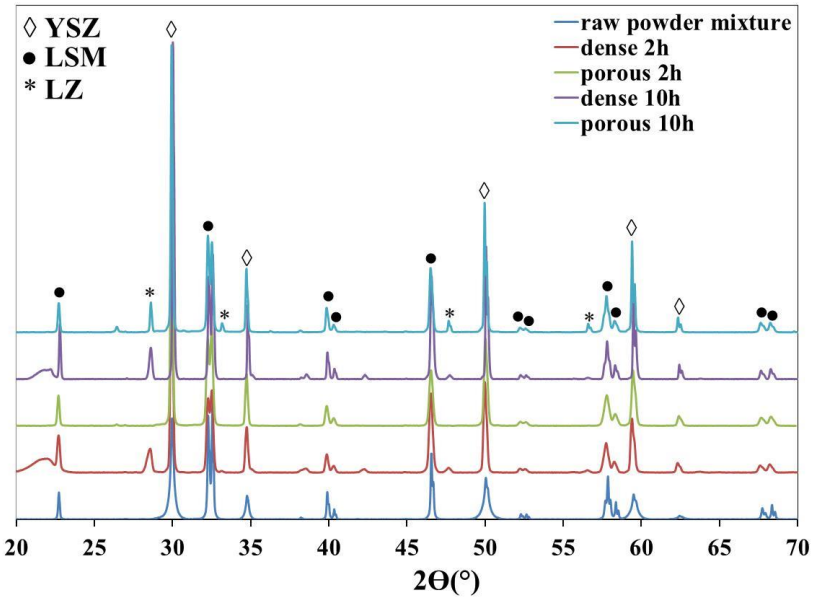

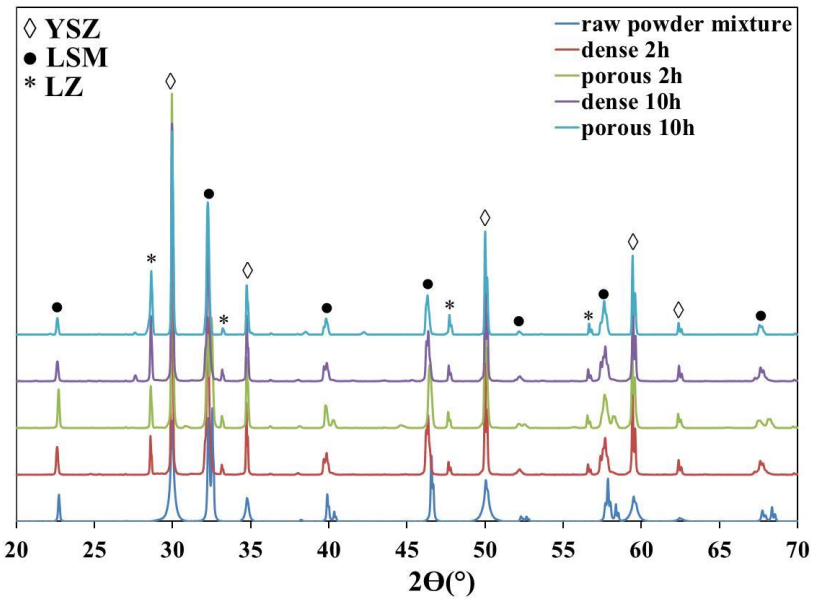

Figure 4.5 XRD patterns of the LSM-YSZ composites sintered at 1400ºC for samples with and without pore formers in (a) air (b) 10^{-3} atm O_2

4.3.4 Starting Powder

Two different LSM powders were used in this study, one is from Inframat, Connecticut and the other one is from Fuel cell materials, Ohio. They have the same formula $La_{0.8}Sr_{0.2}MnO_3$ and showed the same XRD pattern attributed to standard LSM. In Chapter 2, LSM powder and YSZ powder both from Fuel Cell Materials were used, a small amount of carbon black were used as pore former so the sample is relatively dense (density 94%). In chapter 3, LSM powder from Inframat and YSZ powder from Fuel Cell Materials were used, a large amount of starch powder were used as pore former so the sample is relatively porous (density 75-84%). Based on the discussion about the porosity in Chapter 4.3.3, we expect that the porous composite tends to have more intense reaction than the dense composite. The results however tell a different story. Sintered in air for 10h, the dense sample has no LZ formation, but the porous sample has formed LZ. Sintered in lower PO_2, a higher LZ/YSZ content (50-66%) and a lot of MnO_x phase were observed for dense sample by SEM and XRD analysis; a lower LZ/YSZ content (25-30%) and no MnO_x were detected in dense samples by XRD, and a little MnO_x was found in 1ppm sintered samples by SEM. So, we can get a conclusion that the porous sample reacts more intense than dense sample in air, but the dense sample reacts more intense than the porous sample in lower PO_2. And the XRD peak of LSM shift was observed in dense sample only, in which case the LSM crystal structure changed and the unit cell volume increased. All these behavior can be attributed to the different properties of the raw powder. The different manufacturing process may result in the different stability and reaction activity at varied conditions.

Table 4.1 The LSM-YSZ reaction product using different LSM powders sintered at 1400ºC for 10h

	Dense samples	**Porous samples**
LSM powder source	Fuel cell materials	Inframat
Sintered in air	No LZ	LZ
Sintered in 1000ppm PO_2	LSM peak shift, LZ, MnO_x	LZ
Sintered in 1ppm PO_2	LSM peak shift, LZ, MnO_x	LZ, MnO_x

4.4 Conclusion

The interaction between LSM and YSZ has been examined as a function of sintering temperature and time, sample density and starting powder. Higher temperature enhanced secondary phase formation; longer sintering time enhanced secondary phase formation. Dense sample promoted inter-diffusion process and enhanced secondary phase formation. Raw powder has the same chemical formula can show very different stability and reactivity due to different manufacturing process.

Chapter 5 Reversibility and Prevention of the Reaction between LSM-YSZ

5.1 Introduction

This chapter focused on the reversibility of the reaction between LSM and YSZ. The reaction between LSM and YSZ produces oxygen gas; thermodynamically this reaction can be reversed by reinterring the samples at higher PO_2 than the original sintering atmosphere. Selected samples initially sintered in low PO_2, were resintered at 1400°C in higher PO_2. On subsequent sintering in higher PO_2, the microstructure change of the LSM-YSZ composite show the proof of the reversibility of the interaction. The reversibility of LSM-YSZ reaction was independently confirmed by using $La_2Zr_2O_7$ and MnO_x.

5.2 Experimental Section

Selected pellets initially sintered at 1400°C in 1000 ppm O_2 or 1 ppm O_2 atmospheres, were resintered at 1400°C again in dry air or pure oxygen. Certified flowing gas (Airgas, Connecticut) at fixed flow rate of 40 sccm was used and in all the sintering experiments. The samples were sintered and resintered for equal time to check the reversibility of the reaction.

Phase characterization was performed by XRD analysis using Cu Kα radiation (Bruker D8 advance X-Ray diffractometer). The polished cross section was prepared using standard metallographic techniques and analyzed using SEM and the attached EDS (Quanta 600 FEI Company, Hillsboro, OR). The TEM specimens were prepared using a FIB instrument (FEI strata 400S, FEI company, Hillsboro, OR, 30 keV Ga+ ions). TEM high resolution images and EDS spot analysis were performed using JEOL 2010 FasTEM.

To check the reversibility of the LSM-YSZ reaction with respect to oxygen partial pressure, $La_2Zr_2O_7$ compound was first prepared. The YSZ and La_2O_3 powders were mixed and

calcined at 1300°C for 24 h. The calcined powder was crushed into fine powders and pressed into pellets. The pellets were sintered at 1500°C for 24 h. Then the prepared $La_2Zr_2O_7$ samples were crushed into powders and mixed with MnO_2 powder (1:2 mole ratio). The mixed powder was pressed into pellets and sintered at 1400°C for 10 h in air. Phase characterization was performed by XRD analysis using Cu Kα radiation (Bruker D8 advance X-Ray diffractometer).

5.3 Results

5.3.1 XRD

For the samples initially sintered in reduced atmospheres and re-sintered in oxygen or air, these reaction products tend to revert back to the original starting material composition of LSM and YSZ. As shown in Figure 5.1, LZ peak show up in sample sintered in 10^{-3} atm PO_2, but not shown in sample resintered in O_2.

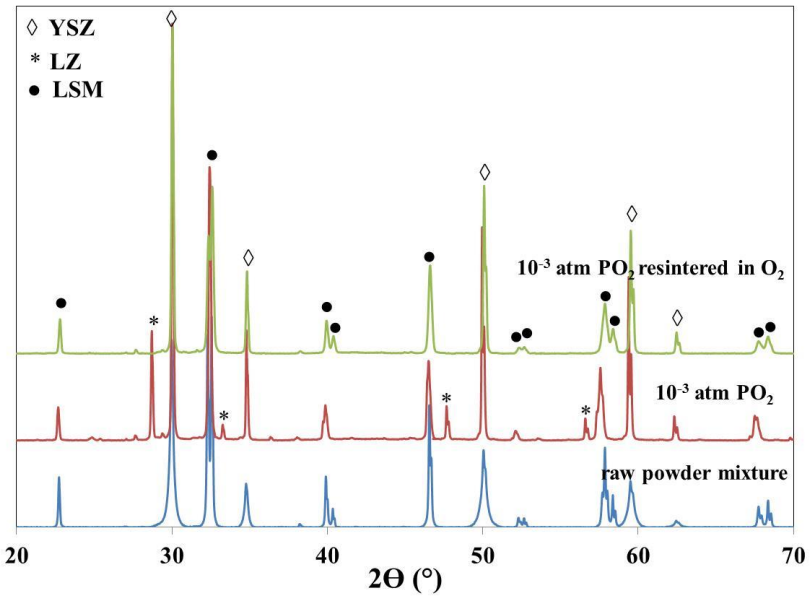

Figure 5.1 XRD patterns of LSM-YSZ composites sintered in 10^{-3} atm PO_2 followed by O_2

5.3.2 SEM

For the sample initially sintered in 10^{-3} and 10^{-6} atm PO_2 followed by sintering in air, significant morphological changes are observed. The dark phase is YSZ (marked as 1 in Figure

5.2) and the bright phase is LSM (marked as 2 Figure 5.2). The grain size of the LSM and YSZ phases vary from 1-8 μm. Overall, the YSZ grains are larger than LSM. The EDS analyses show the presence of ~ 7 at% La and ~ 4 at% Zr in some of the LSM grains. The EDS analyses also show that ~ 10 at% Mn in the YSZ phase for sample (a) and ~ 12 at% Mn in the YSZ for sample (b). On subsequent resintering of these samples in air, the $La_2Zr_2O_7$ and Mn_3O_4 compounds disappear which is consistent with the XRD results. The results indicate that the reaction between the LSM and YSZ is reversible.

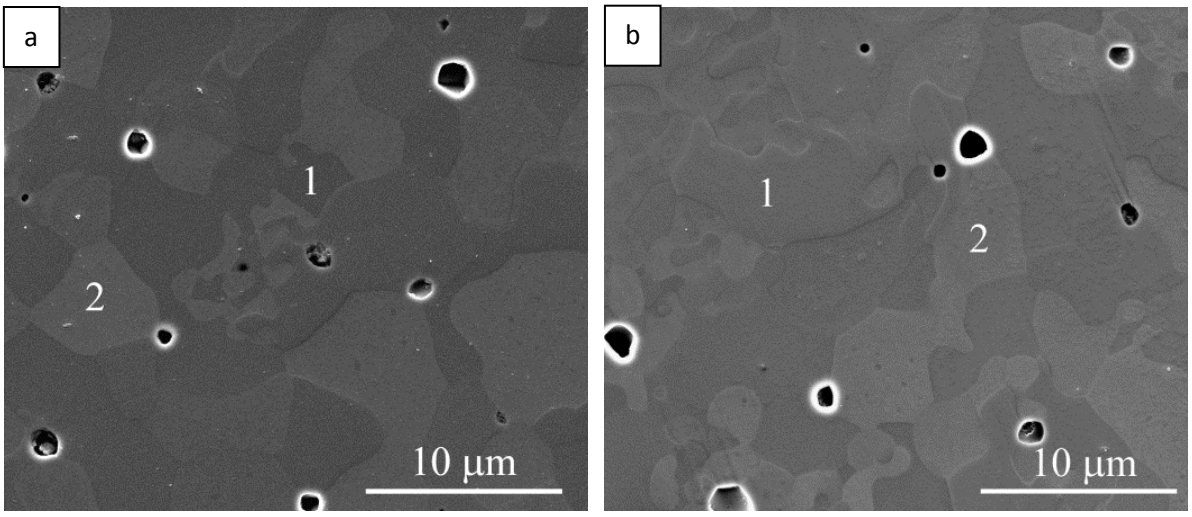

Figure 5.2 SEM of LSM-YSZ composite sintered in (a) 1000 ppm O_2 followed by air and (b) 1ppm O_2 followed by air

5.3.3 TEM-EDS

Figure 5.3 shows the TEM image and EDS analysis. For the sample initially sintered in 10^{-6} atm PO_2 and resintered in air, three different phases are observed. The phases are identified as $La_2Zr_2O_7$ (marked as 1,2), YSZ (marked as 3,4) and LSM (marked as 5,6) by EDS. The grain sizes of these phases are 1-5 μm. Twins are observed in the LSM grains. The compositions of the LSM and YSZ vary from grain to grain. 2-6 at% La and 4-8 at% Mn are found in the YSZ. No secondary phase has been found at the LSM and YSZ grain boundaries, consistent with the elemental concentration profiles at grain boundary.

The absence of MnO_x phase in the sample initially sintered in 10^{-6} atm PO_2 and resintered in air indicates that the reaction between LSM and YSZ is reversible, consistent with the XRD and SEM analysis. However, presence of the $La_2Zr_2O_7$ grains in the sample initially sintered in 10^{-6} atm PO_2 and resintered in air suggests that the complete reversibility of the reaction has not been attained within the experimental conditions.

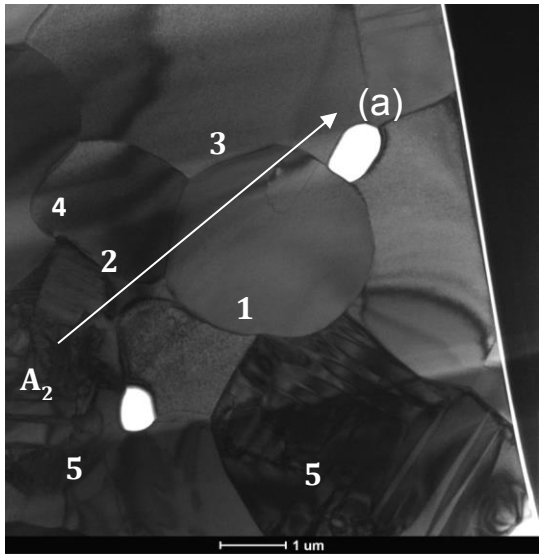

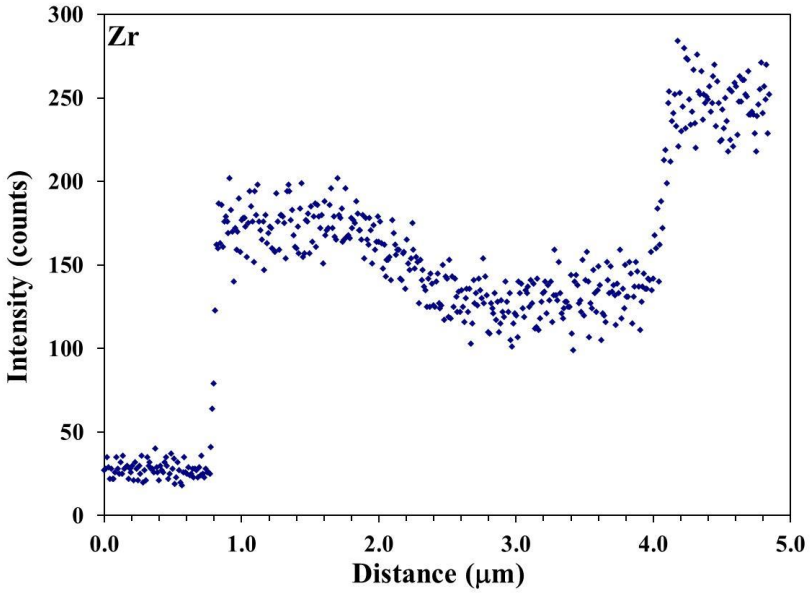

(b) The concentration profiles of Zr

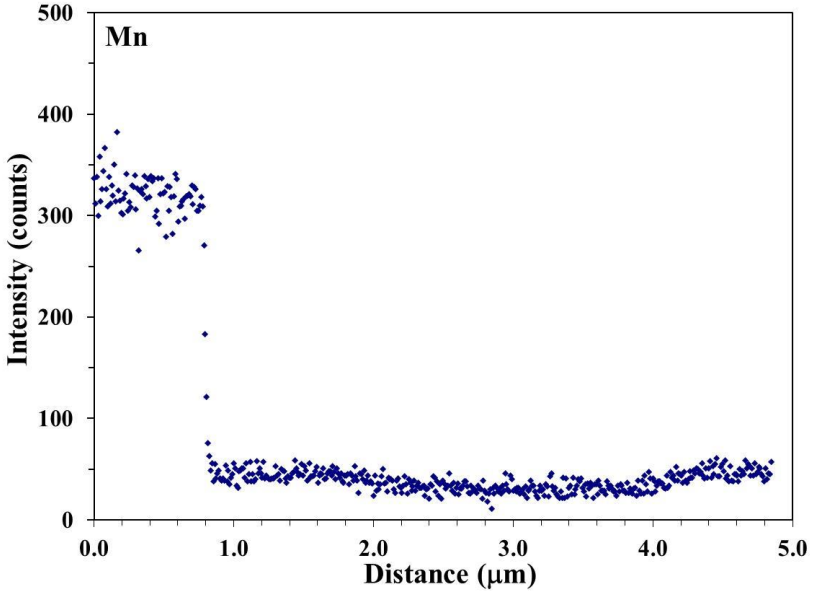

(c) The concentration profiles of Mn

Figure 5.3 (a) TEM image of the LSM-YSZ composite sintered in 1 ppm PO_2 followed by air at 1400°C for 10 h, and the concentration profiles of (b) Zr and (c) Mn determined along the line A1-A2 in the TEM image.

5.4 The Reaction between LZ and MnO_2

From the XRD pattern of the sintered samples in Figure 5.4, formation of the $La_2Zr_2O_7$ (JCPDS number 10705602) phase is confirmed.$Y_2Zr_2O_7$ (JCPDS number 10749311) and small amount of unreacted La_2O_3 phases were also observed.

The XRD pattern in Figure 5.4 shows rhombohedral $LaMnO_3$ (JCPDS number 01-070-3942), cubic YSZ (JCPDS number 01-077-2112), and small amount of $La_2Zr_2O_7$ and Mn_3O_4 phases. Large reduction in the amount of $La_2Zr_2O_7$ suggests that the $La_2Zr_2O_7$ phase reacts with MnO_2 and forms $LaMnO_3$ and YSZ. The absence of the $Y_2Zr_2O_7$ phase indicates that it also reacts with MnO_2 to form $LaMnO_3$ and YSZ. These observations confirm that the reaction between a) LSM and YSZ results in $La_2Zr_2O_7$ and MnO_x and b) the $La_2Zr_2O_7$ and MnO_x results

in $LaMnO_3$ and ZrO_2 formation. Unreacted MnO_2 transforms into the more stable Mn_3O_4 phase during sintering.

$$2ZrO_2 + La_2O_3 = La_2Zr_2O_7 \quad (5.1)$$

$$La_2Zr_2O_7 + 2MnO_2 = 2ZrO_2 + 2LaMnO_3 + 1/2\,O_2 \quad (5.2)$$

$$3MnO_2 = Mn_3O_4 + O_2 \quad (5.3)$$

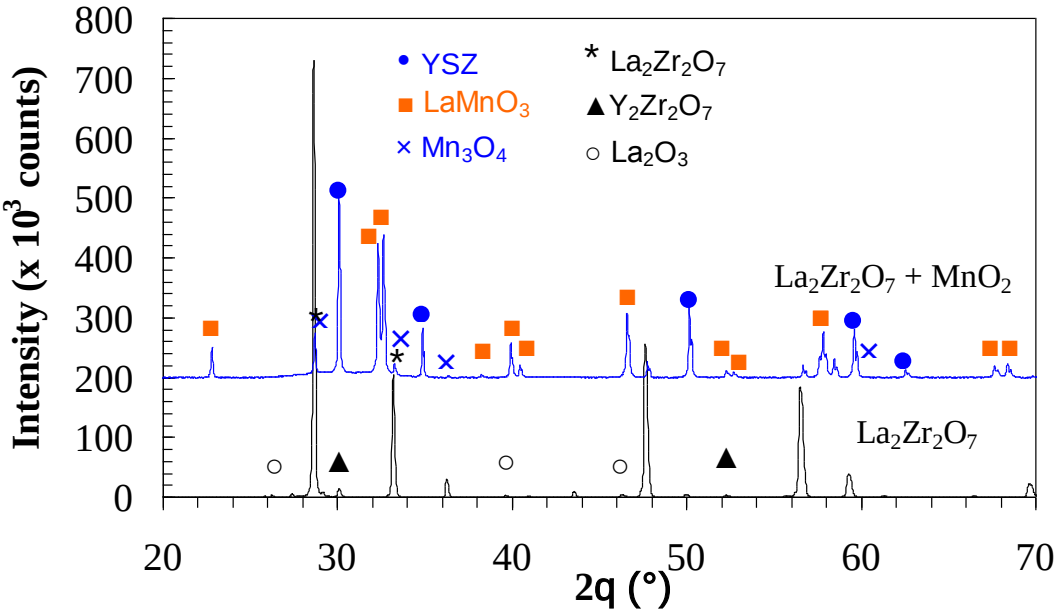

Figure 5.4 XRD patterns of the sintered $La_2Zr_2O_7$ and the mixture of $La_2Zr_2O_7$ with MnO_2 powder after sintering at 1400°C for 10 h in air.

5.5 Discussion

For the samples sintered in 10^{-3} atm and 10^{-6} atm PO_2 followed by sintering in air, the quantity of $La_2Zr_2O_7$ is found to be significantly smaller compared to those sintered in 10^{-3} and 10^{-6} atm PO_2. This observation is also supported by the absence of $La_2Zr_2O_7$ phase in the XRD analysis. This indicates that the reaction products formed during sintering at lower oxygen pressures have the tendency to revert back to initial products according to the reaction:

$$\frac{1}{2}La_2Zr_2O_7 + \frac{1}{3}Mn_3O_4 + \frac{4}{3}O_2 = LaMnO_3 + ZrO_2 \quad (5.4)$$

The presence and co-stability of various phases in the reactions 5.2 and 5.4 has been validated experimentally. $La_2Zr_2O_7$ compound was first prepared to check the reversibility of the LSM-YSZ reaction with respect to oxygen partial pressure. The YSZ and La_2O_3 powders were mixed and calcined at 1300°C for 24 h. The calcined powder was crushed into fine powders and pressed into pellets. The pellets were sintered at 1500°C for 24 h. From the XRD pattern of the sintered samples in Figure 5.4, formation of the $La_2Zr_2O_7$ (JCPDS number 01-070-5602) phase is confirmed.$Y_2Zr_2O_7$ (JCPDS number 01-074-9311) and trace amount of unreacted La_2O_3 (JCPDS number 01-071-5408) phases were also observed.

5.6 Retarding the $La_2Zr_2O_7$ Formation at the $LaMnO_3$-YSZ Phase Interface

In the previous chapter, we have discussed the influences of different factors on the LZ formation. By combining these factors, it is possible to reach a condition that the LSM-YSZ phase interface is actually stable, at least as long as diffusion is not considered. Unfortunately the Mn diffusion from LSM into YSZ will change this unfavorably. With the proceeding of the Mn diffusion, the driving force of the LZ formation at the LSM-YSZ interface increases, leading to LZ formation in a long time run.

$$LZ\ formation\ driving\ force = [\mu(LSM, La) + \mu(YSZ, Zr)] - [\mu(LZ, La) + \mu(LZ, Zr)] \quad (5.5)$$

Since Mn diffusion is the initial and critical step of the LSM-YSZ reaction, by retarding the Mn diffusion, it is possible to decelerate the increase in the driving force of the LZ formation and to stabilize the LSM-YSZ phase interface for an enough long period. Thermodynamically, the Mn diffusion can be retarded by decreasing its driving force

$$Mn\ Diffusion\ Driving\ Force = \mu(LSM, Mn) - \mu(YSZ, Mn) \quad (5.6)$$

As Equation (5.5) shows, the driving force of the Mn diffusion from LSM into YSZ can be decreased by decreasing the chemical potential of Mn in LSM, μ (LSM, Mn) or increasing that in YSZ, μ (YSZ, Mn). It is not worthwhile to decrease μ (LSM, Mn), as very often a decrease in μ (LSM, Mn) means an increase in μ (LSM, La) and therefore also an increase in the driving force of the LZ formation. An increase in μ (YSZ, Mn) has no essential influence on the driving force of the LZ formation and this can be easily achieved by doping Mn oxide into YSZ. Mn oxide can also be introduced into LSM. The Mn oxide then serves as a Mn reservoir for the neighboring LSM phase. As long as LSM is in equilibrium with the Mn oxide, the Mn diffusion from LSM into YSZ will not change the driving force of the LZ formation. The Mn diffusion can also be retarded by adjusting the Mn diffusion rates in LSM and in YSZ. This is however very difficult and obviously less feasible. To totally stop the Mn diffusion, a thin layer of conducting diffusion barrier has to be put between LSM and YSZ. The above discussions outline the measures to retard the LZ formation at the LSM-YSZ interface. For real SOFC applications, the electrical properties, the chemical and mechanical compatibilities of LSM and YSZ also have to be considered.[28]

5.7 Experiment

10mol% Mn doped YSZ powder was synthesized first. Then the Mn-YSZ powder and LSM powder were mixed uniformly and sintered in air for 10h. YSZ-LSM pellet sintered in air for 10h was used as reference. XRD, SEM, EDS etc. were used to characterize the secondary phase formation and microstructure change. Manganese doped YSZ powder were prepared by conventional wet chemical and ceramic processing route. YSZ powder (TZ-8YS, Tosoh Corporation, Yamaguchi, Japan) was mixed with desired amount of $Mn(NO_3)_2$ and ethylene glycol solution ($Mn(NO_3)_2$: ethylene glycol = 1:4) (Alfa Aesar, Massachusetts, USA). The

solution was stirred for 24h at 75 °C followed by binder removal at 400 °C with 2 h dwell time and calcination at 1000 °C for 10 h in air. The calcined powder was grounded for 2 h and pressed to pellets. The pellets were sintered at 1400 °C for 10 h in air. The calcination and sintering time and temperature were optimized to ensure the formation of single phase and microstructural homogeneity using, respectively, X-ray diffraction (XRD, Bruker D8 Advance diffractometer, Bruker AXS Inc., Madison, WI) with 0.0020°/s scan rate and energy dispersive spectroscopy (EDS) attached to scanning electron microscopy (SEM, FEI Company, Hillsboro, OR) techniques. EDS elemental analysis suggested average concentration of manganese in the sample is 9.5 ± 0.7 at.%, in good agreement with the added manganese (10at.%) in the batch composition. Considering the detection limits of XRD and EDS techniques, the samples were also rinsed with hydrochloric acid for the removal of manganese oxide, if present. The samples were cleaned with deionized water and ethyl alcohol prior to electrical conductivity measurement.

5.8 Result and Discussion

The XRD patterns of the as-received YSZ powder, sintered YSZ and sintered Mn-YSZ are shown in Figure 5.5. While the as-received YSZ powder shows cubic symmetry, two distinct features are observed for the other samples: shifting in Bragg's diffraction plane positions towards higher 2θ indicating a decrease in lattice volume and appearance of shoulders in the XRD patterns corresponding to the diffraction planes indicating lower crystal symmetry. Indeed, tetragonal as well as cubic symmetry is found in the sintered YSZ and the Mn-YSZ samples. Distortion of the oxygen sub-lattice results in the tetragonal symmetry in the sintered YSZ.[174,175,176] Local distortion of oxygen sub-lattice and the presence of 6-fold Mn^{3+} and $Mn^{2.66+}$ ions result in tetragonal symmetry in the sintered Mn-YSZ sample.[177]

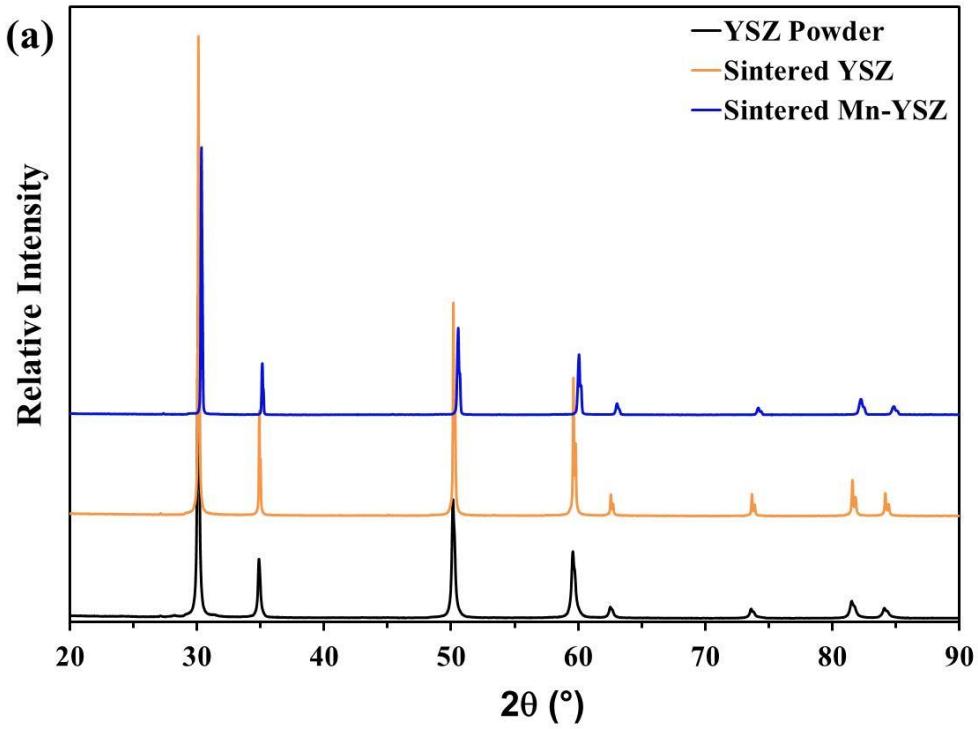
(a)
YSZ Powder
Sintered YSZ
Sintered Mn-YSZ
Relative Intensity
20
30
40
50
60
70
80
90
2θ (°)

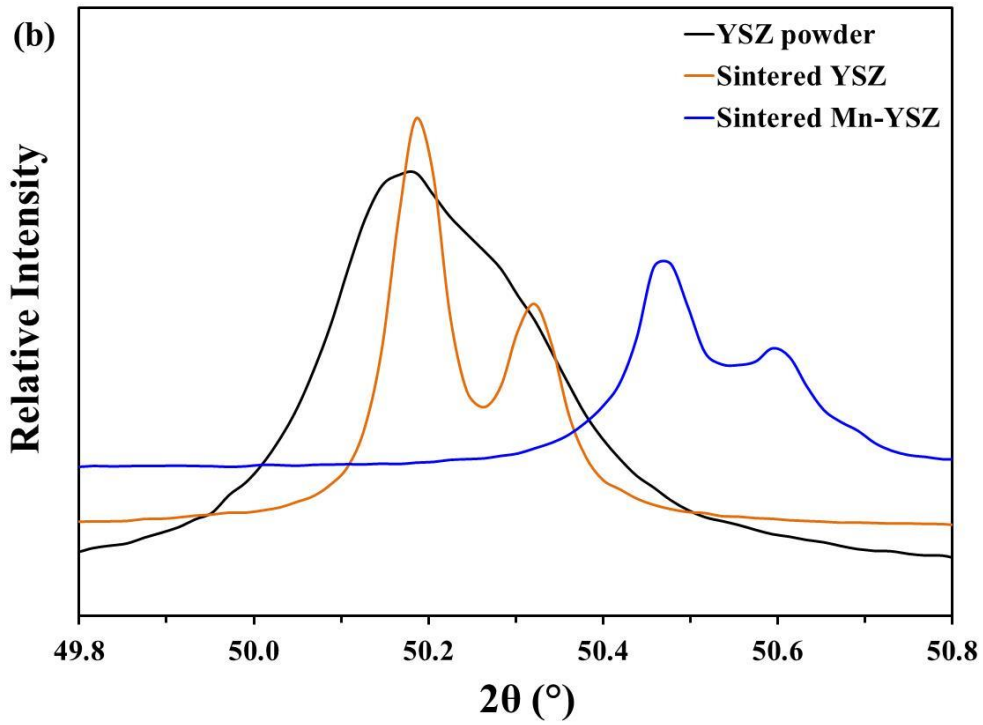
(b)
YSZ powder
Sintered YSZ
Sintered Mn-YSZ
Relative Intensity
49.8
50.0
50.2
50.4
50.6
50.8
2θ (°)

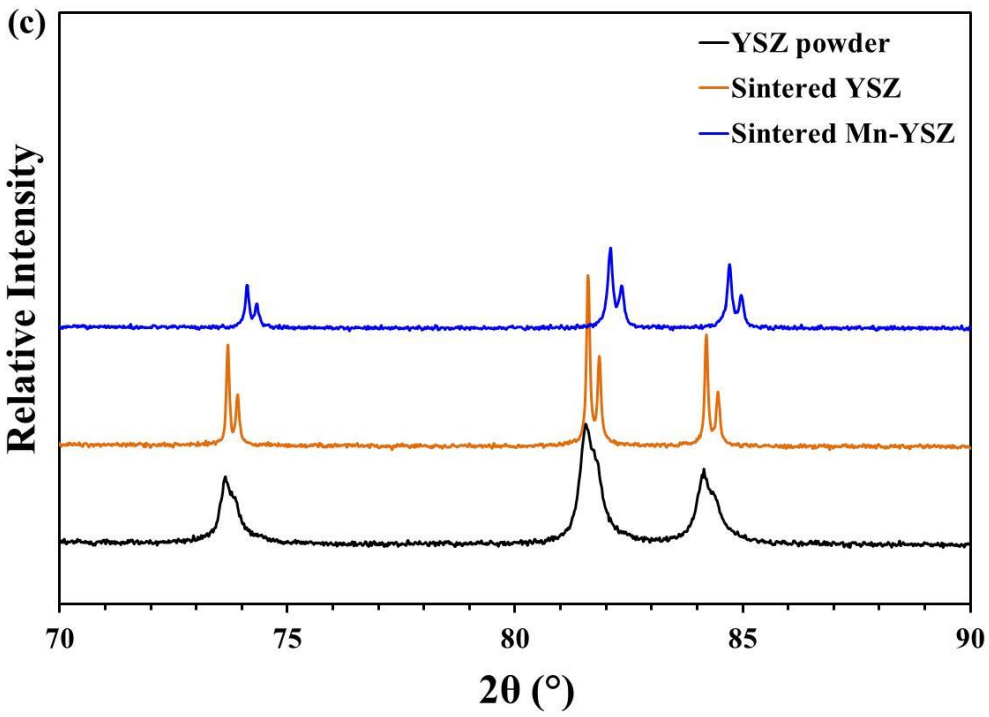

Figure 5.5 XRD patterns of the YSZ and Mn-YSZ samples at low and high angles are shown to illustrate the shift in Bragg's diffraction planes' position.

The lattice parameters and unit cell volumes of the YSZ and Mn-YSZ samples have been calculated using 'Unit Cell' program and listed in Table 5.1. The decrease in lattice volume for the Mn-YSZ samples suggests that manganese forms substitutional solid solution with YSZ. In sintered Mn-YSZ, the valance states of manganese ions are 2.66 and 3. Manganese substitution in the cationic sites in YSZ generates oxygen vacancies to maintain charge neutrality.

After sintering at 1400C for 10h in air, the Mn-YSZ did not show any secondary phase formation with LSM (Figure 5.6), but YSZ powder react with LSM and formed LZ. The SEM images were shown in Figure 5.7. There were only two kinds of grains shown on the surface, LSM and YSZ (confirmed by EDS). On the cross section, there was no LZ phase shown up, but some MnO_x phase shown at the grain boundary. The exist of MnOx phase means Mn diffusion still happened during the sintering process, the diffusion may be alleviated to a certain extent that

the LSM structure did not lose its stability and the further diffusion and reaction between ZrO_2 and La_2O_3 did not happen.

Table 5.1 Lattice constants for the cubic and tetragonal phases in the YSZ and Mn-YSZ samples.

Sample/unit cell structure	Cubic (a-axis, Å)	Tetragonal	
		a-axis (Å)	c-axis (Å)
YSZ powder	5.1426		
Sintered YSZ	5.1394	3.6234	5.1407
Sintered Mn-YSZ	5.1166	3.6086	5.1156

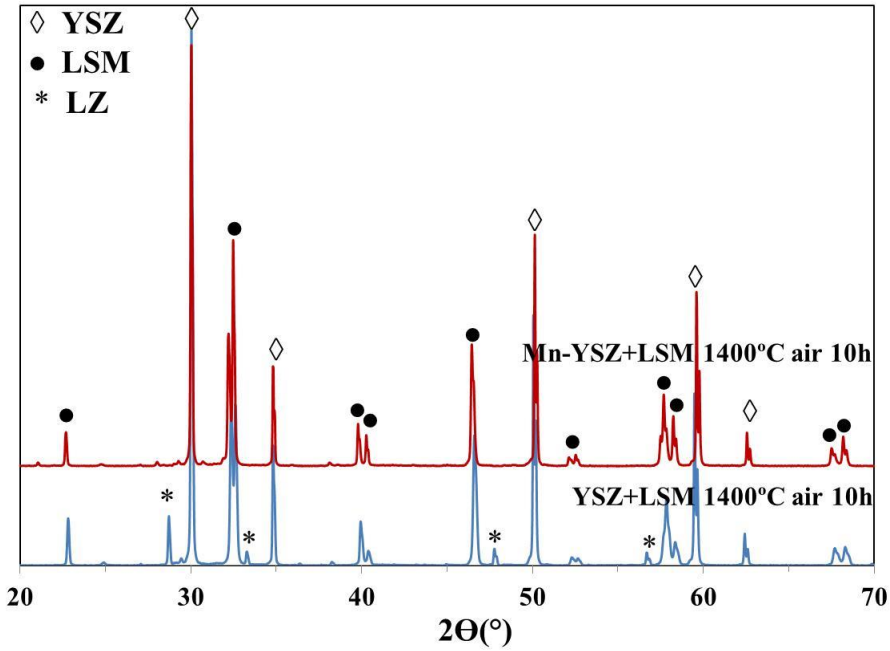

Fig 5.6 XRD patterns of the mixture of Mn-YSZ and LSM after sintering at 1400°C for 10 h in air, the mixture of YSZ and LSM as reference

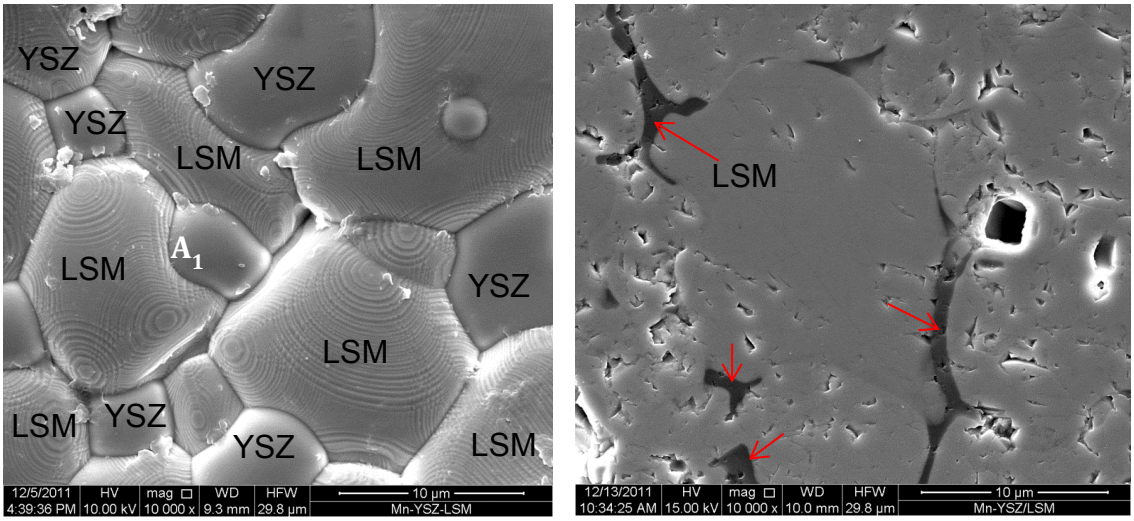

Figure 5.7 SEM of Mn-YSZ/LSM sample sintered at 1400°C for 10h in air

(a) surface (b) cross section

5.9 Conclusion

The reaction between LSM and YSZ in lower PO_2 tends to be reversed back when resintered in air. The reversibility of the LSM-YSZ reaction was proved directly by the reaction of $La_2Zr_2O_7$ and MnO_2 in air. The LZ formation can be prevented by doping Mn into YSZ to slow down the Mn diffusion from LSM to YSZ.

Chapter 6 Improvement of the Durability of SOEC by Mn-doped YSZ

6.1 Introduction

In this chapter, we report an approach for preventing the delamination and increasing longevity of the SOEC device with configuration air/LSM//YSZ//LSM/air. The symmetrical cell configuration simplifies the cell assembly and eliminates sealing requirements as both electrodes of the cell are exposed only to air. The cells were electrochemically tested at fixed operating voltages to measure the overall electrochemical degradation. Mn-doped YSZ layer was prepared between LSM and YSZ to suppress interfacial degradation and anode delamination in SOEC. A mechanism for the cell longevity and anode delamination has been developed based on cell testing results and observations on the chemical and morphological changes at the anode-electrolyte interfaces.

6.2 Experimental Section

6.2.1 Cell Fabrication

Electrolyte supported cell was used in this study, 190 μm thick $(ZrO_2)_{0.92}(Y_2O_3)_{0.08}$ as electrolyte (Fuel Cell Materials), and 25 μm thick $(La_{0.8}Sr_{0.2})_{0.98}MnO_{3-x}$ (Fuel Cell Materials) as anode and cathode. Two methods were used to prepare the Mn-YSZ layer, solid state diffusion and sol-gel coating. During the solid state diffusion experiment, the YSZ substrates were completely surrounded by Mn_2O_3 powder. Then the Mn was allowed to diffuse at 1250°C for 2h. After the diffusion experiment, HCl acid was used to dissolve the extra manganese oxide particle on the surface. In the sol-gel experiment, the metal alkoxide $Zr(OPr)_4$ was used as precursor, yttria and manganese were introduced by nitrates $Y(NO_3)_3 \cdot 6H_2O$ and $Mn(NO_3)_2.6H_2O$, acetylacetone was used as a chelating agent, with the aid of catalyst HNO_3, the precursor was

hydrolyzed and aged to a certain viscosity. [178, 179, 180] Then the Mn-YSZ sol was spin coated on the YSZ substrate. After drying in ambient atmosphere, the coated samples were further dried in an oven at 60°C for 1h then followed by heating at 250°C for 30min. The above process of spin coating, drying, and heating at 250°C was repeated several times to increase the coating thickness. The coating was finally heat treated in furnace at 1250°C for 2h.

The electrode LSM was screen printed on both sides of the specimen and sintered at 1200°C for 2h. The electrochemical active area of the cell electrode was calculated to be 0.8 cm^2. Then silver screen and silver wire were attached to each electrode using silver-palladium contact paste as current collector and sintered at 850°C for 1h. Figure 6.1 shows the schematic of the cell configuration. U-cell is the undoped symmetric cell, YSZ as electrolyte, LSM as cathode and anode. D-cell is the Mn-doped cell prepared by solid state diffusion method, a gradient Mn-doped YSZ layer was introduced both sides of YSZ. SG-cell is the Mn-doped cell prepared by sol-gel method, a uniform porous Mn-doped YSZ layer was introduced between anode LSM and YSZ.

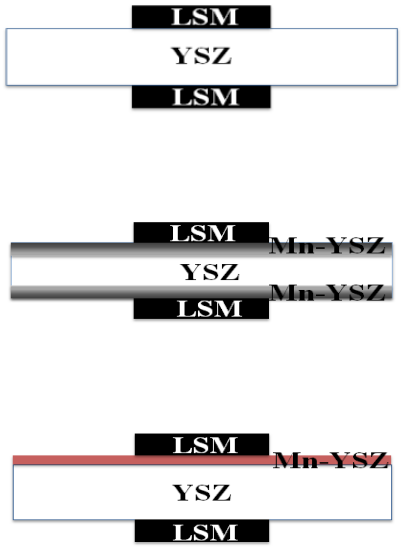

Figure 6.1 schematic of the cells configuration (a) U-cell (b) D-cell (c) SG-cell

6.2.2 Cell Testing

Figure 6.2 shows the GE test station and the alumina test rig for cell testing in our lab. The prepared button cell was put on the top of the alumina tube, and then the alumina test rig was put inside of the vertical split furnace, the cell was connect to a potentiostat through silver wire. The cell was tested at 840°C in air (2% water vapor) with flow rate 300 sccm. A type K thermocouple was placed close to the cell to monitor the operating temperature. A schematic of the experimental test set up is shown in Figure 6.3. A constant voltage 0.8V was applied up to 500h using the potentiostat (VMP2, Bio-Logic) in SOEC mode. Current and Impedance measurement was performed at fixed intervals through the duration of the test. Experiments were repeated several times at each condition to ensure reproducibility. Testing voltage 0.8V above OCV was chosen to assess the degradation under simulated accelerated cell operating conditions. 300 sccm flow rate was adopted according to ref. [120] to minimize mas transport limitation for the 10mm button cell.

6.2.3 Post-test Analysis

After completion of the electrochemical tests, cells were visually examined for electrode integrity and attachment with the electrolyte. A simple peeling off test was used to evaluate the delamination. The electrode-electrolyte interfaces were examined for morphological changes and reaction products formation after dissolving the electrode in hydrochloric acid in order to remove residual LSM from the electrolyte surface. An FEI Quanta 250 FEG scanning electron microscope (SEM) and the attached energy-dispersive X-ray spectroscopy (EDS) was used for the morphological and elemental distribution study. A Bruker AXS D-8 Advance X-ray diffractometer (XRD) was used for the identification of interfacial compound formation in the tested cells.

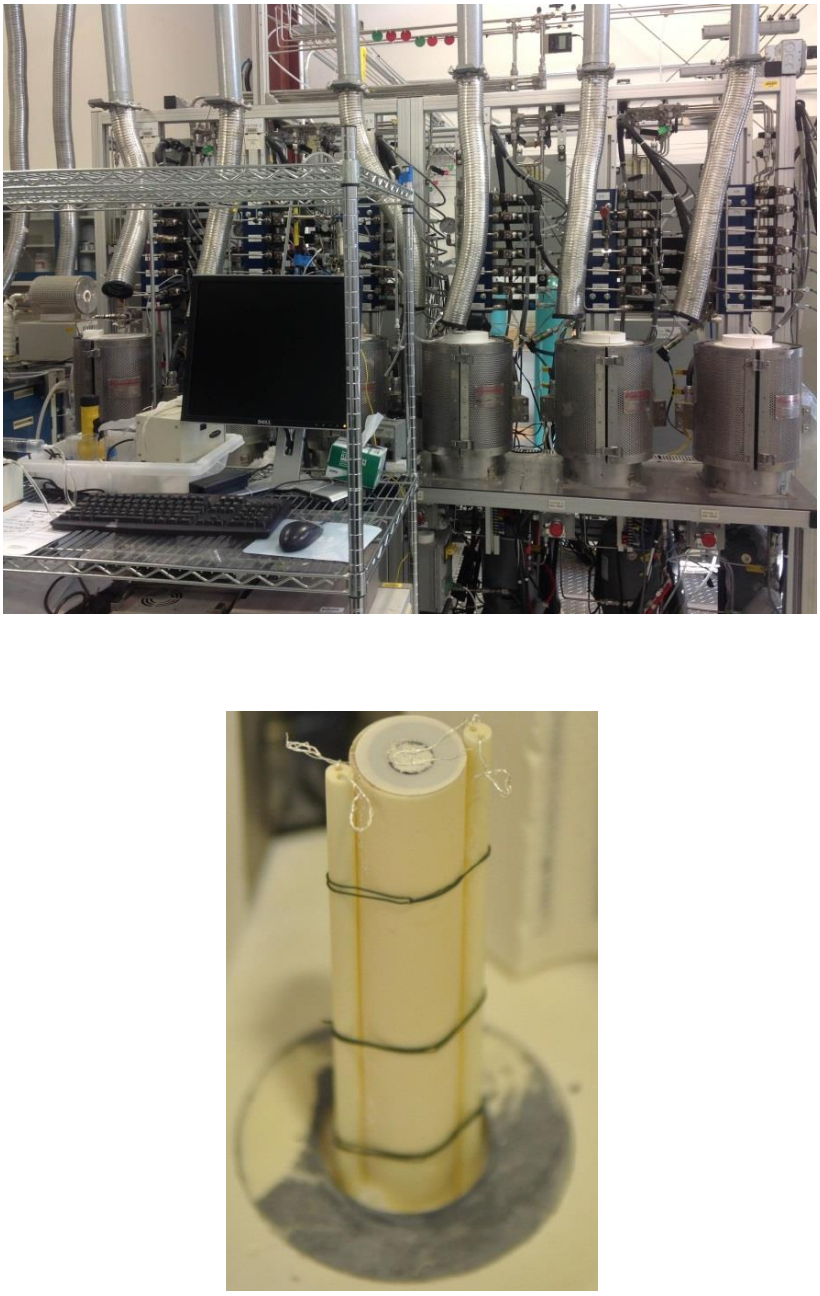

Figure 6.2 GE test station and alumina test rig

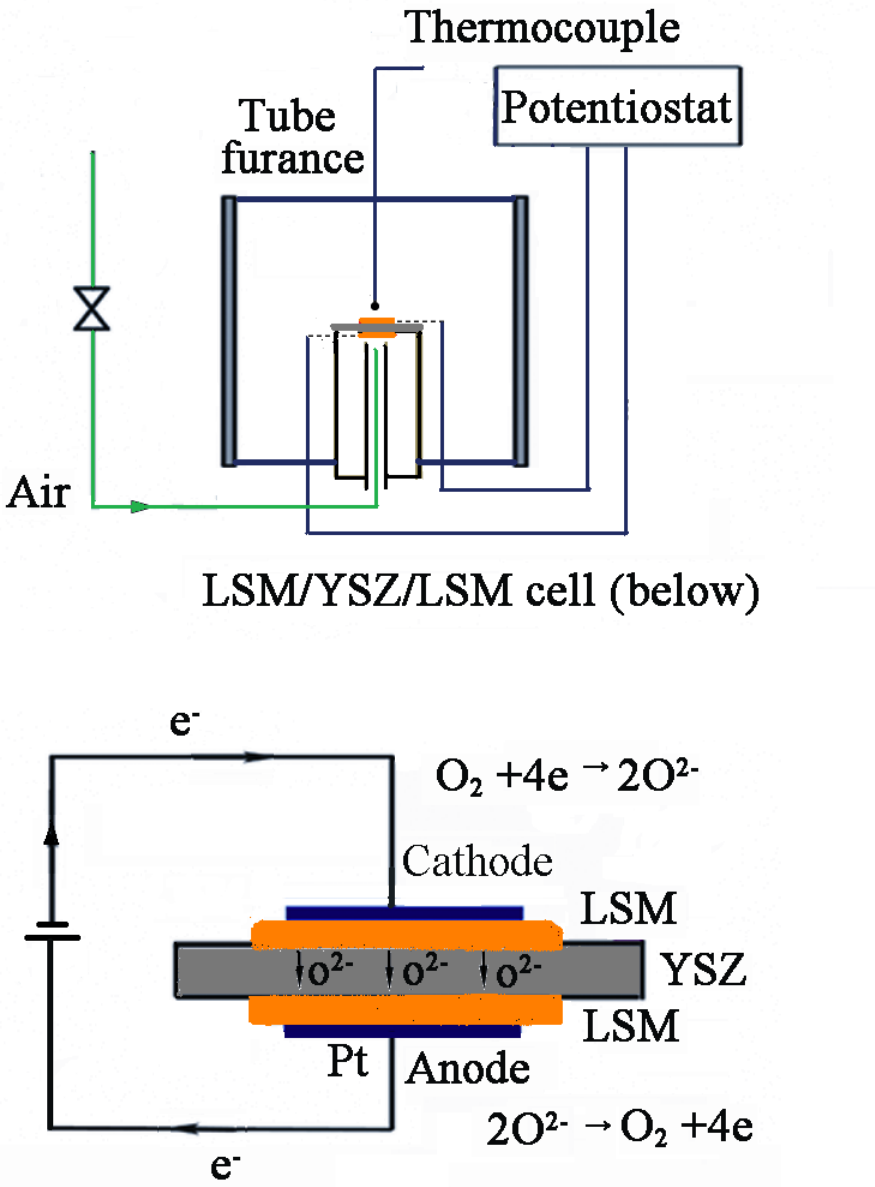

Figure 6.3 Schematic of the experimental test set up

6.3 Results

6.3.1 Electrochemical Testing

Figure 6.4 shows plots of current density during tests with different cells. For the undoped YSZ cell, the current density typically reaches a maximum of approximately 1.48

A/cm^2 after an initial improvement followed by a steep drop. The Mn-doped cells exhibit lower peak current but much more stable performance.

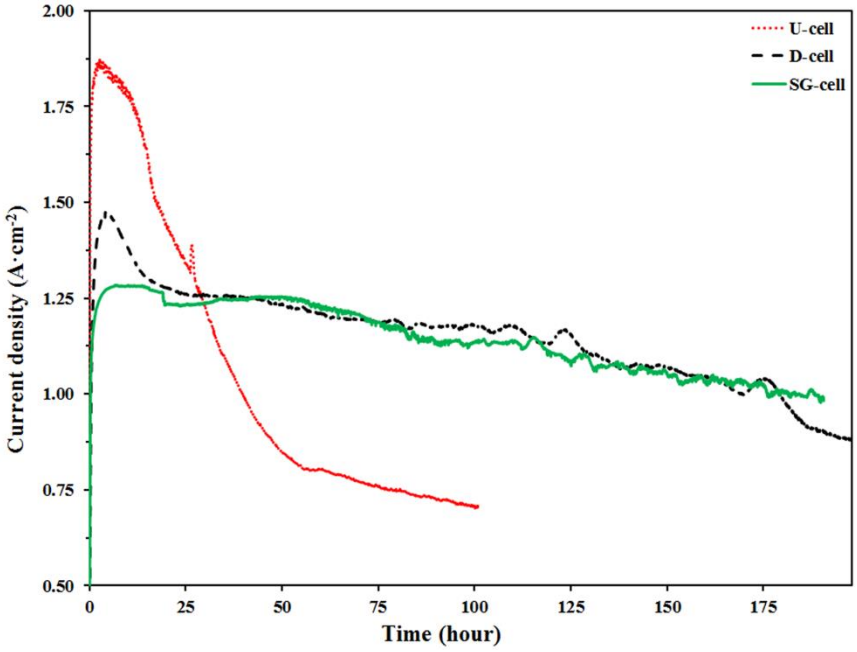

Figure 6.4 Changes in current density with time for U, D and SG-cells

Figure 6.5 shows a typical impedance spectra exhibited by the symmetrical cell assembly at 0.8 V. The skewed semicircle in the impedance plane represents the contributions from electrolyte (ohmic) resistance, oxygen surface exchange and migration, as well as gas-phase oxygen transport. The high-frequency intercept represents ohmic resistance, while the semicircle diameter represents the sum of non-ohmic contributions.[120,181,182] Figure 6.6 (a) represents the ohmic resistance trend for different cells. All the cells show an initial decrease in ohmic resistance with subsequent increase after 4h; the undoped cell shows rapid increase, the Mn-doped cells show slower increase. The doped cells show higher starting resistance than the undoped cell, however, they show much lower resistance at the end of tests. Figure 6.6 (b) represents the non-ohmic resistance trend for different cells. The cells show an initial sharp decrease after 4h, and then they behave differently for the activation and degradation period. The

activation periods are 4, 50, and 100 hours for undoped YSZ cell, Mn-YSZ diffusion cell and Mn-YSZ sol-gel cell, respectively, as these are the times at which the non-ohmic resistances reach their minimum values. The end of the activation period can be interpreted as the time when the rate of degradation equals the rate of activation. The Mn-YSZ sol-gel cell extends the activation period means the activation is slowest. But the subsequent slow degradation result in the more stable performance. The initial decrease in both ohmic and non-ohmic resistances is explained by electrode conditioning process related with a re-equilibrium process of surface strontium or extension of TPB by manganese doping of the electrolyte. [183,184,185]

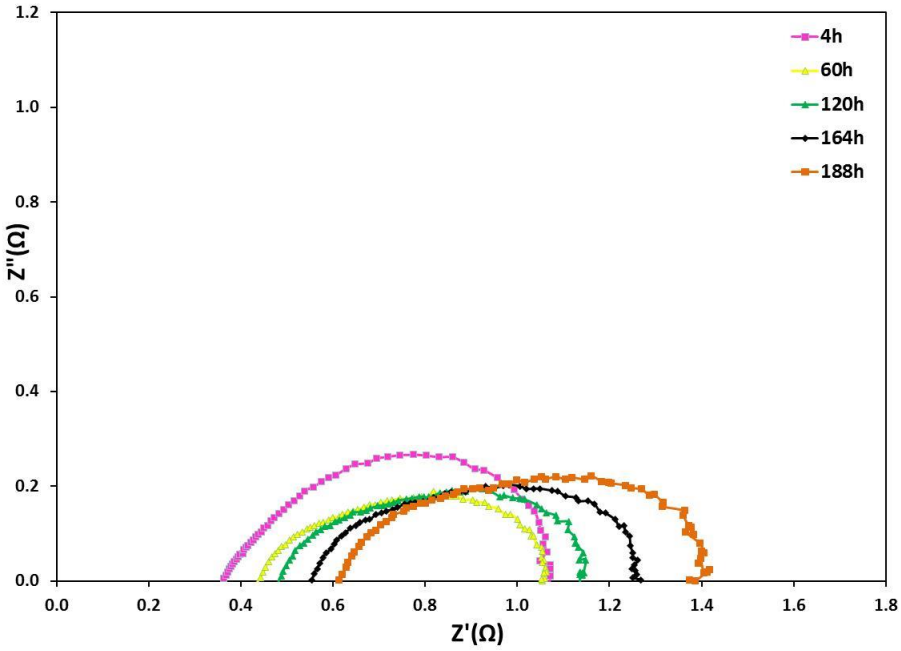

(a)

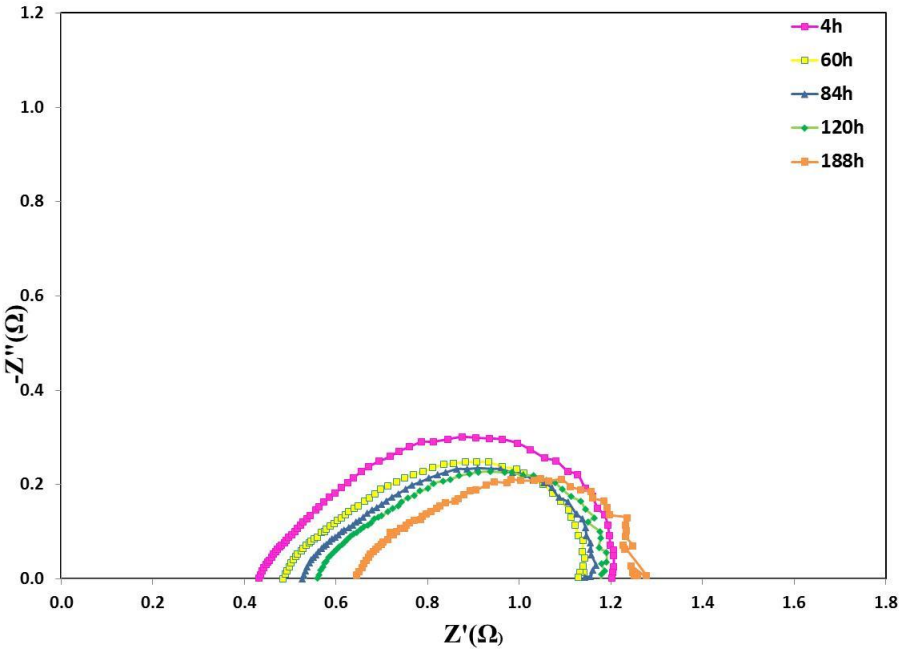

(b)

Figure 6.5 Nyquist plots of impedance spectra (a) D-cell (b) SG-cell

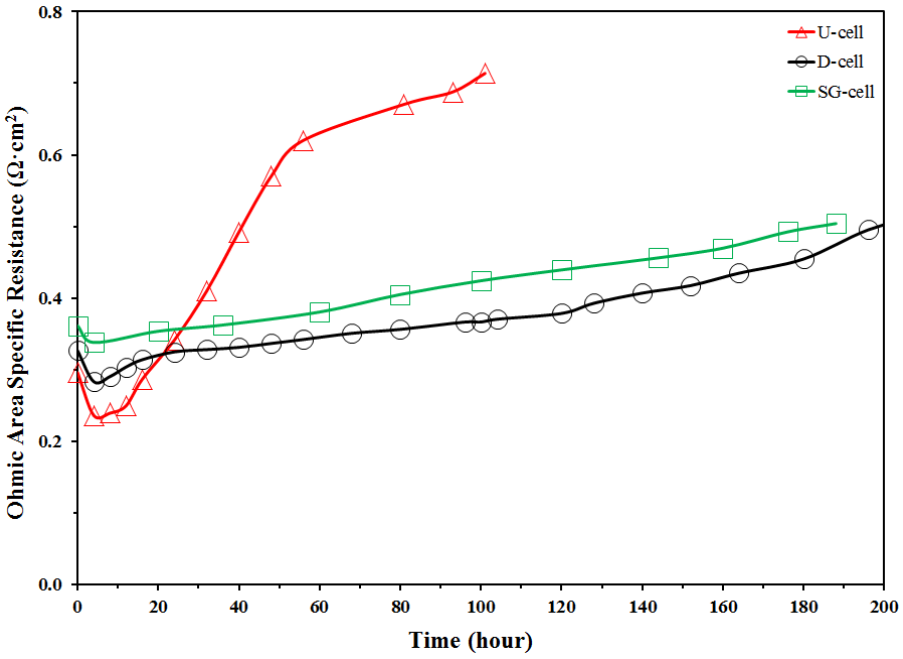

(a)

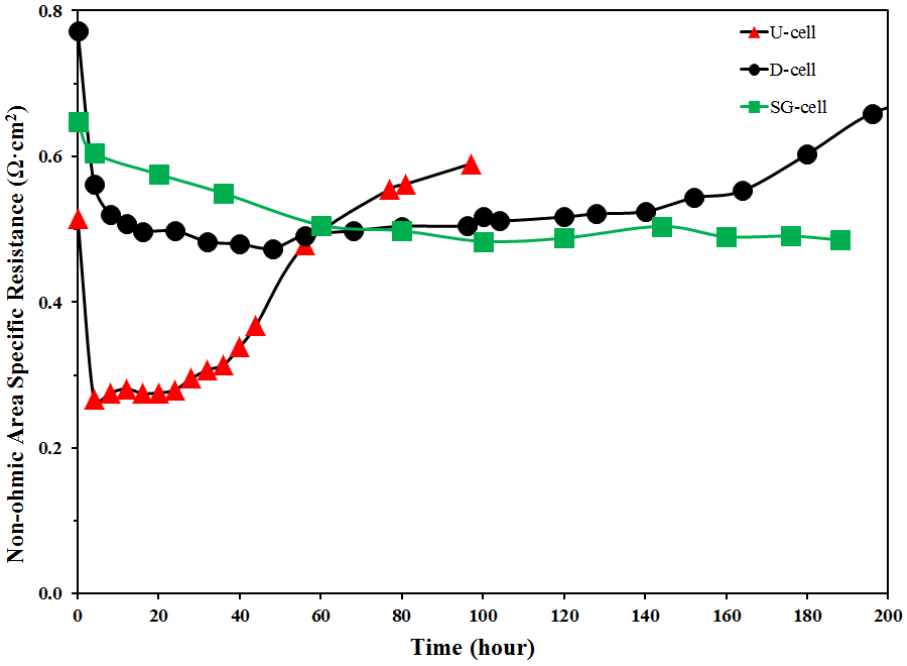

(b)

Figure 6.6 Changes in (a) ohmic resisitance (b) non-ohmic resistance with time for U, D and SG-cells

6.3.2 Delamination Observation

Post-test observations (Figure 6.7) showed no delamination between the cathode electrode and electrolyte for all the tested cells. Observations on the anode electrode adherence, however, varied. For the U-cell, the anode delaminated completely from the substrate, leaving behind a dark-colored imprint on the electrolyte. For the D-cell, similar delamination was observed. For the SG-cell, the anode layer remained firmly adhered to the substrate.

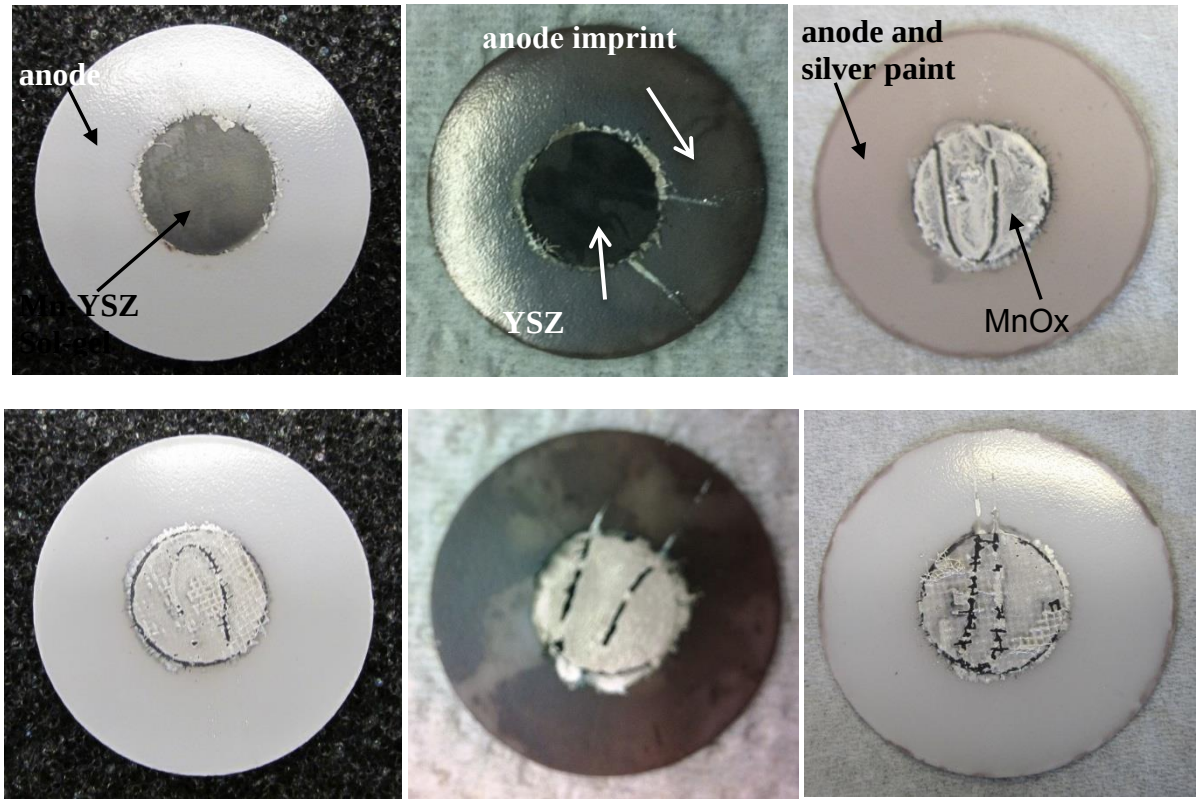

(a) U-cell (b) D-cell (c) SG-cell

Figure 6.7 Optical image of cell anode side after delamination test

6.3.4 SEM-EDS

The surface morphology of the Mn-YSZ diffusion layer and sol-gel coating are shown in Figure 6.8, and the as-received YSZ electrolyte is shown as control. The YSZ surface shows typical dense granular structure with well-defined grain boundaries and localized isolated pores formed during sintering. The Mn diffusion into the YSZ lattice leads to the grain size growth and keeps the dense structure. The sol-gel coating showed the formation of a discontinuous surface layer. The tilted view and high magnification picture of sol-gel coating were shown in Figure 6.10. The porous coating has interconnected channels on the surface and submicron pores in the bulk. The electrode-electrolyte interface morphologies (obtained after the dissolution of electrode) of the tested cells are shown in Figure 6.9. For the un-doped YSZ cell, the electrolyte

surface shows the high coverage of small particles, which is identified to be the reaction product LZ by EDS (Figure 6.11). For the Mn-YSZ diffusion cell, one part of the electrolyte area shows coverage of the needle-shape reaction product, the other part shows a peripheral impression of the electrode in the form of elevated ridges. For the Mn-YSZ sol-gel cell, one part of the electrolyte area shows the coverage of the reaction products, another part shows the sol-gel coating structure.

Energy dispersive x-ray spectroscopy of the anode-side electrolyte after testing at 0.8 V showed some lanthanum, strontium, and manganese left by the anode, in addition to the expected zirconium from the electrolyte (Figure 6.11). Since LSM dissolved in hydrochloric acid, the lanthanum signal supposed to come from $La_2Zr_2O_7$, which is consistent with the XRD detection of lanthanum zirconate phase. In LZ rich area (13.1% La), the Lanthanum content was much higher than LZ uncovered area (1.2% La).

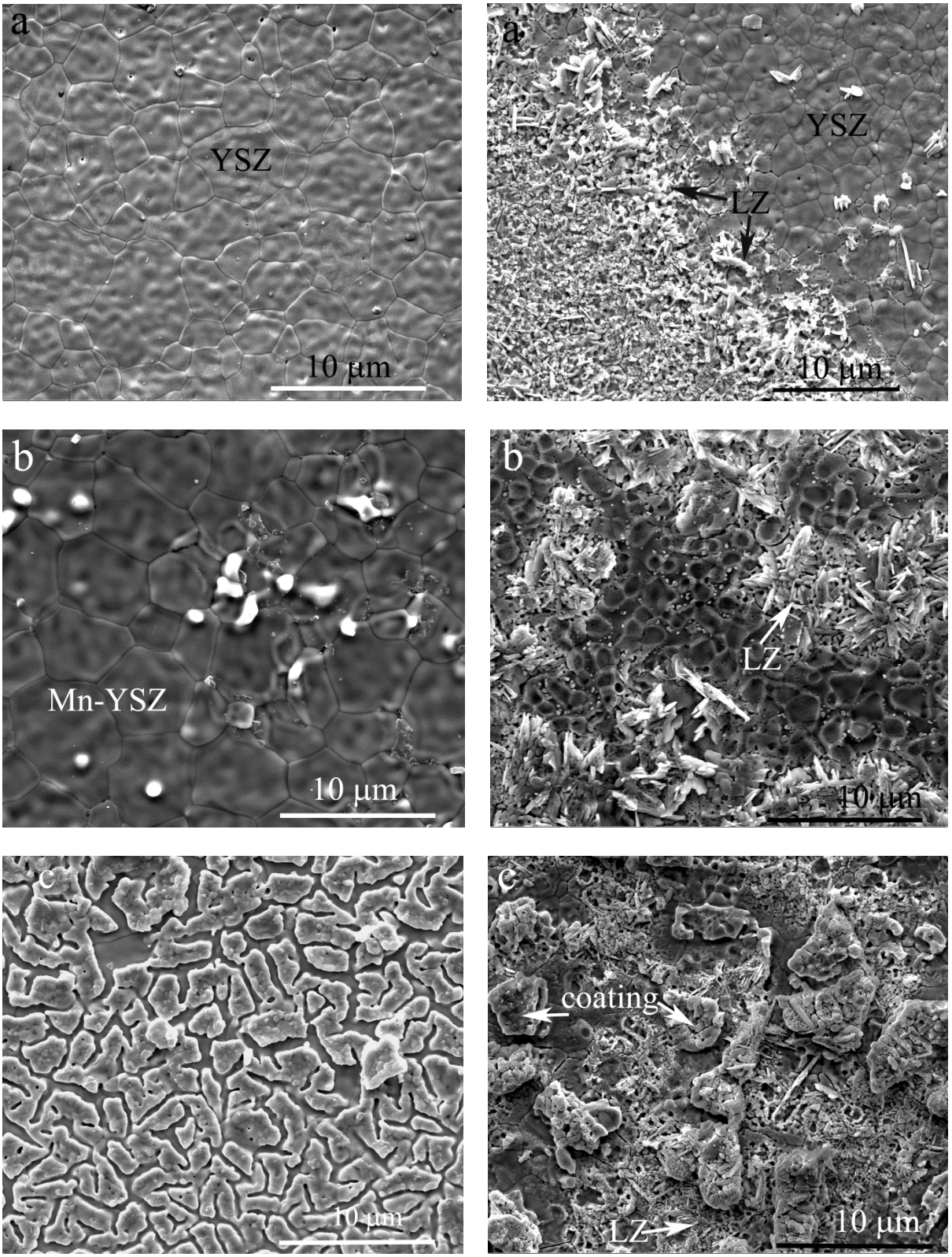
a
YSZ
10 µm
a
YSZ
LZ
10 µm
b
Mn-YSZ
10 µm
b
LZ
10 µm
c
10 µm
c
coating
LZ
10 µm

Figure 6.8 Surface morphology of the electrolyte-anode interface for as-fabricated cells

(a) U-cell, (b) D-cell, and (c) SG-cell

Figure 6.9 Surface morphology of the electrolyte-anode interface after testing and dissolving LSM

(a) U-cell, (b) D-cell, and (c) SG-cell

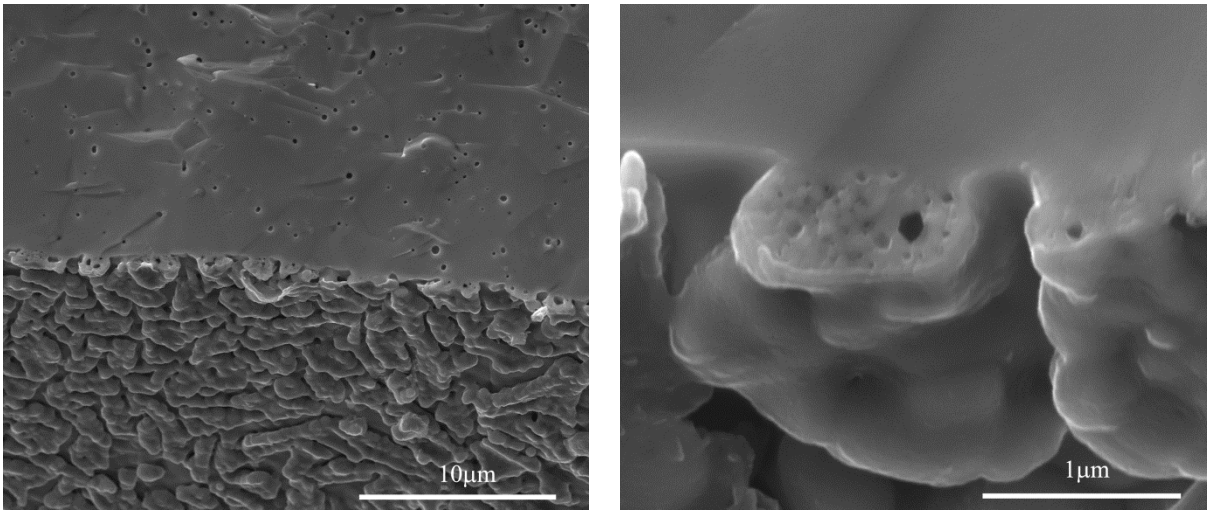

Figure 6.10 SEM morphology of sol-gel coating

(a) interconnected channels on the surface (b) submicron pores in the bulk

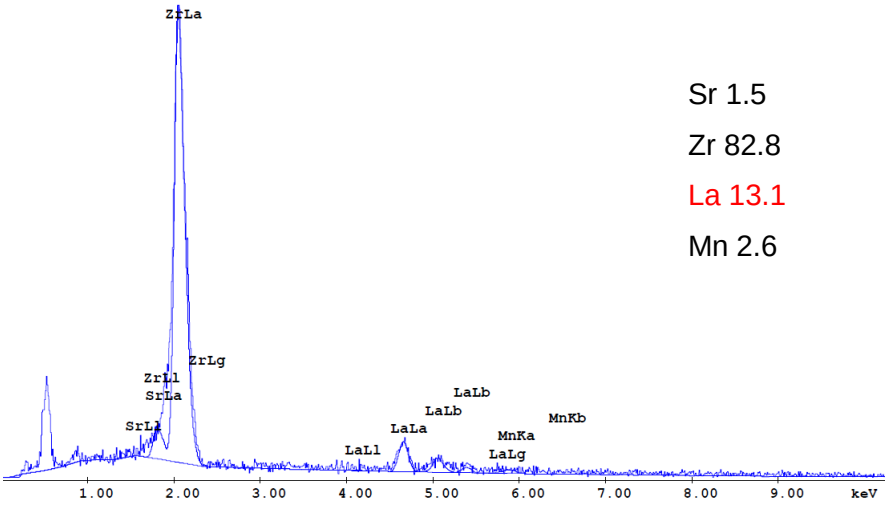

(a)

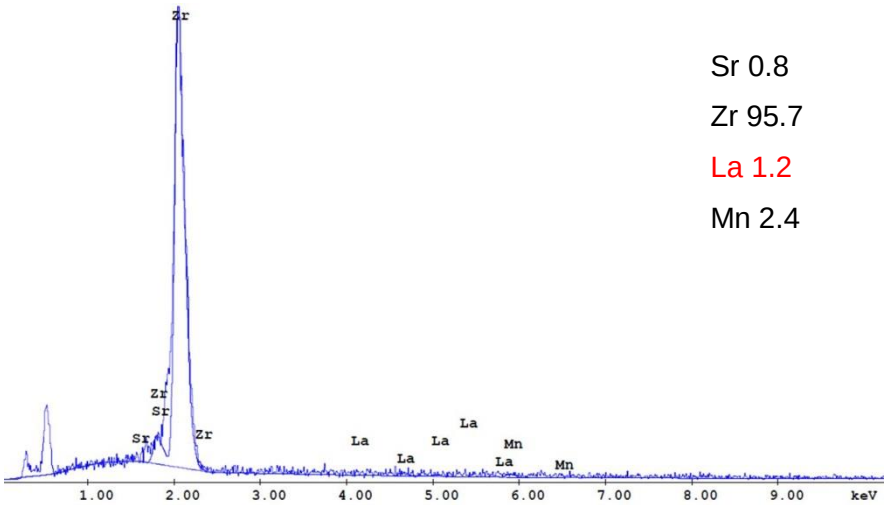

(b)

Figure 6.11 EDS of electrolyte-anode interface after testing and dissolving LSM
(a) LZ covered area (b) LZ uncovered area

6.3.4 XRD

Figure 6.12 shows X-ray diffraction patterns from electrolyte surfaces of electrochemically tested cells after dissolving of the electrodes in hydrochloric acid. Diffraction patterns are shown for YSZ cell, Mn-YSZ diffusion cell and Mn-YSZ sol-gel cell. The y-scale (peak intensity) was magnified to reveal the lower-intensity peaks of reaction compounds. The

lanthanum zirconate ($La_2Zr_2O_7$) diffraction pattern (JCPDS 00-050-0450) is identified at anode side only. The undoped cell has the highest peak of LZ, and then is the diffusion cell; the sol-gel cell has the lowest peak. The relative content of LZ to YSZ was calculated semi-quantitatively and shown in table1. The Mn doping decreased the LZ content, and the sol-gel cell has lower LZ content than diffusion cell. This phenomenon may relate to the Mn content and distribution in the Mn-YSZ interlayer. The Mn content on the surface for both cells was detected by EDS as 2% to Zr, but the distribution is different. Firstly, the Mn in the interlayer alleviated the diffusion of Mn from LSM to YSZ, which is believed to trigger the LSM-YSZ interaction, so decreased the LZ production rate. Secondly, the solid diffusion experiment created a Mn concentration gradient high at the LSM side; however the sol-gel experiment created a uniform Mn distribution in the Mn-YSZ interlayer. The uniform Mn distribution has better prevention effect than this gradient distribution.

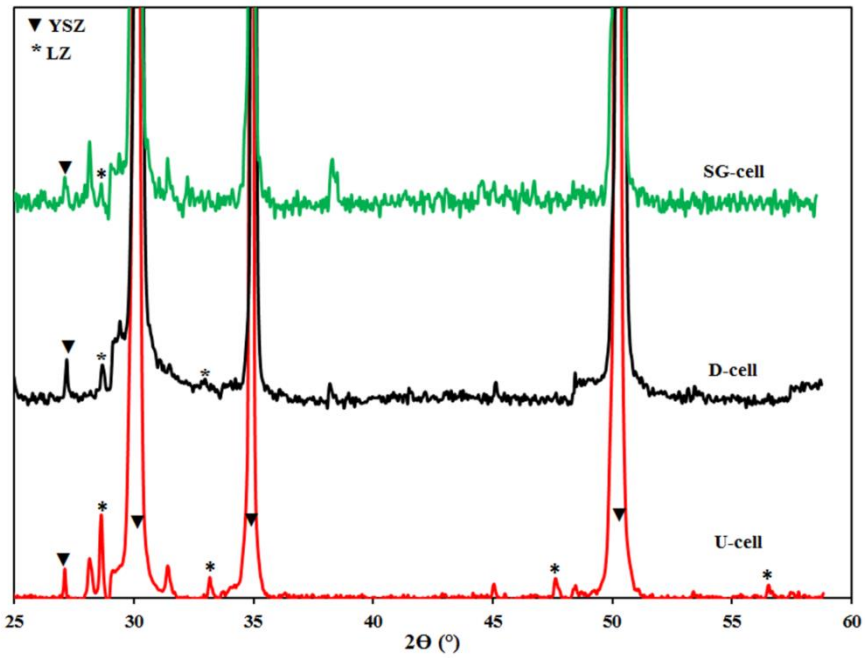

Figure 6.12 X-ray diffraction patterns of anode-side electrolyte surfaces after etching in hydrochloric acid

6.4 Discussion

The formation of the ridges was explained as the impression of the LSM in the YSZ due to the nucleation of epitaxial Mn-YSZ at the triple phase boundary (TPB) during sintering[23,122,186]. It has been proposed that the diffusion of manganese into the YSZ results in an excess of lanthanum in the LSM and subsequent surface diffusion of La^{3+} and Zr^{4+} cations towards the electrode–electrolyte interface causes the formation of lanthanum zirconate phase. The lanthanum zirconate formation is attributed to the evolution of oxygen at this interface according to reaction:

$$LaMnO_3 + ZrO_2 + 0.25O_2 \leftrightarrow 0.5La_2Zr_2O_7 + MnO_2 \quad (6.1)$$

The degradation rates of ohmic and non-ohmic resistance and the LZ content in the first 100h testing were summarized in table 6.1. It shows a correlation between LZ content and degradation in both ohmic and non-ohmic resistances. The Mn-doped cell has lower LZ content and lower ohmic and non-ohmic degradation rates. The ohmic resistance increase is explained by the loss of the contact. The non-ohmic resistance increase is explained through the loss of TPB length resulting in a decrease in the area available for oxygen reduction and evolution. The main loss after 4 hours is due to ohmic resistance increase. The LZ coverage of the interface lost the contact of LSM-YSZ and decreased the TPB length, increased both the ohmic and non-ohmic resistance. The Mn-YSZ interlayer prevented the diffusion of Mn and alleviated the LZ formation, resulted in the slower degradation of the resistance. The cell performance is very close for diffusion cell and sol-gel cell in the first 100h, but the diffusion cell has higher LZ content than the sol-gel cell. There is no evidence showing the correlation between the final LZ content and delamination, between overall resistance and delamination (table 6.2). In general, the lower LZ content at the end of testing corresponds to the smaller total resistance. The lower LZ

content and resistance of the diffusion cell running for 100h delaminated, however, the sol-gel cell which has higher LZ content and resistance running for 244h did not delaminate.

Table 6.1 Ohmic (RΩ) and non-ohmic resistance (Rnon-Ω) change and average LZ formation rates

Cell	R_{Ω} change rate ($\Omega \cdot cm^2$/ 100 h)		$R_{non-\Omega}$ change rate ($\Omega \cdot cm^2$/ 100 h)		Average LZ/YSZ formation rates (100h)
	4-100h	100-200h	4-100h	100-200h	
U-cell	0.56	-	0.38	-	0.74%
D-cell	0.09	0.17	-0.14	0.10	0.38%
SG-cell	0.09	0.07	-0.13	0.01	0.17%

Table 6.2 The total resistance, LZ content and anode delamination for representative cells at the end of testing

Cell	LZ/YSZ content at the end of testing	Total resistance (Ω)	Testing time (h)	Anode delamination
U-cell #41	0.74%	1.72	100	yes
D-cell #1	0.33%	0.86	100	yes
SG-cell #6	0.64%	1.20	244	no

Both Mn-doping layer by solid diffusion and sol-gel method decreased the LZ content, slowed down the resistance degradation rate, and showed more stable current compared to the undoped YSZ cell, but all the Mn-YSZ diffusion cells delaminated, the sol-gel cells did not delaminate. The common character of these two cells is Mn-doping, the difference is that the diffusion cell has a dense Mn-YSZ layer, but sol-gel cell has a highly porous Mn-YSZ layer. The common Mn-doping character related to the common better performance, on the other hand the different character related to the different delamination behavior. The Mn-doping YSZ make Mn excess at the interface, and the excess Mn can slow down the reaction between LSM and YSZ,

either by A site deficient LSM or by Mn excess YSZ. The poor conductivity of the reaction product LZ is responsible for degradation and for part of the ohmic and non-ohmic resistance increase. The LZ content was decreased by Mn-doping, and then the cell degradation rate was decreased accordingly. The dense Mn-YSZ layer did not inhibit the delamination, but the porous Mn-YSZ layer did. That means the porous structure is important for delamination. Usually the sol-gel coating has high surface area and a microscopic porous structure. The high oxygen pressure at the anode-electrolyte interface is the most related factor responsible for the delamination of the anode and electrolyte. According to Virkar's theory [187], the oxygen pressure can build up as high as 10^{13} atm at the anode-electrolyte interface; this high porous and surface area interlayer can absorb more oxygen molecular and help the passage of the oxygen to LSM, and avoid the delamination in long term testing.

Figure 6.13 shows schematic representations of the proposed degradation processes at the anode-electrolyte interfaces of the U-cell (a), D-cell (b), and SG-cell (c). High oxygen pressure buildup at the anode-electrolyte interface results in grain boundary (GB) porosity in the YSZ and anode delamination as shown above. The adherence of the anode with the electrolyte in the SG-cell is hypothesized to be due to the presence of porous interlayer as shown in Figure 6.10.

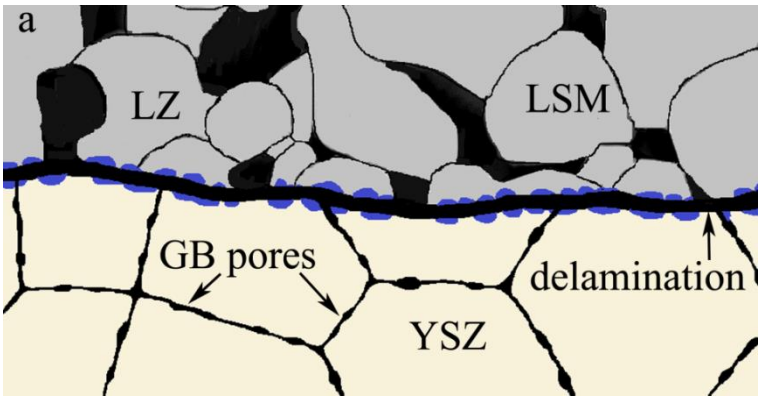

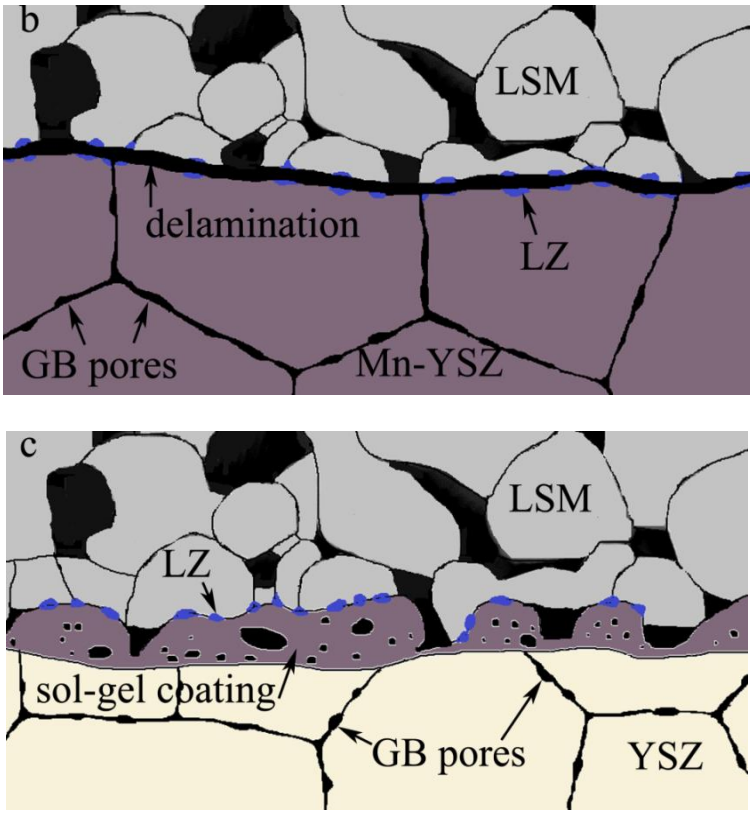

Figure 6.13 Schematic representations of the degradation at the anode-electrolyte interfaces (a) U-cell (b) D-cell (c) SG-cell

6.5 Optimizing Sol-Gel Coating

Since the SG-cell showed improved electrical performance and also prevented delamination, the sol-gel process was investigated in detail to get an optimized condition. The sol-gel coating alleviated the Mn diffusion from LSM to YSZ, so increasing the thickness or doping more Mn into the Mn-YSZ interlayer may improve the cell performance. The sol-gel coating is very thin; to get a homogeneous covering on the substrate, several layers of coating is usually adopted. SG-cell with three layers and six layers of Mn-YSZ sol-gel coating were prepared respectively.

Figure 6.14 (a) shows the plots of current density during tests in 100h with U-cell and 3-layer SG-cell. The U-cell exhibit a maximum followed by a steep drop. The three SG-cells show

highly repetitive data. They all exhibit more stable electrical performance than the undoped cell in 100h testing. The little stage around 20h is because of the adjusting furnace temperature manually to match the setting temperature. The little temperature drop about 2°C gives distinct effect on the current density output. Figure 6.14 (b) shows the representative current density data in 500h for 3-layer and 6-layer SG-cell, the U-cell is used as reference. The U-cell performance degrade very fast, it decrease to 0.50A·cm^{-2} around 100h. The 3-layer SG-cell slowed down the degradation, it decrease to 0.90A·cm^{-2} around 200h. The 6-layer SG-cell showed very stable performance in 500h, it maintain 1.15A·cm^{-2} during the testing.

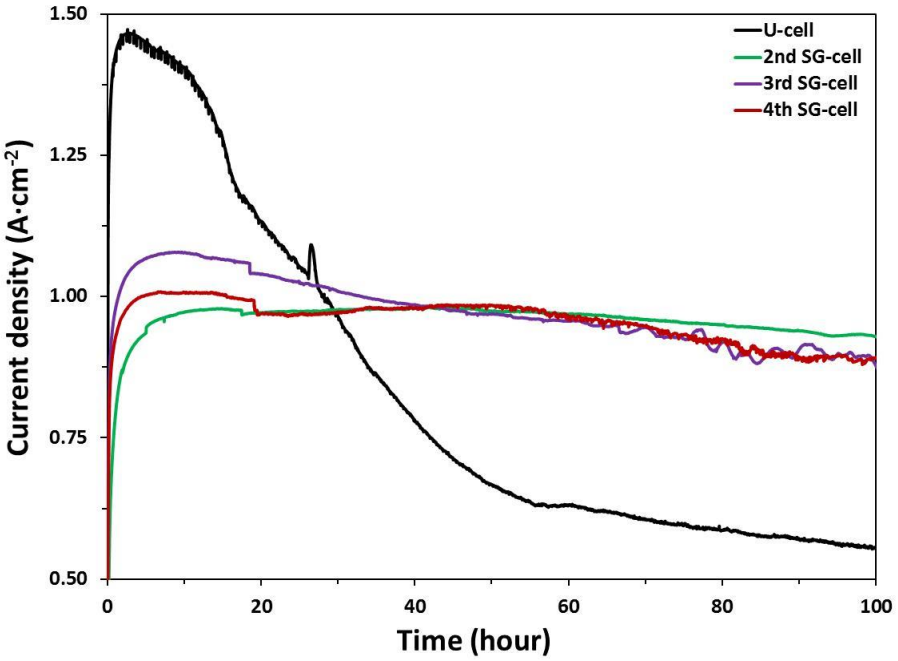

(a) U-cell and several typical 3-layer SG-cells in 100h testing

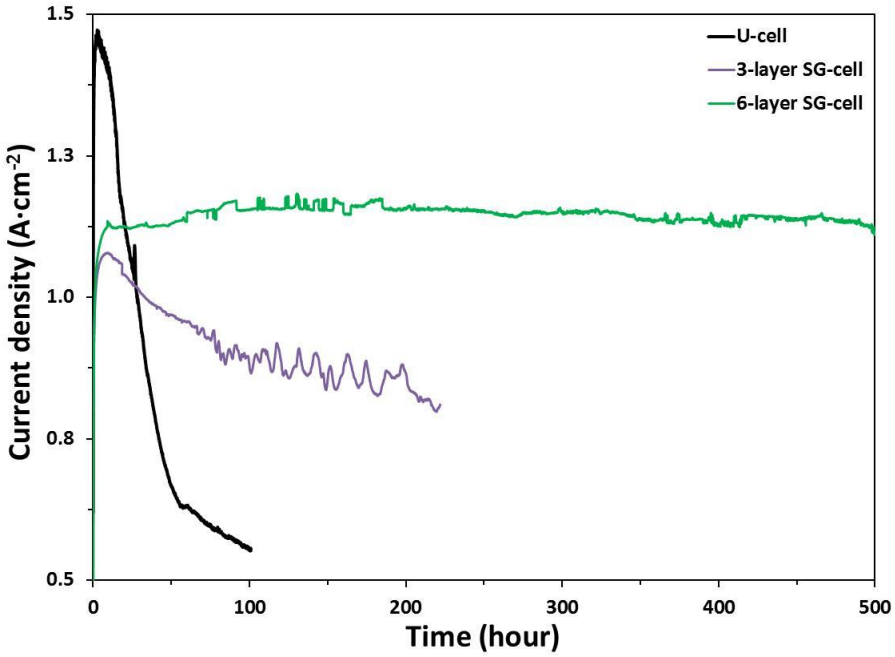

(b) U-cell, 3-layer SG-cell and 6-layer SG-cell in 500h testing

Figure 6.14 Changes in current density with time

Figure 6.15 (a) represents the ohmic resistance trend for different cells. All the cells show an increase in ohmic resistance after the initial decrease in 4h; the undoped cell shows rapid increase, the 3-layer SG-cell shows slower increase, 6-layer SG-cell shows the slowest increase. The doped cells show higher starting resistance than the undoped cell, however, they show much lower resistance at the end of longer term testing. Figure 6.15 (b) represents the non-ohmic resistance trend for different cells. All the cells show an initial sharp decrease after 4h. After that, U-cell experienced a rapid increase in 100h. However, the SG-cells show a rapid decrease of non-ohmic resistance in 100h. Then the SG-cells show a stable zone of non-ohmic resistance change about several hundred hours, finally there is a very slow increasing zone. The 3-layer and 6-layer SG-cell show similar starting non-ohmic resistance, but the 6-layer SG-cell experienced a bigger decrease during the testing. The initial decrease in both ohmic and non-ohmic resistances can be explained in the previous by electrode conditioning process related with a re-equilibrium

process of surface strontium or extension of TPB by manganese doping of the electrolyte.[183,185] The slower increase of ohmic resistance of SG-cell than U-cell and the decrease instead of increase of non-ohmic resistance support the better cell performance of SG-cell than U-cell. Similarly, the 6-layer SG-cell exhibits a slower increase of ohmic resistance and a faster decrease of non-ohmic resistance than 3-layer SG-cell, which supports the better current stability of 6-layer SG-cell.

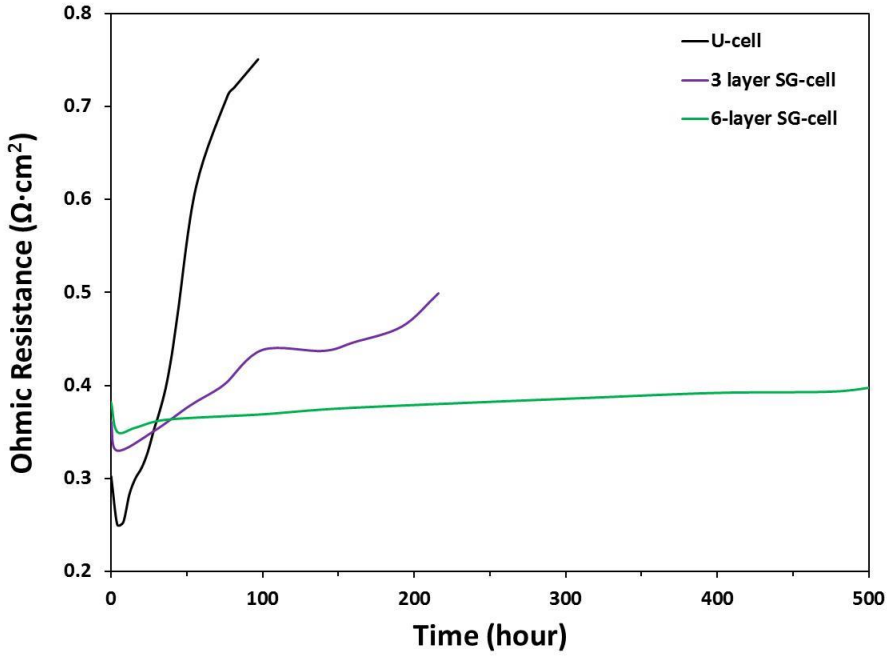

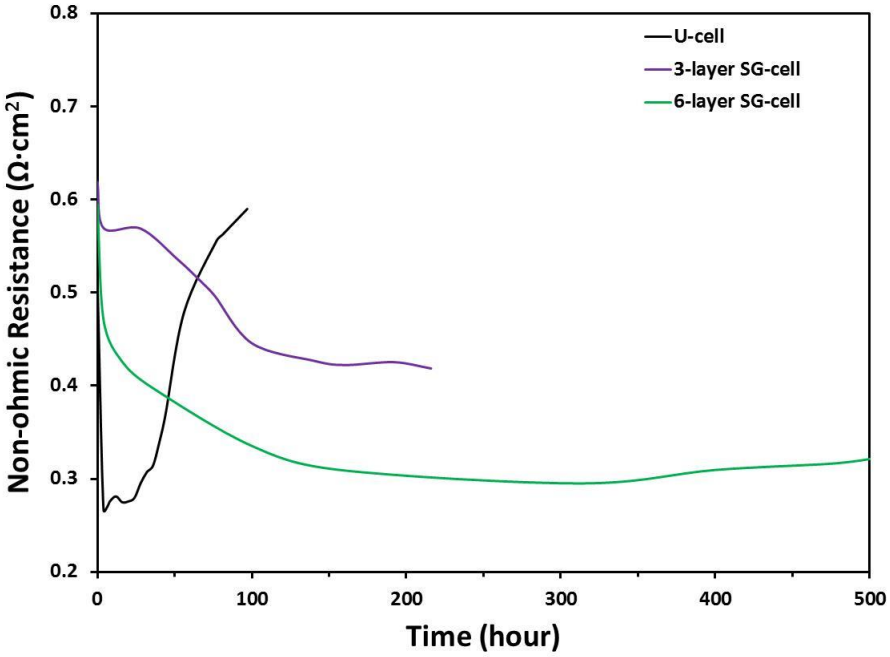

Figure 6.15 Changes in ohmic (a) and non-ohmic (b) resistance with time for 3-layer and 6-layer SG-cells

Figure 6.16 shows X-ray diffraction patterns from electrolyte surfaces of electrochemically tested cells after dissolving of the electrodes in hydrochloric acid. Diffraction patterns are shown for YSZ baseline cell, 3-layer SG-cell and 6-layer SG-cell. The spectrum was normalized to the highest YSZ (111) peak and the y-scale was magnified to reveal the lower-intensity LZ peaks. The lanthanum zirconate ($La_2Zr_2O_7$) diffraction pattern (JCPDS 00-050-0450) is identified at anode side only. The undoped cell has the highest peak of LZ, and then is 3-layer SG-cell; the 6-layer SG-cell has the lowest peak. The thicker sol-gel coating decreased the LZ content, since more Mn was incorporated in the coating to alleviate Mn diffusion from LSM to YSZ.

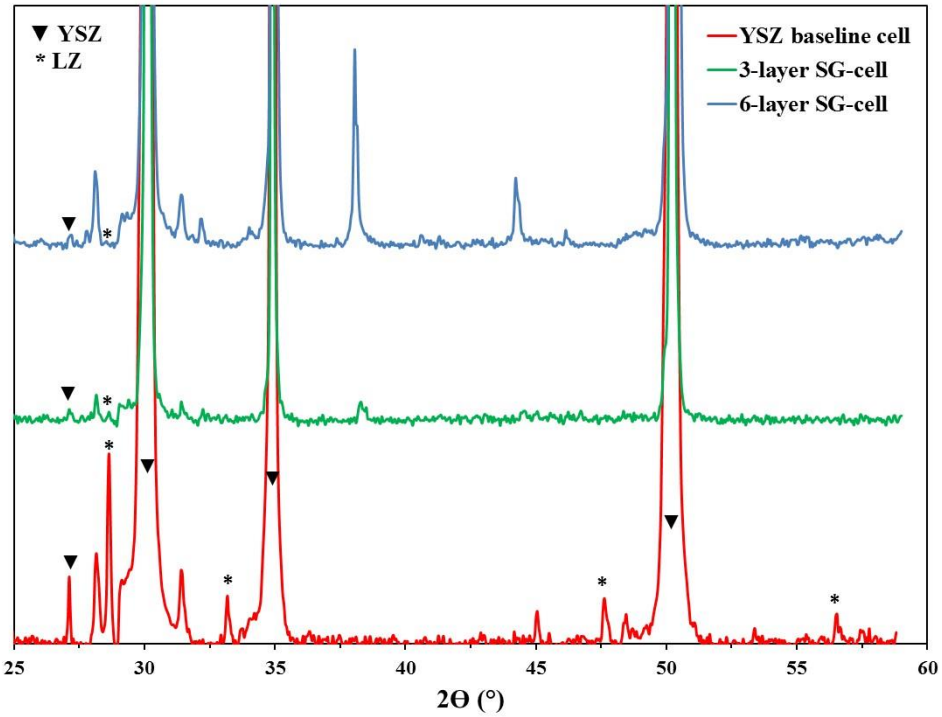

Figure 6.16 X-ray diffraction patterns of anode-side electrolyte surfaces after etching in hydrochloric acid

6.6 Conclusion

The SOEC performance has been improved by using a Mn-YSZ interlayer on symmetric cells of the configuration air/LSM//YSZ//LSM/air. Both solid state diffusion and sol-gel coating two doping method can improve the performance; however, anode delamination can only be prevented by sol-gel method. Mn-doping interlayer can improve the cell performance by alleviating lanthanum zirconate formation and morphological changes at the anode–electrolyte interface. The sol-gel structure with high surface area and porosity is responsible for the prevention of delamination by release the oxygen pressure at the anode side. The sol-gel interlayer could be optimized by increasing the thickness to stabilize the SOEC electrochemical performance for 500h.

Chapter 7 Summary and Recommendations for Future work

The chemical and structural stability of LSM-YSZ composite, the reversibility and the prevention of LSM-YSZ interaction has been successfully investigated. The stability of porous LSM-YSZ composite has been examined as a function of oxygen partial pressure, sintering temperature, sintering time, density, starting powder. Oxygen partial pressure played an important role during sintering. Lower PO_2 exposures enhanced $La_2Zr_2O_7$ formation and preferentially degrade the stability of the LSM-YSZ composite. Lower PO_2 exposure enhanced densification and grain growth. Lower PO_2 exposure decreased the TEC value of the composite. Elemental inter-diffusion across the LSM-YSZ grain boundaries as well as the thermodynamic stability of the LSM-YSZ composite in the studied conditions causes the formation of new compounds such as $La_2Zr_2O_7$ and MnO_x. Thermal expansion coefficient of the composite decreased with increase in the amount of the zirconate phases. The reaction between LSM and YSZ in lower PO_2 tends to be reversed back when re-sintered in air. Mn diffusion from LSM to YSZ is critical and initiated the LSM-YSZ reaction. The reaction between LSM and YSZ can be alleviated by doping Mn into YSZ to slow down the diffusion from LSM to YSZ.

The SOEC performance has been improved by using a Mn-YSZ interlayer on symmetric cells of the configuration air/LSM//YSZ//LSM/air. Both solid state diffusion and sol-gel coating two doping method can improve the performance; however, anode delamination can only be prevented by sol-gel method. Mn-doping interlayer can improve the cell performance by alleviating lanthanum zirconate formation and morphological changes at the anode–electrolyte interface. The sol-gel structure with high surface area and porosity is responsible for the prevention of delamination by release the oxygen pressure at the anode side.

Based on the work presented in this dissertation, the following is recommended in future

(1) It is recommended that the role of Mn doping content and the thickness of Mn-YSZ interlayer for electrode /electrolyte interfacial stability should be further examined.

(2) It is recommended that other method should be explored to prepare the interlayer, for example PLD (pulsed laser deposition), which may provide a uniform and dense Mn-YSZ layer. Comparing with the two methods already applied in the dissertation, the contribution of porous and dense structure to the air electrode delamination could be understood deeply.

(3) It is recommended that a porous YSZ sol-gel coating could be prepared between LSM and YSZ, comparing with the porous Mn-YSZ sol-gel coating, to evaluate the Mn doping effect on the electrochemical performance and anode delamination.

(4) It is also recommended that the long term performance and structural stability (>1000h) for SOEC full cell tests should be evaluated using advanced operando and in-situ techniques to understand bulk and interface degradation phenomena.

(5) Role of possible contaminants should be examined along with co-electrolysis of H_2O and CO_2, such as Si, Al, Na and Cr, which are very common in the experiment and degrade the cell performance a lot.

Appendix Copyright Permissions

Figure 1.1: From Ni-YSZ to sulfur-tolerant anode materials for SOFCs: electrochemical behavior, in situ characterization, modeling, and future perspectives, Z. Cheng, J. Wang, Y. Choi, L. Yang, M. C. Lin and M. Liu, Energy Environ. Sci., 4 (2011) 4380-4409, Reproduced by permission of The Royal Society of Chemistry.

Figure 1.5: Fergus, J. W., Electrolytes for solid oxide fuel cells, J. Power Sources162 (2006) 30–40, Reproduced by permission of Elsevier.

Figure 1.7: J. R. Mawdsley, J.D. Carter, A.J. Kropf, B. Yildiz, V.A. Maroni, Post-test evaluation of oxygen electrodes from solid oxide electrolysis stacks, Int. J. Hydrogen Energy 34 (2009) 4198–4207, Reproduced by permission of International Journal of Hydrogen Energy.

Chapter 2 & 5: Manoj K. Mahapatra, Sanjit Bhowmick, Na Li and Prabhakar Singh, Role of Oxygen Partial Pressure on the Stability of Lanthanum Strontium Manganite – Yttria Stabilized Zirconia Composite, Journal of the European Ceramic Society, 32 (2012) 2341-2349, Reproduced by permission of Elsevier.

Chapter 3: Na Li, Manoj K. Mahapatra and Prabhakar Singh, Sintering of porous strontium doped lanthanum manganite-yttria stabilized zirconia composite in controlled oxygen atmosphere at 1400 °C, Journal of Power Sources 221 (2013) 57-63, Reproduced by permission of Elsevier.

Chapter 5: Manoj K. Mahapatra, Na Li, Atul Verma, Prabhakar Singh, Electrical conductivity of manganese doped yttria (8 mol %) stabilized zirconia, Solid State Ionics, 253 (2013) 223-226, Reproduced by permission of Elsevier.

Chapter 6: Na Li, Michael Keane, Manoj K. Mahapatra, Prabhakar Singh, Mitigation of the delamination of LSM anode in solid oxide electrolysis cells using manganese-doped YSZ interlayer, International Journal of Hydrogen Energy 38(2013) 6298-6303, Reproduced by permission of International Journal of Hydrogen Energy.

REFENRENCES

[1] S.P.S. Badwal & K. Foger, Solid oxide electrolyte fuel cell review, Ceramics International 22 (1996) 257-265
[2] EG&G Technical Services Inc., Fuel cell handbook 2004, Seventh Edition.
[3] Ekaterina V. Tsipis & Vladislav V. Kharton, Electrode materials and reaction mechanisms in solid oxide fuel cells: a brief review. I. Performance-determining factors, J Solid State Electrochem. 12 (2008)1039–1060.
[4] Mekhilef, S., R. Saidur and A. Safari, Comparative study of different fuel cell technologies, Ren.Sustain. Energy. Rev.16 (2012) 981– 989.
[5] Stambouli, A. B., Fuel cells: the expectations for an environmental-friendly and sustainable source of energy, Ren.Sustain. Energy. Rev.15 (2011) 4507– 4520.
[6] Ge L., A. Verma, R. Goettler, D. Lovett, R.K. Singh Raman and P. Singh, Oxide scale morphology and chromium evaporation characteristics of alloys for balance of plant applications in solid oxide fuel cells, Metal. Mater. Trans. 44A (2013) S193-S206.
[7] Shaffer, S., Solid oxide fuel cell development for transportation and stationary applications: latest update on stack and system performance, Fuel Cell Seminar 2009.
[8] Jansen, D. and J.W. Dijkstra, CO_2 capture in SOFC-GT systems, Second Annual Conference on Carbon Sequestration, May 2003, Alexandria, Virginia, USA.
[9] Schlitzberger, C., N. O. Brinkmeier and R. Leithner, CO_2 capture in SOFC by vapor condensation and CH_4 production in SOEC storing excess electricity, Chem. Eng. Technol. 35(2012) 440–444.
[10] Spallina, V., M. C. Romano, S. Campanari and G. Lozza, A SOFC-based integrated gasification fuel cell cycle with CO_2 capture, J. Eng. Gas Turbines and Power 133(2011) 071706
[11] Wee, J. H., Contribution of fuel cell systems to CO_2 emission reduction in their application fields, Ren.Sustain. Energy. Rev.14 (2010) 735–744.
[12] Zhe Cheng, Jeng-Han Wang, YongMan Choi, Lei Yang, M. C. Lin and Meilin Liu, From Ni-YSZ to sulfur-tolerant anode materials for SOFCs: electrochemical behavior, in situ characterization, modeling, and future perspectives, Energy and Environmental Science 4 (2011) 4380-4409
[13] R. Vassen, X. Cao, F. Tietz, D. Basu, and D. Stöver, Zirconates as new materials for thermal barrier coatings, J. Am. Ceram. Soc. 83 (2000) 2023-2028.
[14] Jasinski, P., W. Lewandowska-Iwaniak and S. Molin, Metal supported solid oxide fuel cells – selected aspects, Mater. Sci. Eng. 18 (2011) 132004.
[15] Tucker, M. C., Progress in metal-supported solid oxide fuel cells: a review, J. Power Sources 195 (2010) 4570–4582.
[16] Minh, N. Q., Solid oxide fuel cell technology-features and applications, Solid State Ionics 174 (2004) 271–277.
[17] Virkar, A. V., SOFC materials and processing issues, SECA Core Technology Program Workshop 2001.
[18] Virkar, A. V., J. Chen, C. W. Tanner and J.W. Kim, The role of electrode microstructure on activation and concentration polarizations in solid oxide fuel cells, Solid State Ionics 131(2000) 189-198.
[19] Carter, J. D., Ceramic Fuel Cells, DOE H_2/FC Manufacturing R&D Workshop (SOFC) 2011.

[20] L. J. Gauckler, D. Beckel, B. E. Buergler, E. Jud, U. P. Muecke, M. Prestat, J. L. M. Rupp, and J. Richter, Solid oxide fuel cells: systems and materials, Chimia 58 (2004), 837-850.
[21] C. Brugnoni, U. Ducati, and M. Scagliotti, SOFC cathode/electrolyte interface. part I: reactivity between $La_{0.8}Sr_{0.2}MnO_3$ and ZrO_2-Y_2O_3, Solid State Ionics 76 (1995) 177-182.
[22] H. Y. Lee and S. M. Oh, Origin of cathodic degradation and new phase formation at the $La_{0.9}Sr_{0.1}MnO_3$/YSZ interface, Solid State Ionics 90 (1996) 133-140.
[23] A. Mitterdorfer and L. J. Gauckler, $La_2Zr_2O_7$ formation and oxygen reduction kinetics of the $La_{0.85}Sr_{0.15}$ Mn_yO_3, O_2 (g)/YSZ system, Solid State Ionics 111 (1998) 185-218.
[24] Fergus JW, Metallic interconnects for solid oxide fuel cells, Mater Sci Eng A Struct Mater Prop Microstruct Process 397(2005) 271-283.
[25] C. S. Tedmon, H. S. Spacil, and S. P. Mitoff, Cathode materials and performance in high-temperature zirconia electrolyte fuel cells, J. Electrochem. Soc. 116 (1969) 1170-1175.
[26] De Jonghe LC, Jacobson CP, Visco SJ, Supported electrolyte thin film synthesis of solid oxide fuel cells, Annu Rev Mater Res 33(2003) 169-182.
[27] Ivers-Tiffee E, Weber A, Herbstritt D, Materials and technologies for SOFC-components, J Eur Ceram Soc 21(2001) 1805-1811.
[28] Ming Chen, Understanding the thermodynamics at the LaMnO3-YSZ interface in SOFC, PhD thesis 2005, Swiss Federal Institute of Technology
[29] Fergus, J. W., Electrolytes for solid oxide fuel cells, J. Power Sources162 (2006) 30–40.
[30] Jacobson, A. J., Materials for solid oxide fuel cells, Chem. Mater. 22 (2010) 660–674.
[31] Weller, M., F. Khelfaoui, M. Kilo, M.A. Taylor, C. Argirusis and G. Borchardt, Defects and phase transitions in yttria- and dcandia-doped zirconia, Solid State Ionics 175 (2004) 329–333.
[32] Kurumada, M., H. Hara and E. Iguchi, Oxygen vacancies contributing to intragranular electrical conduction of yttria-stabilized zirconia (YSZ) ceramics, Acta Mater. 53 (2005) 4839–4846.
[33] Inaba, H. and H.Tagawa, Ceria-based Solid Electrolytes, Solid State Ionics 83 (1996) 1- 16.
[34] Guan, X., H. Zhou, Y. Wang and J. Zhang, Preparation and properties of Gd^{3+} and Y^{3+} Co-doped ceria-based electrolytes for intermediate temperature solid oxide fuel cells, J. Alloys Compounds 464 (2008) 310–316.
[35] Podpirkaw, A. and S. Ramanathan, Transference numbers for in-plane carrier conduction in thin film nanostructured gadolinia-doped ceria under varying oxygen partial pressure, J. Am. Ceram. Soc. 92 (2009) 2400–2403.
[36] Schefold, J., A. Brisse and M. Zahid, Solid oxide cells operated in high temperature water electrolysis electronic conduction of yttria-stabilized zirconia electrolyte in solid oxide cells operated in high temperature water electrolysis, J. Electrochem. Soc. 156 (2009) B897-B904.
[37] Kim, J. H. and H.Yoo, Partial electronic conductivity and electrolytic domain of $La_{0.9}Sr_{0.1}Ga_{0.8}Mg_{0.2}O_{3-\delta}$, Solid State Ionics 140 (2001) 105–113.
[38] Sun, C. and U. Stimming, Recent anode advances in solid oxide fuel cells, J. Power Sources 171 (2007) 247–260.
[39] Koide, H., Y. Someya, T. Yoshida and T. Maruyama, Properties of Ni/YSZ cermet as anode for SOFC, Solid State Ionics 132(2000) 253–260.
[40] Pihlatie, M., A. Kaiser and M. Mogensen, Redox stability of SOFC: thermal analysis of Ni–YSZ composites, Solid State Ionics180 (2009) 1100–1112.
[41] Ettler, M., H. Timmermann, J. Malzbender, A. Weber and N.H. Menzler, Durability of Ni anodes during reoxidation cycles, J. Power Sources 195 (2010) 5452–5467.

[42] Heo, Y. H., J. W. Lee, S. B. Lee, T. H. Lim, S. J. Park, R. H. Song, C. O. Park and D. R. Shin, Redox-induced performance degradation of anode-supported tubular solid oxide fuel cells, Int. J. Hyd. Energy 36 (2011) 797-804.

[43] Pihlatie, M., A. Kaiser, P. H. Larsen and M. Mogensen, Dimensional behavior of Ni–YSZ composites during redox cycling, J. Electrochem. Soc.156 (2009) B322-B329.

[44] Lankin, M., Y. Du and C. Finnerty, A review of the implications of silica in solid oxide fuel cells, J. Fuel Cell Sci. Technol. 8 (2011) 054001.

[45] Hauch, H., S. H. Jensen, J. B. Bilde-Sørensen and M. Mogensen, Silica segregation in the Ni/YSZ electrode, J. Electrochem. Soc. 154 (2007) A619-A626 .

[46] Jensen, K. V., R. Wallenberg, Ib Chorkendorff and M. Mogensen, Effect of impurities on structural and electrochemical properties of the Ni–YSZ interface, Solid State Ionics160 (2003) 27– 37.

[47] Lohsoontorn, P., D. J. L. Brett and N. P. Brandon, The Effect of fuel composition and temperature on the interaction of H_2S with Nickel–Ceria anodes for solid oxide fuel cells, J. Power Sources 183 (2008) 232–239.

[48] Hansen, J. B., Correlating sulfur poisoning of SOFC nickel anodes by a Temkin Isotherm. Electrochem. Solid-State Lett.11 (2008) B178 -B180.

[49] Kishimoto, H., T. Horita, K. Yamaji, M. E. Brito, Y. P. Xiong and H. Yokokawa, Sulfur poisoning on SOFC Ni anodes: thermodynamic analyses within local equilibrium anode reaction model, J.Electrochem. Soc.157 (2010) B802-B813.

[50] Sumi, H., P. Puengjinda, H. Muroyama, T. Matsui and K. Eguchi, Effects of crystal structure of yttria- and scandia-stabilized zirconia in nickel-based SOFC anodes on carbon deposition and oxidation behavior, J. Power Sources, 196 (2011) 6048–6054.

[51] Takeguchi, T., Y. Kani, T. Yano, R. Kikuchi, K. Eguchi, K. Tsujimoto, Y. Uchida, A. Ueno, K. Omoshiki and M. Aizaw, Study on steam reforming of CH_4 and C_2 hydrocarbons and carbon deposition on Ni-YSZ Cermets, J. Power Sources 112 (2002) 588–595.

[52] Alzate-Restrepo, V. and J. M. Hill, Carbon deposition on Ni/YSZ anodes exposed to CO/H_2 feeds, J. Power Sources 195 (2010) 1344–1351.

[53] Kim, Y., J. H. Kim, J. Bae, C. W. Yoon and S. W. Nam, In situ analyses of carbon dissolution into Ni-YSZ anode materials, J. Phys. Chem. C 116 (2012) 13281−13288.

[54] Jensen, K. V., S. Primdahl, I. Chorkendorff and M. Mogensen, Microstructural and chemical changes at the Ni-YSZ interface, Solid State Ionics 144 (2001) 197–209.

[55] Utz, A., K.V. Hansen, K. Norrman, E. Ivers-Tiffée and M. Mogensen, Impurity features in Ni-YSZ-H_2-H_2O electrodes, Solid State Ionics183 (2011) 60–70.

[56] Gong, M., X. Liu, J. Trembly and C. Johnson, Sulfur-tolerant anode materials for solid oxide fuel cell application, J. Power Sources 168 (2007) 289–298.

[57] Aguilar, L., S. Zha, S. Li, J. Winnick and M. Liu, Sulfur-tolerant materials for the hydrogen sulfide SOFC, Electrochem. Solid-State Lett. 7 (2004) A324-A326.

[58] Caillot, T., G. Gauthier, P. Delichère, C. Cayron, F.J. Cadete and S. Aires, Evidence of anti-coking behavior of $La_{0.8}Sr_{0.2}Cr_{0.98}Ru_{0.02}O_3$ as potential anode material for solid oxide fuel cells directly fed under methane, J. Catal. 290 (2012) 158–164.

[59] Atkinson, A., S. Barnett, R. J. Gorte, J. T. S. Irvine, A. J. Mcevoy, M. Mogensen, S. C. Singhal and J.Vohs, Advanced anodes for high-temperature fuel cells, Nature Mater. 3(2004) 17-27.

[60] Gong, M., X. Liu, J. Trembly and C. Johnson, Sulfur-tolerant anode materials for solid oxide fuel cell application, J. Power Sources 168 (2007) 289–298.
[61] Howell, T. G., C. P. Kuhnella, T. L. Reitz, A .M. Sukeshini and R. N. Singh, A_2MgMoO_6 (A = Sr,Ba) for use as sulfur tolerant anodes, J. Power Sources 231 (2013) 279-284.
[62] Tao, S. and J. T. S. Irvine, Phase transition in perovskite oxide $La_{0.75}Sr_{0.25}Cr_{0.5}Mn_{0.5}O_{3-\delta}$ observed by in situ high-temperature neutron powder diffraction, Chem. Mater. 18 (2006) 5453-5460.
[63] Zha, S., P. Tsang, Z. Cheng and M. Liu, Electrical properties and sulfur tolerance of $La_{0.75}Sr_{0.25}Cr_{1-x}Mn_xO_3$ under anodic conditions, J. Solid State Chem.178 (2005) 1844–1850.
[64] San Ping Jiang, Development of lanthanum strontium manganite perovskite cathode materials of solid oxide fuel cells: a review, J Mater Sci 43(2008) 6799–6833
[65] Fleig, J., Solid Oxide Fuel Cell Cathodes: Polarization mechanisms and modeling of the electrochemical performance, Annu. Rev. Mater. Res. 33(2003) 61–82.
[66] Horita. T., K. Yamajia, N. Sakaia, H.Yokokawa, T. Kawada and T. Kato, Oxygen reduction sites and diffusion paths at $La_{0.9}\ Sr_{0.1}\ MnO_{3-\delta}$ /yttria-stabilized zirconia interface for different cathodic overvoltages by secondary-ion mass spectrometry, Solid State Ionics 127(2000) 55–65.
[67] Van Roosmalen JAM, Cordfunke EHP, The defect chemistry of $LaMnO_{3\pm\delta}$, 4. defect model for $LaMnO_{3+\delta}$, J Solid State Chem 110 (1994) 109-112.
[68] Kuo JH, Anderson HU, Sparlin DM, Oxidation-reduction behavior of undoped and Sr-doped $LaMnO_3$: defect structure, electrical conductivity, and thermoelectric power, J Solid State Chem 87(1990) 55-63.
[69] S.P. Jiang, A comparison of O_2 reduction reactions on porous $(La,Sr)MnO_3$ and $(La,Sr)(Co,Fe)O_3$ electrodes, Solid State Ionics 146 (2002) 1-22.
[70] Kim, J. D., G. D. Kim, J. W. Moon, H. W. Lee, K.T. Lee and C. E. Kim, The effect of percolation on electrochemical performance, Solid State Ionics 133 (2000) 67–77.
[71] Wilson, J. R., J. S. Cronin, A. T. Duong, S. Rukes, H.Y. Chen, K.Thornton, D. R. Mumm and S. Barnett, Effect of composition of $(La_{0.8}Sr_{0.2}MnO_3–Y_2O_3$-stabilized $ZrO_2)$, Journal of Power Sources 195(2010) 1829-1840
[72] E. V. Bongio, H. Black, F. C. Raszewski, D. Edwards, C. J. McConville and V. R. W. Amarakoon, Microstructural and high-temperature electrical characterization of $La_{1-x}Sr_xFeO_{3-\delta}$, J. Electrocerm. 14 (2005) 193-198.
[73] Sun, C., R. Hui, J. Roller. Cathode materials for solid oxide fuel cells: a review, J. Solid State Electrochem 14 (2010) 1125–1144.
[74] A. Petric, P. Huang, and F. Tietz, Evaluation of La-Sr-Co-Fe-O perovskite for solid oxide fuel cells and gas separation membrances, solid state Ionics, 135 (2000) 719-725.
[75] Rembelski, D., J. P. Viricelle, L. CombemaleandM. Rieu, Characterization and comparison of different cathode materials for SCSOFC: LSM, BSCF, SSC, and LSCF, Fuel Cells 12 (2012) 256–264.
[76] Chroneos, A., B. Yildiz, A. Tarancon, D. Parfitta and J. A. Kilner, Oxygen diffusion in solid oxide fuel cell cathode and electrolyte materials: mechanistic insights from atomistic simulations, Energy Environ. Sci. 4 (2011) 2774–2789.
[77] Simner, S. P., M. D. Anderson, M. H. Engelhard and J. W. Stevenson, Degradation mechanisms of La–Sr–Co–Fe–O_3 SOFC cathodes, Electrochem. Solid-State Lett. 9 (2006) A478-A481.

[78] Li, Z. P., T. Mori, G. J. Auchterlonie, J. Zou and J. Drennan, Two types of diffusions at the cathode/electrolyte interface in IT-SOFCs. J. Solid State Chemistry 184 (2011) 2458–2461.
[79] Oh, D. and D. Gostovic, Mechanism of $La_{0.6}Sr_{0.4}Co_{0.2}Fe_{0.8}O_3$ cathode degradation, J. Mater. Res. 27 (2012) 1992-1999.
[80] Manoj K Mahapatra, Prabhakar Singh, Fuel Cells: Energy Conversion Technology
[81] Bucher, E., W. Sitte, F. Klauser and E. Bertel, Impact of humid atmospheres on oxygen exchange properties, surface-near elemental composition, and surface morphology of $La_{0.6}Sr_{0.4}CoO_{3-\delta}$, Solid State Ionics 208 (2012) 43–51.
[82] Nielsen, J. and M. Mogensen, SOFC LSM:YSZ cathode degradation induced by moisture: an impedance spectroscopy study, Solid State Ionics 189 (2011) 74–81.
[83] X. D. Zhou, J. W. Templeton, Z. Zhu, Y.-S. Chou, G. D. Maupin, Z. Lu, R. K. Brow and J. W. Stevenson, Electrochemical performance and stability of the cathode for solid oxide fuel cells III. role of volatile boron species on LSM/YSZ and LSCF, J. Electrochem. Soc. 157 (2010) B1019-B1023.
[84] Xiong, Y., K. Yamaji, T. Horita, H. Yokokawa, J. Akikusa, H. Eto and T. Inagakic, Sulfur poisoning of SOFC cathodes, J. Electrochem. Soc. 156 (2009) B588-B592.
[85] Bucher, E., C. Gspan, F. Hofer and W. Sitte, Post-test analysis of silicon poisoning and phase decomposition in the SOFC cathode material $La_{0.58}Sr_{0.4}Co_{0.2}Fe_{0.8}O_{3-\delta}$ by transmission electron microscopy, Solid State Ionics 230 (2013) 7–11.
[86] Fergus, J. W., Effect of cathode and electrolyte transport properties on chromium poisoning in solid oxide fuel cells, Int. J. Hyd. Energy 32 (2007) 3664 – 3671.
[87] Wang, F., K.Yamaji, D. H. Cho, T. Shimonosono, H. Kishimoto, M. E. Brito, T. Horita and H. Yokokawa, Sulfur poisoning on $La_{0.6}Sr_{0.4}Co_{0.2}Fe_{0.8}O_3$ cathode for SOFCs, J. Electrochem. Soc. 158 (2011) B1391-B1397.
[88] Schuler, J. A., H. Yokokawa, C. F. Calderone, Q. Jeangros, Z. Wuillemina, A. H. Wyser and J. Van Herle, Combined Cr and S poisoning in solid oxide fuel cell cathodes, J. Power Sources 201 (2012) 112– 120.
[89] Wang, F., K.Yamaji, D. H. Cho, T. Shimonosono, H. Kishimoto, M. E. Brito, T. Horita and H. Yokokawa, Sulfur poisoning on $La_{0.6}Sr_{0.4}Co_{0.2}Fe_{0.8}O_3$ cathode for SOFCs. J. Electrochem. Soc. 158 (2011) B1391-B1397.
[90] Jiang, S. P., L. Christiansen, B. Hughan and K. Foger, Effect of glass sealant materials on microstructure and performance of Sr-doped $LaMnO_3$ cathodes, J. Mater. Sci. Lett. 20 (2001) 695– 697.
[91] Bentzen, J. J., J. V. T. Høgh, R. Barfod and A. Hagen, Chromium poisoning of LSM/YSZ and LSCF/CGO composite cathodes, Fuel Cells 09 (2009) 823–832.
[92] M.A. Laguna-Bercero, Recent advances in high temperature electrolysis using solid oxide fuel cells: a review, Journal of Power Sources 203 (2012) 4–16
[93] Döenitz W, Schmidberger R, Steinheil E, Streicher R. Hydrogen production by high temperature electrolysis of water vapor. Int J Hydrogen Energy 5 (1980) 55–63.
[94] Döenitz W, Schmidberger R, Concepts and design for scaling up high-temperature water vapor electrolysis, Int J Hydrogen Energy 7 (1982) 321-330

[95] W. Dönitz and E. Erdle, High-temperature electrolysis of water vapor- status of development and perspective for application, Int. J. Hydrogen Energy10 (1985) 291–295.
[96] W. Dönitz, G. Dietrich, E. Erdle, and R. Streicher, Electrochecmial high-temperature technology for hydrogen production or direct electricity generation, Int J Hydrogen Energy 13 (1988) 283-287
[97] W. Dönitz, E. Erdle, R. Streicher, 1990. Electrochemical Hydrogen Technologies., Wendt, H.,Editor. Elsevier. p 213.
[98] A. O. Isenberg, Energy conversion via solid oxide electrolyte electrochemical cells at high temperatures, Solid State Ionics 3-4 (1981) 431-437.
[99] V. I. Sharma and B. Yildiz, Degradation mechanism in $La_{0.8}Sr_{0.2}CoO_3$ as contact layer on the solid oxide electrolysis cell anode, J Electrochem Soc 157(2010) B441–448.
[100] A. Hauch, S. D. Ebbesen, S. H. Jensen, M. Mogensen, Solid Oxide Electrolysis Cells: Microstructure and Degradation of the Ni/Yttria-Stabilized Zirconia Electrode, J. Electrochem. Soc. 155 (2008) B1184-B1193.
[101] James E. O'Brien, Carl M. Stoots and J. Stephen Herring, Hoseph J. Hartvigsen, Performace of planar high-temperature electrolysis stacks for hydrogen production from nuclear energy, Nuclear Technology 158 (2007) 118-131.
[102] D. Hickey, M. Cassidy, J. McElroy, F. Mitlitsky and V. Venkataraman, in SOFC-IX, PV2005-07, ed. S. C. Singhal and J. Mizusaki, The Electrochemical Society Inc., Pennington, NJ, USA, 2005, pp. 285–294.
[103] Guan J, Minh N, Ramamurthi B, Ruud J, Hong J, Riley P and D. Weng. High performance flexible reversible solid oxide fuel cell. Final Technical Report, Performed under DOE Cooperative Agreement DE-FC36-04GO14351, GE Global Research Center, Torrance, CA., 2004-2006
[104] A. Momma, T. Kato, Y. Kaga and S. Nagata, Polarization behavior of high temperature solid oxide electrolysis cells, J. Ceram. Soc. Jpn. 105(1997) 369–373.
[105] Kaiser A, Monreal E, Koch A, Stolten D. Reactions at the interface $La_{0.5}Ca_{0.5}MnO_3$ YSZ/Al_2O_3 under anodic current, Ionics 2(1996)184–189.
[106] Lim H, Virkar AV, A study of solid oxide fuel cell stack failure by inducing abnormal behavior in a single cell test, J Power Sources 185 (2008) 790–800.
[107] M. S. Sohal, J. E. O'Brien, C. M. Stoots, V. I. Sharma, B. Yildiz, A. Virkar, Degradation issues in soild oxide cells during high temperature electrolysis, Journal of fuel cell Science and technology, 9 (2012) 011017 1-10.
[108] J.R. Mawdsley, J.D. Carter, A.J. Kropf, B. Yildiz, V.A. Maroni, Post-test evaluation of oxygen electrodes from solid oxide electrolysis stacks, Int. J. Hydrogen Energy 34 (2009) 4198–4207.
[109] Xinfang Jin, Xingjian Xue, Computational fluid dynamics analysis of solid oxide electrolysis cells with delaminations, Int J Hydrogen Energ 35(2010) 7321-7328.
[110] Virkar AV, Mechanism of oxygen electrode delamination in solid oxide electrolyzer cells, Int J Hydrogen Energy 35 (2010) 9527–9543.
[111] Chen K, Jiang SP, Failure mechanism of $(La,Sr)MnO_3$ oxygen electrodes of solid oxide electrolysis cells, Int J Hydrogen Energy 36(2011)10541–10549.
[112] Sergey N. Rashkeev, Michael V. Glazoff, Atomic-scale mechanisms of oxygen electrode delamination in solid oxide electrolyzer cells, International Journal of hydrogen energy (2011)1-12.

[113] Kongfa Chen, Na Ai, San Ping Jiang, Performance and stability of (La,Sr)MnO_3-Y_2O_3-ZrO_2 composite oxygen electrodes under solid oxide electrolysis cell operation conditions, Int. J. Hydrogen Energy 37(2012) 10517-10525.
[114] Chenghao Yang, Adam Coffin, Fanglin Chen, High temperature solid oxide electrolysis cell employing porous structured $(La_{0.75}Sr_{0.25})_{0.95}MnO_3$ with enhanced oxygen electrode performance, International Journal of Hydrogen Energy 35 (2010) 3221-3226
[115] Knibbe R, Traulsen ML, Hauch A, Ebbesen SD, Mogensen M., Solid oxide electrolysis cells: degradation at high current densities, J Electrochem Soc 157 (2010) B1209–1217.
[116] Chenghao Yang, Adam Coffin, Fanglin Chen, Characterization of infiltrated $(La_{0.75}Sr_{0.25})_{0.95}MnO_3$ as oxygen electrode for solid oxide electrolysis cells, International Journal of Hydrogen Energy 35 (2010) 5187-5193
[117] Kongfa Chen, Na Ai, San Ping Jiang, Reasons for the high stability of nano-structured (La,Sr)MnO_3 infiltrated Y_2O_3-ZrO_2 composite oxygen electrodes of solid oxide electrolysis cells, Electrochemistry Communications 19 (2012) 119-122.
[118] Jennifer R. Mawdsley, J. David Carter, A. Jeremy Kropf, Bilge Yildiz, Victor A. Maroni, , Int. J. Hydrogen Energy 34 (2009) 4198-4207.
[119] Sergey N. Rashkeev and Michael V. Glazoff, Control of oxygen delamination in solid oxide electrolyzer cells via modifying operational regime, Applied Physics Letters 99 (2011) 173506
[120] Michael Keane, Manoj K. Mahapatra, Atul Verma and Prabhakar Singh, LSM-YSZ interactions and anode delamination in solid oxide electrolysis cells, Int. J. Hydrogen Energy 37 (2012) 16776-16785.
[121] Y.L. Liu, A. Hagen, R. Barfod, M. Chen, H.J. Wang, F.W. Poulsen, P.V. Hendriksen, Microstructural studies on degradation of interface between LSM-YSZ cathode and YSZ electrolyte in SOFCs, Solid State Ionics 180 (2009) 1298-1304.
[122] C. Clausen, C. Bagger, J. B. Bilde-Sørensen and A. Horsewell, Microstructural and microchemical characterization of the interface between $La_{0.85}Sr_{0.15}MnO_3$ and Y_2O_3-stabilized ZrO_2, Solid State Ionics 70 (1994) 59–64.
[123] J.A.M. Van Roosmalen and E. H. P. Cordfunke, Chemical reactivity and interdiffusion of (La, Sr)MnO_3 and (Zr,Y)O_2, solid oxide fuel cell cathode and electrolyte materials, Solid State Ionics 52 (1992) 303–312.
[124] K. Wiik, C. R. Schmidt, S. Faaland, S. Shamsili, M. A. Sinarsrud and T. Grande, Reactions between strontium-substituted lanthanum manganite and yttria-stabilized zirconia: I, powder samples, J. Am. Ceram. Soc. 82 (1999) 721–728.
[125] T. Kawada, N. Sakai, H. Yokokawa, M. Dokiya and I. Anzai, Reaction between solid oxide fuel cell materials, Solid State Ionics, 50 (1992) 189–196.
[126] G. Stochniol, E. Syskakis, A. Naoumidis, Chemical compatibility between strontium-doped lanthanum manganite and yittria-stabilized zirconia, J. Am. Ceram. Soc. 78 (1995) 929-932.
[127] I. Koshiro, H. Miyamoto, M. Sumi, and K. Mori, in Proc. 10th World Hydrogen Energy Conference, 1994, Cocoa Beach, Florida, USA, pp. 695–701.
[128] Anne Hauch, Sune Dalgaard Ebbesen, Søren Højgaard Jensen and Mogens Mogensen, Highly efficient high temperature electrolysis, J. Mater. Chem. 18 (2008) 2331–2340
[129] F. W. Poulsen and N. V. Puil, Phase relations and conductivity of Sr- and La-zirconates, Solid State Ionics 53-56 (1992) 777-783.
[130] J. A. Labrincha, J.R. Frade, F.M.B. Marques, $La_2Zr_2O_7$ formed at the ceramic electrode/YSZ contacts, J. Mater. Sci. 28 (1993) 3809-3815.

[131] H.Y. Lee, S.M. Oh, Origin of cathodic degradation and new phase formation at the $LaSrMnO_3$/YSZ interface, Solid State Ionics 90 (1996) 133-140.
[132] C. Brugnoni, U. Ducati, M. Scagliotti, SOFC cathode/electrolyte interface. Part I: reactivity between $LaSrMnO_3$ and ZrO_2-Y_2O_3, Solid State Ionics 76 (1995) 177-182.
[133] A. Hagen, Y.L. Liu, R. Barfod, P.V. Hendriksen, J. Electrochem. Soc. 155 (2008) B1047-B1052.
[134] A. Chen, J.R. Smith, K.L. Duncan, R.T. DeHoff, K.S. Jones, E.D. Wachsman, Effect of $La_2Zr_2O_7$ on interfacial resistance in solid oxide fuel cells, J. Electrochem. Soc. 157 (2010) B1624-B1628.
[135] C. Levy, Y. Zhong, C. Morel, S. Marlina, Thermodynamic stabilities of LZ and SZ in SOFC and their relationship with LSM synthesis process, J. Electrochem. Soc. 157 (2010) B1597-B1601.
[136] H.S. Song, W.H. Kim, S.H. Hyun, J. Moon, Influences of starting particulate materials on microstructural evolution and electrochemical activity of LSM-YSZ composite cathode for SOFC, J. Electroceram. 17 (2006) 759-764.
[137] C.C.T. Yang, W.C. J. Wei, A. Roosen, Reaction kinetics and mechanisms between $La_{0.65}Sr_{0.3}MnO_3$ and 8 mol% yttria-stabilized zirconia, J. Am. Ceram. Soc. 87 (2004) 1110-1116.
[138] M. Chen, Y.L. Liu, A. Hagen, P.V. Hendriksen, F.W. Poulsen, LSM-YSZ reactions in different atmospheres, Fuel Cells 09 (2009) 833-840.
[139] K. Wiik, C. R. Schmidt, S. Faaland, S. Shamsili, M. Einarsrud, T. Grande, Reactions between Strontium-Substituted Lanthanum Manganite and Yttria-Stabilized Zirconia: I, Powder Samples, J. Am. Ceram. Soc., 82 (1999) 721–728.
[140] A. Chen, G. Bourne, K. Siebein, R. DeHoff, E. Wachsman, and K. Jones, Characterization of lanthanum zirconate formation at the A-site-deficient strontium-doped lanthanum manganite cathode/yittrium-stabilized zirconia electrolyte interface of solid oxide fuel cells, J. Am. Ceram. Soc. 91 (2008) 2670-2675.
[141] M.C. Brant, T. Matencio, L. Dessemond, R.Z. Domingues, Electrical degradation of porous and dense LSM/YSZ interface, Solid State Ionics 177 (2006) 915-921.
[142] A. Grosjean, O. Sanseau, V. radmilovic, A. Thorel, Reactivity and diffusion between $La_{0.8}Sr_{0.2}MnO_3$ and ZrO_2 at interfaces in SOFC cores by TEM analyses on FIB samples, Solid State Ionics 177 (2006) 1977-1980.
[143] K. Kleveland, M. Einarsrud, C.R. Schmidt, S. Shamsili, S. Faaland, K. Wiik, T. Grande, Reactions between strontium-substituted lanthanum manganite and yttria-stabilized zirconia: II, diffusion couples, J. Am. Ceram. Soc. 82 (1999) 729-734.
[144] H. Taimatsu, K. Wada, H. Kaneko, H. Yamamura, Mechanism of reaction between lanthanum manganite and yttria-stabilized zirconia, J. Am. Ceram. Soc. 75 (1992) 401-405.
[145] L.J.H. Kuo, P. Singh, R.J. Ruka, T.R. Vasilow, R.J. Bratton, US Patent, 056861982, 1997.
[146] M.F. Mahoney, Y. Narendar, H. Huang, WO Patent, 082326 A2, 2011.
[147] E. EI Batawi, P. Munoz, D. Nguyen, US Patent, 0043010 A1, 2012.
[148] P. Sarkar, H. Rho, US Patent, 7736772 B2, 2010.
[149] Y.L. Liu, A. Hagen, R. Barfod, M. Chen, H.J. Wang, F. W. Poulsen, and P. V. Hendriksen, Microstructural studies on degradation of interface between LSM-YSZ cathode and YSZ electrolyte in SOFCs, Solid State Ionics180 (2009) 1298-1304.
[150] A. V. Virkar, A model for solid oxide fuel cell (SOFC) stack degradation, J. Power Sources 172 (2007) 713-724.

[151] K.T. Jacob, Y. Waseda, Potentiometric determination of the Gibbs energies of formation of $SrZrO_3$ and $BaZrO_3$, Metall. Mater. Trans. B 26 (1995) 775-781.
[152] M. Mori, T. Abe, H. Itoh, O. Yamamoto, G.Q. Shen, Y. Takeda, N. Imanishi, Reaction mechanism between lanthanum manganite and yttria doped cubic zirconia, Solid State Ionics 123 (1999) 113-119.
[153] L. Rørmark, K. Wiik, S. Stølen, and T. Grande, Oxygen stoichiometry and structural properties of $La_{1-x}A_xMnO_{3\pm\delta}$ (A=Ca or Sr and $0\leq x\leq 1$), J. Mater. Chem., 12 (2002) 1058-67.
[154] T. Kawashima, Phase equilibria in ZrO_2-Y_2O_3-MnO_t ternary system at 1673K, Mater. Trans., 40 (1999) 967-971.
[155] Qi-Hui Wu, Meilin Liu, W. Jaegermann, X-ray photoelectron spectroscopy of $LaSrMnO_3$, Mater. Lett. 59 (2005) 1980-1983.
[156] J.A.M. van Roosmalem and E. H. P. Cordfunke, Chemical reactivity and interdiffusion of (La, Sr)MnO_3 and (Zr,Y)O_2, solid oxide fuel cell cathode and electrolyte materials, J. Solid State Chem., 93 (1991) 212-219.
[157] M. Chen, A. N. Grundy, B. Hallstedt, and L. J. Gaukler, Thermodynamic modelling of the La-Mn-Y-Zr-O system, Calphad, 30 (2006) 489-500.
[158] Stanek CR, Minervini L, Grimes RB, Nonstoichoimetry in $A_2B_2O_7$ Pyrochlores, J Am Ceram Soc 85 (2002) 2792-2798.
[159] S. Faaland, M.A. Einarsrud, K. Wiik, T. Grande, Reactions between $LaCaMnO_3$ and CaO-stabilized ZrO_2 : part I powder mixtures, J. Mater. Sci. 34 (1999) 957-966.
[160] Dokyol Lee, Ju-Hyeong Han, Youngsuk Chun, Rak-Hyun Song, Dong Ryul Shin, Preparation and characterization of strontium and magnesium doped lanthanum gallates as the electrolyte for IT-SOFC, J. Power Sources 166 (2007) 35–40.
[161] F. Tietz, Thermal expansion of SOFC materials, Ionics 5 (1999) 129-139.
[162] Gwenaël Corbel, Samih Mestiri, Philippe Lacorre, Physicochemical compatibility of CGO fluorite, LSM and LSCF perovskite electrode materials with $La_2Mo_2O_9$ fast oxide-ion conductor, Solid State Sci. 7 (2005) 1216–1224.
[163] Hongming Zhou, Danqing Yi, Zhiming Yu, Lairong Xiao, Preparation and thermophysical properties of CeO_2 doped $La_2Zr_2O_7$ ceramic for thermal barrier coatings, J. Alloys Compd. 438 (2007) 217–221.
[164] Zhenhua Xu, Limin He, Xinghua Zhong, Jiangfeng Zhang, Xiaolong Chen, Hongmei Ma, Xueqiang Cao, Effects of Y_2O_3 addition on the phase evolution and thermophysical properties of lanthanum zirconate, J. Alloys Compd. 480 (2009) 220–224.
[165] A.N. Grundy, B. Hallstedt, L.J. Gauckler, Assessment of the La–Sr–Mn–O system, Calphad 28 (2004) 191-201.
[166] Charlotte C. Appel, Gianluigi A. Botton, Andy Horsewell and W. Michael Stobbs, Chemical and structural changes in manganese-doped yttria-stabilized zirconia studied by electron energy loss spectroscopy combined with electron diffraction, J. Am. Ceram. Soc. 82 (1999) 429–435.
[167] M. Chen, B. Hallstedt, L. J. Gauckler, Thermodynamic modeling of phase equilibria in the Mn–Y–Zr–O system, Solid State Ionics 176 (2005) 1457-1464.
[168] H. Yokokawa, T. Horita, N. Sakai, T. Kawada, M. Dokiya, in: Ulf Bossel (Ed.), First European Solid Oxide Fuel Cell Forum Proceedings, vol. 1, European Solid Oxide Fuel Cell Forum Publishers, Oberrohrdorf, Switzerland, 1994, pp. 425-434.
[169] J. W. Stevenson, P. F. Hallman, T. R. Armstrong, L. A. Chick, Sintering behavior of doped lanthanum and yttrium manganite, J. Am. Ceram. Soc. 78 (1995) 507–512.

[170] Benjamin P. McCarthy, Larry R. Pederson, Ralph E. Williford, Xiaodong Zhou, Low-temperature densification of lanthanum strontium manganite ($La_{1-x}Sr_xMnO_{3+\delta}$), x=0.0–0.20, J. Am. Ceram. Soc. 92 (2009) 1672-1678.
[171] R. A. De Souza, J. A. Kilner, J. F. Walker, A SIMS study of oxygen tracer diffusion and surface exchange in $La_{0.8}Sr_{0.2}MnO_{3+\delta}$, Mater. Lett. 43 (2000) 43–52.
[172] K. Thomas Jacob, Niladri Dasgupta, Yoshio Waseda, Composition-graded solid electrolyte for determination of the Gibbs energy of formation of lanthanum zirconate, J. Am. Ceram. Soc. 81 (1998) 1926-1930.
[173] M.K. Mahapatra, S. Bhowmick, N. Li, P. Singh, Role of oxygen pressure on the stability of lanthanum strontium manganite – yttria stabilized zirconia composite, J. Eur. Ceram. Soc. 32 (2012) 2341-2349.
[174] C.C. Appel, N. Bonanos, A. Horsewell, S. Linderoth, Aging behavior of zirconia stabilized by yttria and manganese oxide, J. Mater. Sci. 36 (2001) 4493–4501.
[175] Y. Zhou, T.C. Lei, T. Sakuma, Diffusionless cubic-to-tetragonal phase transition and microstructural evolution in sintered zirconia–yttria ceramics, J. Am. Ceram. Soc. 74 (1991) 633–640.
[176] K.J. McClellan, S.Q. Xiao, K.P.D. Lagerlof, A.H. Heuer, Determination of the structure of the cubic phase in high-ZrO_2 Y_2O_3-ZrO_2 alloys by convergent-beam electron-diffraction, Philosophical Magazine A Physics Of Condensed Matter Structure Defects And Mechanical Properties,70 (1994) 185–200.
[177] M.K. Mahapatra, P. Singh, S.T. Misture, Manganese induced modifications in yttria stabilized zirconia, Appl. Phys. Lett. 101 (2012) 131606.
[178] S. K. Tiwari, Jhuma Adhikary, T. B. Singh, Raghuvir Singh, Preparation and characterization of sol-gel derived yttria doped zirconia coatings on AISI 316L, Thin Solid Films 517 (2009) 4502-4508.
[179] E. Courtin, P. Boy, T. Piquero, J. Vulliet, N. Poirot, C. Laberty-Robert, A composite sol-gel process to prepare a YSZ electrolyte for solid oxide fuel cells, Journal of Power Sources 206 (2012) 77-83.
[180] M. Gaudon, Ch. Laberty-Robert, F. Ansart, P. Stevens, Thick YSZ films prepared via a modified sol-gel route: thickness control (8-80μm), Journal of the European Ceramic Society 26 (2006) 3153-3160.
[181] Adler SB, Mechanism and kinetics of oxygen reduction on porous $La_{1-x}Sr_xCoO_{3-\delta}$ electrodes, Solid State Ionics 111(1998) 125–34.
[182] Holme TP, Pornprasertsuk R, Prinz FB, Interpretation of low temperature solid oxide fuel cell electrochemical impedance spectra, J Electrochem Soc 157(2010) B64–70.
[183] Jiang SP, Love JG, Zhang JP, Huong M, Ramprakash Y, Hughes AE, et al, The electrochemical performance of LSM/ zirconia–yttria interface as a function of a-site non stoichiometry and cathodic current treatment, Solid State Ionics 121(1999) 1–10.
[184] Backhaus-Ricoult M, Adib K, St.Clair T, Luerssen B, Gregoratti L, Barinov A, In-situ study of operating SOFC LSM/YSZ cathodes under polarization by photoelectron microscopy, Solid State Ionics 179 (2008) 891–895.
[185] Liang M, Yu B, Wen M, Chen J, Xu J, Zhai Y. Preparation of LSM-YSZ composite powder for anode of solid oxide electrolysis cell and its activation mechanism, J Power Sources 190 (2009) 341–345.
[186] De Ridder M, van Welzenis RG, Denier van der Gon AW, Brongersma HH, Wulff S, Chu W

F, et al, Subsurface segregation of yttria in yttria-stabilized zirconia, J Appl Phys 92(2002) 3056–3064.

[187] Virkar AV, Nachlas J, Joshi AV, Diamond J. Internal precipitation of molecular oxygen and electromechanical failure of zirconia solid electrolytes, J Am Ceram Soc 73 (1990) 3382–3390.